UNIVERSITY OF CASSINO

AND SOUTHERN LAZIO

PH.D. IN METHODS, MODELS AND TECHNOLOGIES FOR ENGINEERING

XXXII CYCLE

PH.D. THESIS

Differential Formulation coupled to the Dirichlet-to-Neumann operator for scattering problems

Supervisor

Prof. Antonello Tamburrino

Ph.D. Student

Antea Perrotta

Co-supervisor

Prof. Antonio Maffucci

Prof. Salvatore Ventre

Prof. Lalita Udpa

Coordinator

Prof. Wilma Polini

A.A. 2018/2019

Magnus gubernator et scisso navigat velo et,
si exarmavit, tamen reliquias navigii aptat ad cursum.
Lucio Anneo Seneca

ACKNOWLEDGEMENT

I would like to express my deep and sincere gratitude to my research supervisor, Prof. Antonello Tamburrino of the *DIEI* Department of University of Cassino and the *ECE* Department at Michigan State University, for providing his invaluable guidance throughout the research work described in this Thesis. I am extending my heartfelt thanks to my co-advisors Prof. Antonio Maffucci and Salvatore Ventre of the *DIEI* Department of University of Cassino, and to Prof.ssa Lalita Udpa of the *ECE* Department at Michigan State University.

I am extremely grateful to my parents for their love, prayers, caring and sacrifices for educating and preparing me for my future. Also would like to extend my gratitude to my grandparents for their support and valuable prayers.

Finally, my thanks go to all the people who played a role in my academic accomplishments. Thank you all for your unwavering support.

INTRODUCTION

Interaction of electromagnetic fields with matter arises in many low- and high-frequency applications. Examples are Inverse Scattering Problems, Optimization, Electromagnetic Compatibility (EMC), Antenna Design, etc. In this Thesis a special focus is given to the development of an efficient (i.e. accurate and fast) numerical method for EM scattering. Then, this "tool" can be used as an essential building block for the aforementioned applications.

As it is well known, the electromagnetic scattering from conducting and/or dielectric objects hit by an e.m. wave can be studied using either integral [1]-[2] or differential formulations [3]-[4]. The former are based on Maxwell equations expressed in terms of integral equations. Often the unknown is a proper equivalent source. The latter are based on the "classical" Maxwell equations expressed in term of a system of Partial Differential Equations (PDE). This Thesis is in the framework of differential formulations.

Differential formulations are very attractive because they lead to numerical models characterized by sparse matrices, easier to be stored and inverted. On the contrary, integral formulations involve the treatment of fully-populated matrices. However, integral formulations require to discretize only the material regions, whereas differential formulations require to discretize the computational domain entirely. This is an issue when dealing with a problem in an unbounded domain such as a plane, half-plane, etc. In this case, it is mandatory to "truncate" the computational domain at a proper distance from the scatterer. This calls for a proper treatment of the artificial boundary where the truncation of the computational domain has been carried out.

The truncation of the computational domain in differential formulations (for instance, based on FE or FDTD methods) requires a proper treatment, otherwise significant numerical errors may affect the numerical solution. Spurious reflections of waves from the artificial boundary have to be avoided. To this purpose, in the last decades several approaches have been proposed. They can be classified in two main strategies: non-reflective boundary conditions and non-reflective boundary layers. In the first approach, known as the "classical" Absorbing Boundary Conditions (ABC), e.g. [5], the impinging waves are absorbed on the artificial boundary thanks to proper boundary conditions. In the second approach, the waves are absorbed by an artificial layer, as for the Perfectly Matched Layer

(PML), e.g., [6]. A comprehensive review of methods derived from ABC may be found in [7]-[8], where low- and high-order non-reflecting boundary conditions are presented. In [9], [10], [11], [12], [13], [14] it is possible to find a review of methods based on PML. The absorbing conditions are extremely efficient only if the artificial boundary is placed in the far-field region. To overcome this problem was introduced the adaptive absorbing boundary conditions [15] that can be placed close to the scatterer but depend on the shape and the material of the scatterer. Performances of ABC depends significantly on the incidence angle of the field on the boundary. Waves are absorbed when orthogonal to the artificial boundary. This is not the case for PML which is efficient also for non-orthogonal incidence. We mention that the original PML approach proposed by Berger was transformed in an anisotropic PML by [16] thus reducing the distance between the scatterer and the artificial layer. However, the PML involves in the solution domain the addition of the external absorbing layer, which increases the computational burden.

An alternative approach is based on the so-called Dirichlet-to-Neumann (DtN) operator. This is a proper operator which relates the Dirichlet data on the boundary to the Neumann data, on the boundary. In this way it is possible to decouple the "inner" problem (defined inside the computational domain) from the "outer" problem (defined outside the computational domain). The DtN operator provides an exact boundary condition which can be imposed onto the artificial boundary. This allows to place the artificial boundary close to the scatterer, therefore reducing the size of the computational domain and, ultimately, the computational cost. A DtN based formulation has been originally proposed for different wave propagation problems in , such as acoustic and electromagnetics [17]-[18]. Then, it has been used for several electromagnetic scattering problems, such as for periodic arrays [19], waveguides [20], photonic crystals [21], and more recently in passive composite materials [22]. Recently, it has been adopted for scattering problems applied to conducting cylinders [23]. An extension to multiple scattering problems is also provided in [24]. The DtN operator can be computed in analytical form only for domains with canonical geometries. For instance, the exact DtN operator for spherical boundaries has been derived in [25]. Although the DtN operator can be computed numerically for boundaries of arbitrary shape, an analytical form of the DtN operator offers some advantages. Among them we mention the possibility of controlling the accuracy by properly

truncating a series expansion. Moreover, it entails the possibility of factorizing the DtN operator, as firstly proposed in this thesis. This latter option is essential in view of a relevant improving of the computational cost and efficiency and in view of the application of the DtN operator for internal problems, as required by scatterers with cavities. Also, we highlight that the DtN operator is a non-local operator that, when expressed in analytical form, does not require the evaluation of singular kernels.

In this Thesis, the DtN approach is used to analyze a 2D scattering problem where a dielectric object is hit by an external time-harmonic electromagnetic field. The efficiency of the DtN based approach is compared to state-of-the-art PML. The comparison proves the superior performances of the DtN based approach. In this Thesis we integrate the DtN operator within a finite element method applied to the 2D wave equation. Despite the simplicity of the geometry, this numerical model is capable of handling TMz and TEz illuminations, in the presence of z-invariant dielectric and/or magnetic materials. These materials can also be anisotropic. Also, we highlight that the proposed numerical model is capable of treating either homogeneous or non-homogeneous objects. The first original contribution of this Thesis, with respect to the current state-of-the-art, consists in proposing an analytical sparsification of the DtN operator. This sparsification is of paramount importance because the DtN operator is represented in discrete form by a fully populated matrix with a low/moderate rank. The sparsification allows to reduce significantly the computational cost arising from imposing the boundary condition through the DtN operator. In this Thesis two different sparsifications are proposed: one is based on the analytical form of the series representing the DtN operator, the other of the Fast Fourier Transform (FFT). Another original contribution of this work is the introduction of the Internal DtN operator. This is a straightforward generalization of the DtN approach to problems with cavities, as in the case of tubes. The goal is avoiding the discretization of cavities in a material. This can be carried out by impose the boundary condition on the boundary of the cavity internal by means of the Internal DtN operator. In this case we found that the aforementioned sparsification is mandatory to reduce the computational cost with respect to a traditional FEM where the cavity is part of the discretization. The last original contribution of this Thesis is the extension of the approach to anisotropic, but z-invariant, materials under the TMz or TEz illumination. It is worth noting that these

electromagnetic scattering problems can be treated by means of the DtN operator for the scalar case.

The Thesis is organized as follows. In Chapter 1 a state-of-the-art on major differential formulations used to solve the scattering problem when the domain is closed by an artificial boundary is described. In Chapter 2 we derive the DtN operator for the scalar Helmholtz equation in 2D. Specifically, we briefly summarize the derivation of the DtN operator for the exterior problem, as introduced in past work by other authors and, then, we propose the DtN operator for the interior problem (cavities). In both cases the shape of the boundary is circular so that the DtN operator can be expressed in analytical form. In Chapter 3, we treat the electromagnetic scattering from z-invariant material, possibly anisotropic, in both the TMz and TEz cases. In Chapter 4 the numerical implementation of the method proposed is described. Moreover, in this Chapter is addressed the problem of the sparsification of the DtN operators by means of an analytical factorization and the Fast Fourier Transform. Eventually, in Chapter 5 three case studies are described and discussed. The first is a benchmark case to evaluate and compare the performances of the proposed approach. Specifically, the scattering from a circular cylinder is modelled with both the DtN and PML based approaches, and compared against the analytical solution. When considering an iterative solver, the DtN approach is superior to the PML both in term of number of multiplications per iteration and in term of a better condition number. The second case refers to the electromagnetic scattering from a PVC tube. This case is relevant to prove the effectiveness of the numerical model combined with the Internal DtN operator. In the third case, a bundle cable is considered. This is a real-world case in the framework of electromagnetic compatibility (EMC). Specifically, the goal was to predict the near field.

Contents

List of Figures

Chapter 1

ELECTROMAGNETIC SCATTERING

In this chapter the scattering problem will be introduced, starting with electromagnetism fundamental equations, best known as Maxwell equations. Then a brief state-of-the-art about the techniques to solve the scattering problem with the differential formulation is reported. In the last section the ABC and PML techniques will be briefly described.

1.1 Maxwell's equation

The mathematical model for the electromagnetic fields can be obtained from a set of three-dimensional partial differential equations called Maxwell's equations.

Let $\boldsymbol{E}(r,t)$ be the electric field, $\boldsymbol{J}(r,t)$ the current density,$\boldsymbol{D}(r,t)$ the electric displacement field, $\boldsymbol{\rho}(r,t)$ the free electric charge density, $\boldsymbol{B}(r,t)$ the magnetic flux density and $\boldsymbol{H}(r,t)$ the magnetic field at a point $r \in \mathbb{R}^3$. The Maxwell equations in differential form are:

Gauss's law—The divergence of displacement flux density is equal to the charge density, that is,

$$\nabla \cdot \boldsymbol{D} = \boldsymbol{\rho} + \boldsymbol{\rho}_0 \tag{1.1}$$

where $\boldsymbol{\rho}$ is the charge density from conduction and $\boldsymbol{\rho}_0$ is the source charge density.

Gauss's law for magnetism—The divergence of the magnetic flux density is equal to

zero, that is,

$$\nabla \cdot \boldsymbol{B} = 0 \tag{1.2}$$

Faraday's law of induction—The curl of the electric field intensity is equal to the negative of the time derivative of the magnetic flux density, that is

$$\nabla \times \boldsymbol{E} = -\frac{\partial \boldsymbol{B}}{\partial t} \tag{1.3}$$

Ampere's law—The curl of the magnetic field intensity is equal to the sum of the current density due to flow of charges and the displacement current density, which is the time derivative of the displacement flux density, that is,

$$\nabla \times \boldsymbol{H} = \frac{\partial \boldsymbol{D}}{\partial t} + \boldsymbol{J} + \boldsymbol{J}_0 \tag{1.4}$$

where $\boldsymbol{J}_0$ is the prescribed source and

$$\nabla \cdot \boldsymbol{J}_0 + \frac{\partial \boldsymbol{\rho}_0}{\partial t} = 0 \tag{1.5}$$

In addition, Ohm's law implies that:

$$\boldsymbol{J} = \sigma \boldsymbol{E} \tag{1.6}$$

where $\sigma(r, t)$ is the conductivity. Also, we recall that

$$\boldsymbol{D} = \epsilon \boldsymbol{E} \tag{1.7}$$

$$\boldsymbol{B} = \mu \boldsymbol{H} \tag{1.8}$$

Auxiliary to (1.2)–(1.3), the continuity equation is given by

$$\nabla \cdot \boldsymbol{J} + \frac{\partial \boldsymbol{\rho}}{\partial t} = 0 \tag{1.9}$$

This equation, which is the differential form of the law of conservation of charge, states that the sum of the divergence of the current density due to flow of charges and the time derivative of the charge density is equal to zero. Maxwell's equations simplify considerably in the case of harmonic time dependence. Through the inverse Fourier transform, general solutions of Maxwell's equation can be built as linear combinations of single-frequency solutions:

$$\boldsymbol{E}(r, t) = \frac{1}{2\pi} \int_{-\infty}^{+\infty} \boldsymbol{E}(r, \omega) e^{j\omega t} d\omega \tag{1.10}$$

hereafter we assume that all fields have a time dependence $e^{j\omega t}$.

Replacing time derivatives as $\partial_t \longrightarrow \jmath\omega$, we may rewrite the Maxwell's equation in the form:

$$\nabla\cdot\boldsymbol{D} = \boldsymbol{\rho} + \boldsymbol{\rho}_0 \tag{1.11}$$

$$\nabla\cdot\boldsymbol{B} = 0 \tag{1.12}$$

$$\nabla\times\boldsymbol{E} = -\jmath\omega\boldsymbol{B} \tag{1.13}$$

$$\nabla\times\boldsymbol{H} = \jmath\omega\boldsymbol{D} + \boldsymbol{J} + \boldsymbol{J}_0 \tag{1.14}$$

In order to simplify, the same symbols of electromagnetic fields in time domain have been used in frequency domain. The meaning is clear by the context.

1.1.1 Constitutive relations

Equations (1.11)-(1.14) must be coupled to two constitutive laws that relate $\boldsymbol{E}$ and $\boldsymbol{H}$ to $\boldsymbol{D}$ and $\boldsymbol{B}$. These laws depend on the properties of the matter.

1. *Vacuum or free space*. In the free space the fields are related by the equations:

$$\mathbf{D} = \epsilon_0\boldsymbol{E} \qquad \text{and} \qquad \boldsymbol{B} = \mu_0\mathbf{H} \tag{1.15}$$

   where the costant ϵ_0 and μ_0 are the electric permittivity and magnetic permeability, respectively. The values of ϵ_0 and μ_0 are in the SI system.

$$\epsilon_0 = 8.854\,187 \times 10^{-12}\,\mathrm{Fm}^{-1} \qquad \mu_0 = 4\pi \times 10^{-7}\,\mathrm{Hm}^{-1} \tag{1.16}$$

2. *Inhomogeneous, local isotropic material*. If the material properties do not depend on the direction of the field and the material is linear, we have.

$$\boldsymbol{D} = \epsilon\,\boldsymbol{E} \qquad \text{and} \qquad \boldsymbol{B} = \mu\,\boldsymbol{H} \tag{1.17}$$

   where ϵ and μ are positive and scalar functions.

3. *Inhomogeneous, anisotropic material.* In some materials the electric or magnetic properties of the constituent materials depends on the direction of the field. In such cases ϵ and μ are 3×3 tensor field.

   In the case of ohmic conductors, we have

$$\boldsymbol{J} = \sigma\boldsymbol{E} \tag{1.18}$$

   where σ is the conductivity of the materials. Using the linear inhomogeneous constitutive equations in (1.17) and the constitutive relation for the current in (1.18) we obtain the Maxwell equation in following form:

$$\begin{aligned} \nabla\cdot\epsilon\boldsymbol{E} &= \boldsymbol{\rho} && (1.19)\\ \nabla\cdot\mu\boldsymbol{H} &= 0 && (1.20)\\ \nabla\times\boldsymbol{E} &= -\jmath\omega\mu\boldsymbol{H} && (1.21)\\ \nabla\times\boldsymbol{H} &= \jmath\omega\epsilon\boldsymbol{E} + \sigma\boldsymbol{E} && (1.22) \end{aligned}$$

   When $\sigma > 0$ the region is called *conductor*, if $\sigma = 0$ and $\epsilon \neq \epsilon_0$ the material is termed a *dielectric*, and ϵ is referred to as the *dielectric constant*. In a vacuum $\sigma = 0$, $\epsilon = \epsilon_0$ and $\mu = \mu_0$.

   Defining the complex relative permittivity and permeability by

$$\epsilon_r = \frac{1}{\epsilon_0}\left(\epsilon + \jmath\frac{\sigma}{\omega}\right) \quad \text{and} \quad \mu_r = \frac{\mu}{\mu_0} \tag{1.23}$$

   noting that $\epsilon_r = \mu_r = 1$ in vacuum, we can rewrite the Maxwell's equations as follows:

$$\begin{aligned} \nabla\times\boldsymbol{E} &= -\jmath\omega\mu_0\mu_r\boldsymbol{H} && (1.24a)\\ \nabla\times\boldsymbol{H} &= \jmath\omega\epsilon_0\epsilon_r\boldsymbol{E} + \boldsymbol{J} && (1.24b)\\ \nabla\cdot(\mu_r\boldsymbol{H}) &= 0 && (1.24c)\\ \nabla\cdot(\epsilon_r\boldsymbol{E}) &= \boldsymbol{\rho} && (1.24d) \end{aligned}$$

1.1.2 Interfaces condition

Equations (1.24) are not complete at interfaces between different materials, where either μ_r or ϵ_r are discontinuous.

Let us consider the case of two media with different relative permittivity and permeability, separated by a surface *S*, and let $\boldsymbol{\nu}$ a normal unit vector from region 2 to region 1, as shown in Figure 1.1.

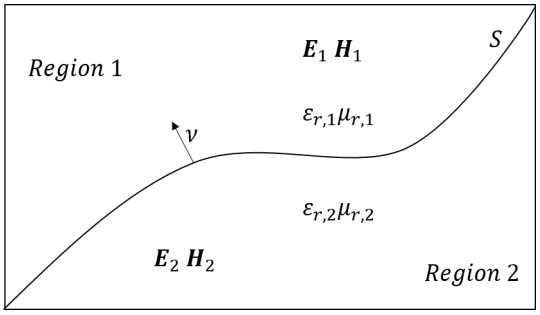

Figure 1.1: Case of two media with different electric e magnetic properties

When an electromagnetic field faces an abrupt change in the permittivity and permeability, certain continuity conditions on electric and magnetic fields on the interface have to be imposed. These continuity conditions are known as the interface conditions for the electromagnetic field. As shown in the Figure 1.1, if $\mathbf{E}_1$ is the electric field from region 1 and $\mathbf{E}_2$ electric field from region 2. From equation (1.24a) we must have that the tangential component of the electric field to be continuous across S, i.e.,

$$\boldsymbol{\nu} \times (\mathbf{E}_1 - \mathbf{E}_2) = 0 \qquad \text{on } S \tag{1.25}$$

Similarly to (1.24b) for the normal magnetic field we have

$$\boldsymbol{\nu} \times (\mathbf{H}_1 - \mathbf{H}_2) = \mathbf{J}_s \qquad \text{on } S \tag{1.26}$$

where $\mathbf{J}_s$ is a surface current density on surface *S*. From equation (1.24c) we must have the normal component of the magnetic flux density to be continuous across S, i.e:

$$\boldsymbol{\nu} \cdot (\mu_{r,1}\mathbf{H}_1 - \mu_{r,2}\mathbf{H}_2) = 0 \qquad \text{on } S. \tag{1.27}$$

Similarly to (1.24d) for the normal flux density we have:

$$\boldsymbol{\nu} \cdot (\epsilon_{r,1}\mathbf{E}_1 - \epsilon_{r,2}\mathbf{E}_2) = \rho_s \qquad \text{on } S \tag{1.28}$$

where ρ_s is the charge density on surface *S*.

1.2 State of art of numerical methods for scattering problems

In this section, a brief state of the art about the solution of differential formulations when truncating the computational domain with boundary conditions is reported. When solving the scattering problem by means of differential formulations (for instance, FE or FDTD methods), it is necessary to introduce artificial boundary to limit the numerical solution to a bounded domain. Non-reflecting conditions must be imposed to avoid spurious reflections of waves from this artificial boundary, proper non-reflecting conditions must be imposed. To this purpose, several approaches have been proposed in the last decades that can be classified into two main types: non-reflective boundary conditions and non-reflective boundary layers. In the first approach, the impinging waves are absorbed by the artificial boundary, as for instance the classical Absorbing Boundary Conditions (ABC), e.g., [18], [26]. In the second approach, the waves are absorbed by a layer, as in the case of the Perfectly Matched Layer (PML), e.g., [6].

1.2.1 Absorbing Boundary Conditions

Whenever one solves a PDE numerically starting from differential formulations by a volume discretization, one must truncate the computational domain in some way, and the key question is how to perform this truncation without introducing significant artifacts into the computation. Some problems are naturally truncated, e.g. for periodic structures where periodic boundary conditions can be applied. Some problems involve solutions that are rapidly decaying in space, so that the truncation is irrelevant as long as the computational domain is large enough. However, some of the most difficult problems to truncate involve wave equations, where the solutions are oscillating and typically decay with distance r as $1/r^{(d-1)/2}$ in d dimensions. The slow decay means that by simply truncating the grid with hard-wall (Dirichlet or Neumann) or by periodic boundary conditions will lead to unacceptable artifacts from boundary reflections. The oscillation means that any real coordinate remapping from an infinite to a finite domain will result in solutions that oscillate infinitely fast as the boundary is approached such fast oscillations cannot be represented by any finite-resolution grid, and will instead effectively form a reflecting hard

wall. Therefore, wave equations require something different: an absorbing boundary that will somehow absorb waves that strike it, without reflecting them, and without requiring infeasible resolution.The first attempts at such absorbing boundaries for wave equations involved absorbing boundary conditions (ABCs) [18], [26].Given a solution on a discrete grid, a boundary condition is a rule to set the value at the edge of the grid. An ABC tries to somehow extrapolate from the interior grid points to the edge grid point(s), to fool the solution into "thinking" that it extends forever with no boundary. It turns out that this can be done perfectly in one dimension, where waves can only propagate in two directions. However, the main interest for numerical simulation lies, in two and three dimensions [27], [28], and in these cases the infinite number of possible propagation directions makes the ABC problem much harder. It seems unlikely that any other efficient method exists that can exactly absorb radiating waves that strike a boundary at any possible angle. Existing ABCs restrict themselves to absorbing waves exactly only at a few angles, especially at normal incidence. Another difficulty is that many standard ABCs are formulated only for homogeneous materials at the boundaries [29], [30], and may even become numerically unstable if the grid boundaries are inhomogeneous.

1.2.2 Perfect Matched Layer

In 1994, however, the problem of the absorbing boundaries in wave equations was analyzed in a different way in a seminal paper by Berenger, where he introduced for the first time the concept of "perfect matched layer" [6]. Berenger changed the absorbing boundary condition, with the introduction of an absorbing boundary layer, as shown in Figure 1.2.

An absorbing boundary layer is a layer of artificial absorbing material that is placed adjacent to the boundary of the computational domain. When a wave enters the absorbing layer, it is attenuated by the absorption and decays exponentially; even if it reflects off the boundary, the returning wave after one round trip through the absorbing layer is exponentially small. The problem with this approach is that, whenever you have a transition from one material to another, waves generally reflect. However, Berenger demonstrated that a special absorbing medium could be constructed so that waves do not reflect at the interface: a perfectly matched layer, or PML. In this case, an external layer of thickness δ

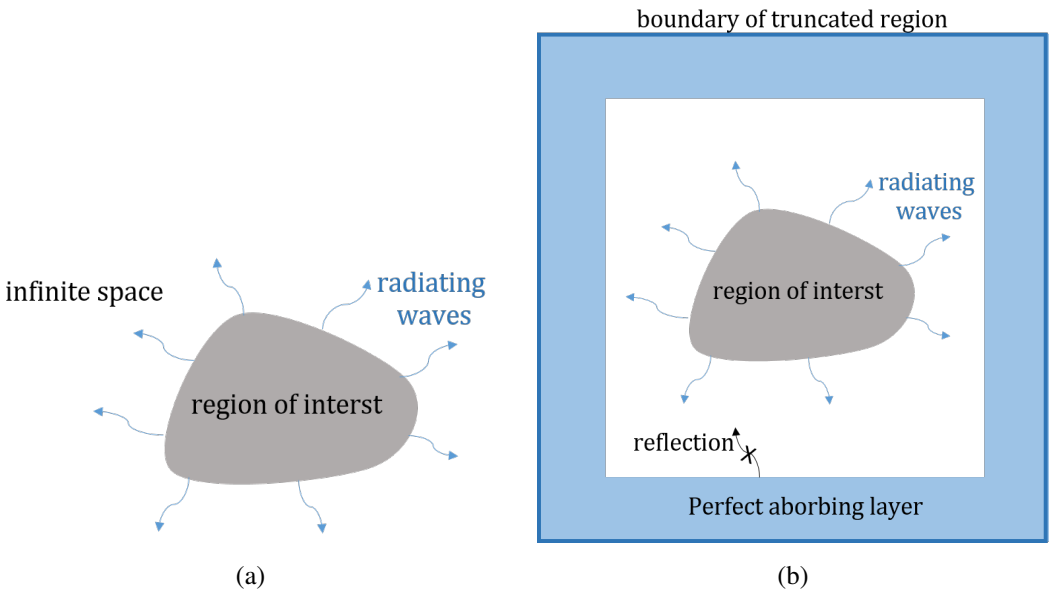

Figure 1.2: (a) Schematic of a typical wave-equation problem, where a finite interest region has sources from which some radiative waves escape to infinity. (b) The same problem, where space has been truncated to some computational region. An absorbing layer is placed adjacent to the edges of the computational region—a perfect absorbing layer would absorb outgoing wave without reflections from the edge of the absorber.

is added to the boundary, where the propagating waves are attenuated as:

$$e^{\jmath(\omega t - kr) - \frac{k}{\omega}\int_0^{\delta}\sigma(r')dr'} \tag{1.29}$$

where $\sigma > 0$ is the conductivity function of the distance.

1.2.3 Dirichlet-to-Neumann transformation

The absorbing conditions are extremely efficient if the artificial boundary is placed in the far-field region, whereas their computational burden increases if placed in the near-field region, where the field is characterized also by the presence of evanescent waves. In general, for a fixed accuracy the computational cost of a near field simulation increases when the boundary is placed closer to the scatterer. An alternative approach is based on the so-called Dirichlet-to-Neumann (DtN) operator, where exact boundary conditions can be imposed on a closest boundary of the solution domain, even when located in proximity of the scatterer, reducing the solution domain to be meshed. This approach has been originally proposed for different wave problems, like acoustic [31]-[32], optical [33] and electromagnetics [34]. Then, it has been used for several electromagnetic scattering problems, such as periodic arrays [19], in waveguides [20], in transmission line [35] and more recently in passive composite materials [22]. An extension of the use of the DtN operator is also provided for analyzing photonic crystals through numerical methods [36], [21], [37] or for photonic bandgap calculations [38], [39], [40].

In addition the DtN operator condition can be derived for the numerical solution of time-harmonic multiple scattering problems, where the scatterer consists of several disjoint components.It is obtained by combining contributions from multiple purely outgoing wave fields. In [24] has been demonstrated that the DtN condition for multiple scattering is as accurate as the well-known DtN condition for single scattering problems.

In recent years the DtN operator has been successfully applied to many different problems. Among them we mention applications to inverse problems for elliptic wave propagation [41], to efficiently extract the capacitance, resistance and inductance of multiconductor transmission lines [42], to characterize the interconnect structures [43] and also for the water-wave problems [44],[45]. Eventually, we mention that the DtN operator has

been introduced also for 3D eddy currents computation in the magneto-quasi-static limit [46].

Chapter 2

DIRICHLET-TO-NEUMANN OPERATOR

This chapter focuses on a differential formulation coupled to the Dirichlet-to-Neumann operator to solve a scattering problem by arbitrarily shaped objects. From a general perspective, the DtN operator provides the "connection" (the mapping) between Dirichlet and Neumann data onto a properly closed surface. In this way, exact boundary conditions may be imposed on the boundary of the solution domain, even when located in proximity of the scatterer. Such operator allows to truncate the computational domain from an infinite one to a finite one. Specifically, it provides an exact boundary condition on the boundary of the computational domain thus allowing this boundary to be placed in close proximity of the scatterer to reduce the computational cost.

This approach has been originally proposed for acoustic problems [32] and for several electromagnetic scattering problems, such as for periodic arrays [19], waveguides [20], photonic crystals [21], and more recently passive composite materials [22].

In the first part of the chapter a 2D scalar scattering problem coupled to the Dirichlet-to-Neumann operator is considered. The mathematical model is given in terms of a weak form. This weak form will be then (see Chapter 4) translated in discrete terms through the Finite Elements Method.

In the second part of the chapter we introduce the DtN operator for the internal problem. Despite its conceptual simplicity, this DtN operator is very useful for treating the

scattering from materials having one or more cavities. This is a first original contribution of this work.

2.1 Forward problem

Let us consider a scatterer Ω characterized by the refraction index m given by:

$$m = \frac{\sqrt{\epsilon\mu}}{\sqrt{\epsilon_0\mu_0}} = \sqrt{\epsilon_r\mu_r} \tag{2.1}$$

with ϵ_r and μ_r the relative electric permittivity and relative magnetic permeability.

The relevant partial differential equation (PDE) in strong form is [47]:

$$\begin{aligned} \bigtriangledown^2 w + k^2 m^2 w &= 0 \qquad \text{in} \quad \Omega \\ \bigtriangledown^2 w + k^2 w &= 0 \qquad \text{in} \quad \mathbb{R}^2 \setminus \Omega \\ w|_{\partial\Omega^-} - w|_{\partial\Omega^+} &= 0 \\ \partial_n w|_{\partial\Omega^-} - \partial_n w|_{\partial\Omega^+} &= 0 \\ \lim_{r\to\infty} r^{1/2}\big(\partial_r(w - w^i) + jk(w - w^i)\big) &= 0 \end{aligned} \tag{2.2}$$

where $w = w^i + w^s$ is the total field as the sum of the incident w^i and the scattering w^s field, k is the wave number, $\partial\Omega^-$ is the inner page and $\partial\Omega^+$ is the outer page of $\partial\Omega$, ∂_n is the normal partial derivative and ∂_r is the radial partial derivative.

2.1.1 Differential formulation coupled to the DtN operator

We assume that the scatterer is contained in a circular bounded domain $\Omega \subset B_R \triangleq \{r \in \mathbb{R}^2 \mid |r| \leq R\}$, as shown in Figure 2.1 with radius R.

The corresponding weak form in B_R is given by [34]:

$$\int_{\partial B_R} \varphi \partial_n w \, dl - \int_{B_R} \nabla\varphi \cdot \nabla w \, dS + k^2 \int_{B_R} m^2 \varphi w \, dS = 0, \quad \forall \varphi \in H^1(B_R) \tag{2.3}$$

where $w \in H^1(B_R)$, with $H^1(B_R) = \{\varphi \in L^2(B_R) | \nabla\varphi \in L^2(B_R)\}$.

The equation (2.3) is the final weak formulation [47]. It is equivalent to the strong form above. Firstly, if we look at the strong form, we have two separate partial derivatives of w, so the strong form requires w to be continuously differentiable until at least the second

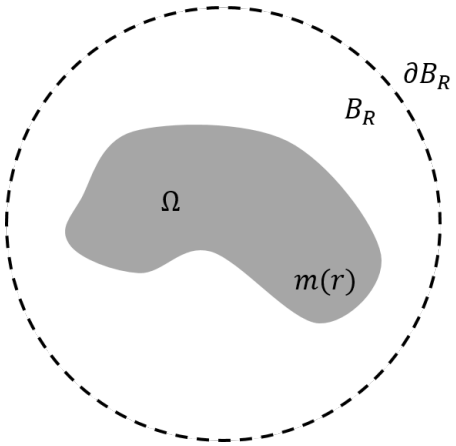

Figure 2.1: The reference problem. An arbitrarily-shaped object Ω and the contained domain

partial derivative. The weak formulation has reduced this requirement to only first partial derivatives. This is the first big advantage of a weak formulation. In general, solving the strong form (governing differential equations) is not always efficient and there may not be smooth (classical) solutions to a problem in particular. This is true especially in the case of complex domains and/or different material interfaces etc. Moreover, incorporating boundary conditions is always a daunting task when solving strong forms directly. It is stronger the need to have continuous field variables. In order to overcome the above difficulties, weak formulations are preferred. They reduce the continuity requirements on the approximation (or basis functions) functions thereby allowing the use of easy-to-construct and implement polynomials. This is one of the main reasons that explain the popularity of weak formulations.

Our reference problem consists of computing the electromagnetic scattering from an object of arbitrary shape, hit by a known incident field. At any spatial position r the total field is given by the sum of the of the incident and the scattering fields:

$$w(r) = w^s(r) + w^i(r).$$

Then it follows that:

$$\int_{\partial B_R} \varphi \partial_n (w^s + w^i) dl - \int_{B_R} \nabla\varphi \cdot \nabla (w^s + w^i) dS$$
$$+k^2 \int_{B_R} m^2 \varphi (w^s + w^i) dS = 0, \quad \forall \varphi \in H^1(B_R) \tag{2.4}$$

The Dirichlet-to-Neumann operator for the exterior problem in $\mathbb{R}^2 \setminus B_R$ is defined as

$$\partial_n w^s|_{\partial B_R} = \Lambda_R[w^s|_{\partial B_R}] \tag{2.5}$$

and

$$\int_{\partial B_R} \varphi(\Lambda_R w^s) dl - \int_{B_R} \nabla\varphi \cdot \nabla w^s dS + k^2 \int_{B_R} m^2 \varphi w^s dS = f, \quad \forall \varphi \in H^1(B_R) \tag{2.6}$$

being

$$f = -\int_{\partial B_R} \varphi \partial_n w^i dl + \int_{B_R} \nabla\varphi \cdot \nabla w^i dS - k^2 \int_{B_R} m^2 \varphi w^i dS \tag{2.7}$$

It is worth nothing that the source term *f* for (2.6) has to be vanishing when $m = 1$, i.e when there is no scatterer:

$$-\int_{\partial B_R} \varphi \partial_n w^i dl + \int_{B_R} \nabla\varphi \cdot \nabla w^i dS - k^2 \int_{B_R} \varphi w^i dS = 0 \tag{2.8}$$

Equation (2.8) can be exploited to rewrite (2.7) as follows:

$$f = -k^2 \int_{B_R} (m^2 - 1) \varphi w^i dS \tag{2.9}$$

2.1.2 Dirichlet-to-Neumann operator for a circle

In this section, we will compute the DtN operator on a circle for the exterior problem in 2-dimensions (2D). The starting point is the following representation of the field as a solution of the Helmholtz equation in cylindrical coordinates (see Appendix A).

$$w(r, \theta) = \sum_{n=-\infty}^{+\infty} w_n H_n^{(2)}(kr) e^{jn\theta} \tag{2.10}$$

where $H_n^{(2)}$ are the second-order Hankel functions.

From (2.10), according with [48], it follows that:

$$\begin{aligned}\partial_r w(r,\theta) &= \sum_{n=-\infty}^{+\infty} w_n \frac{dH_n^{(2)}}{dr}(kr)e^{jn\theta} \\ &= \sum_{n=-\infty}^{+\infty} w_n k \frac{H_{n-1}^{(2)}(kr) - H_{n+1}^{(2)}(kr)}{2} e^{jn\theta}\end{aligned} \tag{2.11}$$

thus the DtN operator onto a circumference of radius R is the operator described by:

$$\Lambda_R : w(r,\theta) \longrightarrow \frac{k}{4\pi} \sum_{n=-\infty}^{+\infty} \left[\frac{H_{n-1}^{(2)}(kR) - H_{n+1}^{(2)}(kR)}{H_n^{(2)}(kR)} \int_0^{2\pi} w(R,\theta') e^{jn\theta'} d\theta' \right] e^{jn\theta} \tag{2.12}$$

or:

$$\Lambda_R[e^{jn\theta}] = \frac{k}{2} \frac{H_{n-1}^{(2)}(kR) - H_{n+1}^{(2)}(kR)}{H_n^{(2)}(kR)} e^{jn\theta} \tag{2.13}$$

Moreover, we notice that:

$$w_n = \frac{1}{2\pi H_n^{(2)}(kR)} \int_0^{2\pi} w(R,\theta) e^{jn\theta} d\theta. \tag{2.14}$$

The operator is therefore known in analytical form, in terms of a series expansion. It is worth noting that the position of the circular boundary may be arbitrarily chosen, even in close proximity of the scatterers. Therefore, the size of the solution domain may be strongly reduced without any impact on accuracy of numerical solution.

2.2 Internal Dirichlet-to-Neumann operator

Let us consider a scatterer having refraction index m, the relevant problem in strong form is described in (2.2). The problem analyzed in this section, is the evaluation (in the frequency domain) of the electromagnetic scattering from a hollow object. The final goal is to evaluate the scattered field, w^s, assuming the incident field w^i is known. At a generic position r the total field is given by the sum of the two aforementioned contributions:

$$w(r) = w^s(r) + w^i(r) \tag{2.15}$$

We assume that the scatterer is contained in an anular domain that is bounded by two boundaries ∂B_R^o and ∂B_R^I (see Figure 2.2).

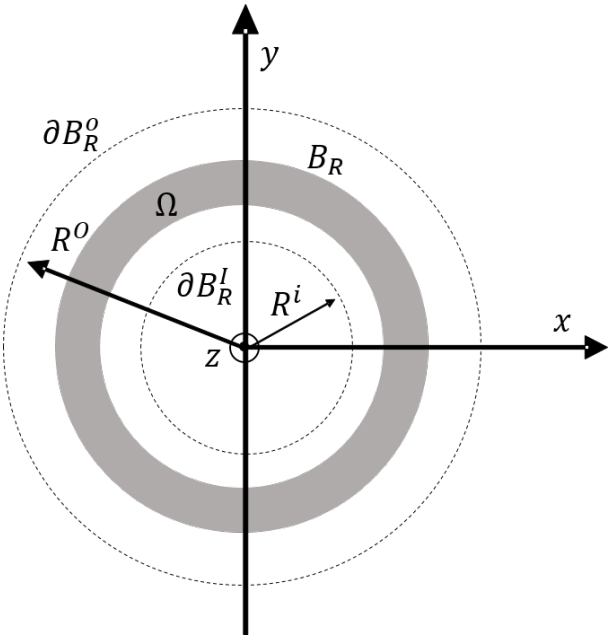

Figure 2.2: Scatterer contained in a bounded domain, with an internal and external boundaries

By considering that the boundary domain ∂B_R is the union of ∂B_R^o and ∂B_R^I, the corresponding weak form in B_R, is given by

$$\begin{aligned} &\int_{\partial B_R^o} \varphi \partial_n w \, dl + \int_{\partial B_R^I} \varphi \partial_n w \, dl - \\ &\int_{B_R} \nabla\varphi \cdot \nabla w \, dS + k^2 \int_{B_R} m^2 \varphi w \, dS = 0, \quad \forall \varphi \in H^1(B_R) \end{aligned} \tag{2.16}$$

then

$$\begin{aligned} &\int_{\partial B_R^o} \varphi \partial_n (w^s + w^i) dl + \int_{\partial B_R^I} \varphi \partial_n (w^s + w^i) dl - \\ &\int_{B_R} \nabla\varphi \cdot \nabla (w^s + w^i) dS + k^2 \int_{B_R} m^2 \varphi (w^s + w^i) dS = 0, \quad \forall \varphi \in H^1(B_R) \end{aligned} \tag{2.17}$$

where $H^1(B_R) = \{\varphi \in L^2(B_R) \mid \nabla\varphi \in L^2(B_R)\}$.

Let Λ_R^o be the Dirichlet-to-Neumann operator for the exterior problem in $R^o \leq r \leq \infty$, i.e.,

$$\partial_n w^s|_{\partial B_R^o} = \Lambda_R^o [w^s|_{\partial B_R^o}] \tag{2.18}$$

and, analogously, let Λ_R^I be the Dirichlet-to-Neumann operator for the internal problem

$0 \leq r \leq R^i$, i.e.,

$$\partial_n w^s|_{\partial B_R^I} = \Lambda_R^I[w^s|_{\partial B_R^I}]\,. \tag{2.19}$$

According to (2.18) and (2.19), the equation (2.17) became:

$$\begin{aligned} &\int_{\partial B_R^o} \varphi \Lambda_R^o(w^s) dl + \int_{\partial B_R^I} \varphi \Lambda_R^I(w^s) dl - \\ &\int_{B_R} \nabla\varphi \cdot \nabla w^s dS + k^2 \int_{B_R} m^2 \varphi w^s dS = f, \quad \forall \varphi \in H^1(B_R) \end{aligned} \tag{2.20}$$

being:

$$\begin{aligned} f &= -\int_{\partial B_R^o} \varphi \partial_n(w^i) dl - \int_{\partial B_R^I} \varphi \partial_n(w^i) dl + \int_{B_R} \nabla\varphi \cdot \nabla w^i dS - k^2 \int_{B_R} m^2 \varphi w^i dS \\ &= -k^2 \int_{B_R} (m^2 - 1) \varphi w^i dS. \end{aligned} \tag{2.21}$$

where f is a source term that depends only on the know incident field, that we will consider in the next paragraphs as a plane wave.

2.2.1 Dirichlet-to-Neumann operator for a circle

The DtN operator on the circle for the exterior problem in 2D has already been calculated in Section 2.2 . Here we compute the DtN operator on the circle for the interior problem in 2D case.

The starting point is the following representation of the field in the internal domain, resulting from the solution of the Helmholtz equation in cylindrical coordinates

$$w(r,\theta) = \sum_{n=-\infty}^{+\infty} w_n J_n(kr) e^{jn\theta} \tag{2.22}$$

where J_n are the Bessel functions.

From (2.22) it follows that

$$\begin{aligned} \partial_r w(r,\theta) &= \sum_{n=-\infty}^{+\infty} w_n \frac{dJ_n}{dr}(kr) e^{jn\theta} \\ &= \sum_{n=-\infty}^{+\infty} w_n k \frac{J_{n-1}(kr) - J_{n+1}(kr)}{2} e^{jn\theta}\,. \end{aligned} \tag{2.23}$$

Thus the DtN into the circumference on radius R^i is the operator described by:

$$\Lambda_R^I : w(r,\theta) \longrightarrow -\frac{k}{4\pi} \sum_{n=-\infty}^{+\infty} \left[\frac{J_{n-1}(kR^i) - J_{n+1}(kR^i)}{J_n(kR^i)} \int_0^{2\pi} w(R^i,\theta') e^{jn\theta'} d\theta' \right] e^{jn\theta} . \tag{2.24}$$

Moreover, we can notice that:

$$w_n = \frac{1}{2\pi J_n(kR^i)} \int_0^{2\pi} w(R^i,\theta) e^{jn\theta} d\theta . \tag{2.25}$$

It should be noted that: (i) only the boundary values of w are needed in order to compute the (2.22) and (2.24), (ii) the DtN is a non local operator.

Chapter 3

TRANSVERSE MAGNETIC AND ELECTRIC ILLUMINATION

This chapter is focused on differential formulations coupled with the Dirichlet-to-Neumann operator for the Transverse Magnetic and Transverse Electric illumination, where the object may be anisotropic but it is z-invariant (TMz or TEz, respectively). This extension to TMz and TEz scattering is another original contribution of this work. It is worth noting that the scatterers under investigation can be either homogeneous or inhomogeneous and either isotropic or anisotropic.

3.1 Problem setting

Let us consider a cylindrical scatterer of arbitrary cross section $\Omega \subset \mathbb{R}^2$ described by the permittivity tensor ε and the permeability tensor μ. These tensors are both invariant with z, i.e. $\varepsilon = \varepsilon(x, y)$ and $\mu = \mu(x, y)$. In addition, we assume that the scatterer is symmetric about the z axis. Consequently, tensors ε and μ are

$$\varepsilon = \begin{bmatrix} \varepsilon_{xx} & \varepsilon_{xy} & 0 \\ \varepsilon_{yx} & \varepsilon_{yy} & 0 \\ 0 & 0 & \varepsilon_{zz} \end{bmatrix} ; \ \mu = \begin{bmatrix} \mu_{xx} & \mu_{xy} & 0 \\ \mu_{yx} & \mu_{yy} & 0 \\ 0 & 0 & \mu_{zz} \end{bmatrix}. \tag{3.1}$$

and ε_T, μ_T refer to the transverse part of ε and μ, respectively:

$$\varepsilon_T = \begin{bmatrix} \varepsilon_{xx} & \varepsilon_{xy} \\ \varepsilon_{yx} & \varepsilon_{yy} \end{bmatrix};\ \mu_T = \begin{bmatrix} \mu_{xx} & \mu_{xy} \\ \mu_{yx} & \mu_{yy} \end{bmatrix}. \tag{3.2}$$

Hereafter, for the sake of convenience, we define $\Omega_e = \Omega \times [0,1]$. Ω_e corresponds to a unit length section of the cylindrical scatterer. Its boundary $\partial\Omega_e$ is

$$\partial\Omega_e = S_0 \cup S_1 \cup S_l \tag{3.3}$$

being $S_0 = \Omega \times \{0\}$, $S_1 = \Omega \times \{1\}$ and $S_l = \partial\Omega \times [0,1]$.

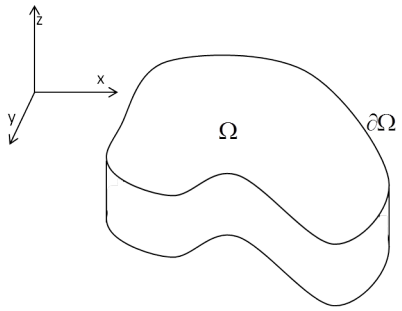

Figure 3.1: The reference problem. An arbitrarily shaped object Ω_e

3.2 TMz illumination

3.2.1 Forward problem

We assume that the source electric current density $\mathbf{J}_0$ is oriented along the z-direction and does not depend on z, i.e. $\mathbf{J}_0 = J_0(x,y)\,\hat{\mathbf{i}}_z$. The electric field $\mathbf{E}$ is z-directed too, $\mathbf{E} = E_z(x,y)\hat{\mathbf{i}}_z$. Since $\mathbf{E}$ is curl-conforming, under the TM illumination, we have that E_z is grad-conforming under the TM illumination

From Maxwell equations we have that the electric field satisfies:

$$\nabla \times \frac{j\nu}{\omega} \nabla \times \mathbf{E} = j\omega\varepsilon\mathbf{E} + \mathbf{J}_0. \tag{3.4}$$

3.2.2 Weak formulation

The corresponding weak form of (3.4) is given by:

$$\int_{\Omega_e} \boldsymbol{\varphi} \cdot \nabla \times \frac{j\nu}{\omega} \nabla \times \mathbf{E} dV = \int_{\Omega_e} j\omega \boldsymbol{\varphi} \cdot \varepsilon \mathbf{E} dV + \int_{\Omega_e} \boldsymbol{\varphi} \cdot \mathbf{J}_0 dV \tag{3.5}$$

then:

$$\int_{\Omega_e} \boldsymbol{\varphi} \cdot \nabla \times \nu \nabla \times \mathbf{E} dV - \int_{\Omega_e} \omega^2 \boldsymbol{\varphi} \cdot \varepsilon \mathbf{E} dV = - \int_{\Omega_e} j\omega \boldsymbol{\varphi} \cdot \mathbf{J}_0 dV. \tag{3.6}$$

We take as test function φ's defined as follows:

$$\boldsymbol{\varphi} = \varphi_z(x, y) \hat{\mathbf{i}}_z. \tag{3.7}$$

It is worth noting that $\boldsymbol{\varphi} \in H(\text{rot}, \Omega_e)$, where

$$H(\text{rot}, \Omega_e) = \left\{ \boldsymbol{\varphi} \in \left(L^2(\Omega_e) \right)^2 \ : \ \text{rot}(\boldsymbol{\varphi}) \in L^2(\Omega_e) \right\} . \tag{3.8}$$

and $\varphi_z \in H^1(\Omega_e)$ where

$$H^1(\Omega_e) = \left\{ \varphi_z \in L^2(\Omega_e) \ : \ \nabla \varphi_z \in \left(L^2(\Omega_e) \right)^2 \right\} . \tag{3.9}$$

Using the vector identity:

$$\nabla \cdot (\boldsymbol{\varphi} \times \nu \nabla \times \mathbf{E}) = (\nabla \times \boldsymbol{\varphi}) \cdot (\nu \nabla \times \mathbf{E}) - \boldsymbol{\varphi} \cdot \nabla \times \nu \nabla \times \mathbf{E} \tag{3.10}$$

in equation (3.6) we have:

$$\begin{aligned} \int_{\Omega_e} (\nabla \times \boldsymbol{\varphi}) \cdot (\nu \nabla \times \mathbf{E}) dV - \int_{\Omega_e} \nabla \cdot (\boldsymbol{\varphi} \times \nu \nabla \times \mathbf{E}) dV - \int_{\Omega_e} \omega^2 \boldsymbol{\varphi} \cdot \varepsilon \mathbf{E} \\ = - \int_{\Omega_e} j\omega \boldsymbol{\varphi} \cdot \mathbf{J}_0 dV \end{aligned} \tag{3.11}$$

Hereafter, we define ν as:

$$\nu = \mu^{-1}. \tag{3.12}$$

Thus

$$\nu = \begin{bmatrix} \nu_{xx} & \nu_{xy} & 0 \\ \nu_{yx} & \nu_{yy} & 0 \\ 0 & 0 & \nu_{zz} \end{bmatrix} \tag{3.13}$$

and ν_T is the transverse part of ν, i.e.

$$\nu_T = \begin{bmatrix} \nu_{xx} & \nu_{xy} \\ \nu_{yx} & \nu_{yy} \end{bmatrix}. \tag{3.14}$$

Let us consider the first integral in (3.11):

$$I_1 = \int_{\Omega_e} (\nabla \times \boldsymbol{\varphi}) \cdot (\nu \nabla \times \mathbf{E}) dV. \tag{3.15}$$

We notice that:

$$\nabla \times \mathbf{E} = \nabla E_z(x, y) \times \hat{\mathbf{i}}_z \tag{3.16}$$

and, similarly

$$\nabla \times \boldsymbol{\varphi} = \nabla \varphi_z(x, y) \times \hat{\mathbf{i}}_z \tag{3.17}$$

After replacing (3.16) and (3.17) in (3.15), and considering $dV = dSdz$, we have

$$I_1 = \int_0^1 \int_\Omega (\nabla \varphi_z \times \hat{\mathbf{i}}_z) \cdot \nu (\nabla E_z \times \hat{\mathbf{i}}_z) dSdz = \int_\Omega (\nabla \varphi_z \times \hat{\mathbf{i}}_z) \cdot \nu (\nabla E_z \times \hat{\mathbf{i}}_z) dS. \tag{3.18}$$

We notice that

$$(\mathbf{a} \times \hat{\mathbf{i}}_z) \cdot \nu (\mathbf{b} \times \hat{\mathbf{i}}_z) = \mathbf{a}^T \begin{bmatrix} 0 & -1 \\ +1 & 0 \end{bmatrix} \nu_T \begin{bmatrix} 0 & 1 \\ -1 & 0 \end{bmatrix} \mathbf{b}, \tag{3.19}$$

Also, we notice that

$$\begin{bmatrix} 0 & -1 \\ +1 & 0 \end{bmatrix} \nu \begin{bmatrix} 0 & 1 \\ -1 & 0 \end{bmatrix} = \begin{bmatrix} \nu_{yy} & -\nu_{yx} \\ -\nu_{xy} & \nu_{xx} \end{bmatrix} = \det(\nu_T) \nu_T^{-T} = \frac{\mu_T^T}{\det(\mu_T)}, \tag{3.20}$$

being $\det(\cdot)$ the determinant of a matrix. Therefore, I_1 becomes:

$$I_1 = \int_\Omega \nabla \varphi_z \cdot \frac{\mu_T^T}{\det(\mu_T)} \nabla E_z dS. \tag{3.21}$$

Concerning the second integral in (3.11), i.e. [1]:

$$I_2 = \int_{\Omega_e} \nabla \cdot (\boldsymbol{\varphi} \times \nu \nabla \times \mathbf{E}_s) dV \tag{3.22}$$

[1] Here the subscript "-" means that the physical quantities on a closed surface are defined as the limit from the interior.

it is worth noting that, by using the divergence theorem, we have:

$$I_2 = \int_{\partial\Omega_e^-} (\boldsymbol{\varphi} \times \nu\nabla \times \mathbf{E}) \cdot \hat{\mathbf{n}} dS. \tag{3.23}$$

From $\partial\Omega_e = S_0 \cup S_1 \cup S_l$, (3.22) becomes:

$$I_2 = \int_{S_0^-} (\boldsymbol{\varphi} \times \nu\nabla \times \mathbf{E}) \cdot \hat{\mathbf{n}} dS + \int_{S_1^-} (\boldsymbol{\varphi} \times \nu\nabla \times \mathbf{E}) \cdot \hat{\mathbf{n}} dS + \int_{S_l^-} (\boldsymbol{\varphi} \times \nu\nabla \times \mathbf{E}) \cdot \hat{\mathbf{n}} dS \tag{3.24}$$

Since the normal vectors are equal and opposite on S_0^- and S_1^-,as shown in Figure 3.2 the

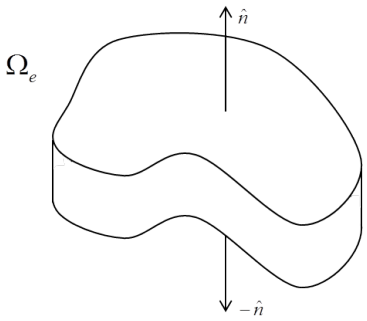

Figure 3.2: The normal vectors of an arbitrarily shaped object Ω_e

first two integrals cancel:

$$\begin{aligned} I_2 &= \int_{S_l^-} (\boldsymbol{\varphi} \times \nu\nabla \times \mathbf{E}) \cdot \hat{\mathbf{n}} dS \\ &= \int_{S_l} \varphi_z \hat{\mathbf{i}}_z \times \nu(\nabla E_z \times \hat{\mathbf{i}}_z) \cdot \hat{\mathbf{n}} dS \\ &= \int_{S_l} (\hat{\mathbf{n}} \times \varphi_z \hat{\mathbf{i}}_z) \cdot \nu(\nabla E_z \times \hat{\mathbf{i}}_z) dS. \end{aligned} \tag{3.25}$$

From dS =dldz we have:

$$I_2 = \int_{\partial\Omega^-} (\hat{\mathbf{n}} \times \varphi_z \hat{\mathbf{i}}_z) \cdot \nu(\nabla E_z \times \hat{\mathbf{i}}_z) dl. \tag{3.26}$$

Eventually, we consider the third integral in (3.11). Specifically, from $dV = dSdz$ we have

$$I_3 = \omega^2 \int_{\Omega_e} \boldsymbol{\varphi} \cdot \varepsilon \mathbf{E} dV = \omega^2 \int_{\Omega} \boldsymbol{\varphi} \cdot \varepsilon \mathbf{E} dS \tag{3.27}$$

Since both $\boldsymbol{\varphi}$ and $\mathbf{E}$ are z-directed, we have that the argument of the integral appearing in (3.27) is:

$$\boldsymbol{\varphi} \cdot \varepsilon \mathbf{E} = \varepsilon_{zz} \varphi_z E_z, \tag{3.28}$$

thus

$$I_3 = \omega^2 \int_\Omega \varepsilon_{zz}\varphi_z E_z dS. \tag{3.29}$$

Finally, equation (3.11) becomes:

$$\int_\Omega \nabla\varphi_z \cdot \frac{\mu_T^T}{\det(\mu_T)}\nabla E_z dS - \int_{\partial\Omega^-} (\hat{\mathbf{n}} \times \varphi_z \hat{\mathbf{i}}_z) \cdot \nu(\nabla E_z \times \hat{\mathbf{i}}_z) dl - \omega^2 \int_\Omega \varepsilon_{zz}\varphi_z E_z dS = - j\omega \int_\Omega \varphi_z J_0 dS \tag{3.30}$$

Let the scattered field be definend, as usual, as $\mathbf{E}^s = \mathbf{E} - \mathbf{E}^i$, where $\mathbf{E}^i$ is the incident field. Then, it follows that:

$$\begin{aligned} &\int_\Omega \nabla\varphi_z \cdot \frac{\mu_T^T}{\det(\mu_T)}\nabla(E_z^i + E_z^s) dS - \int_{\partial\Omega^-} (\hat{\mathbf{n}} \times \varphi_z \hat{\mathbf{i}}_z) \cdot \nu(\nabla(E_z^i + E_z^s) \times \hat{\mathbf{i}}_z) dl + \\ &- \omega^2 \int_\Omega \varepsilon_{zz}\varphi_z (E_z^i + E_z^s) dS = -j\omega \int_\Omega \varphi_z J_0 dS \end{aligned} \tag{3.31}$$

from which:

$$\int_\Omega \nabla\varphi_z \cdot \frac{\mu_T^T}{\det(\mu_T)}\nabla E_z^s dS - \int_{\partial\Omega^-} (\hat{\mathbf{n}} \times \varphi_z \hat{\mathbf{i}}_z) \cdot \mu^{-1}(\nabla E_z^s \times \hat{\mathbf{i}}_z) dl - \omega^2 \int_\Omega \varepsilon_{zz}\varphi_z E_z^s dS = f \tag{3.32}$$

being:

$$\begin{aligned} f \;=\; & -\int_\Omega \nabla\varphi_z \cdot \frac{\mu_T^T}{\det(\mu_T)}\nabla E_z^i dS + \int_{\partial\Omega^-} (\hat{\mathbf{n}} \times \varphi_z \hat{\mathbf{i}}_z) \cdot \mu^{-1}(\nabla E_z^i \times \hat{\mathbf{i}}_z) dl + \\ & + \omega^2 \int_\Omega \varepsilon_{zz}\varphi_z E_z^i dS - j\omega \int_\Omega \varphi_z J_0 dS. \end{aligned} \tag{3.33}$$

It is worth noting that any anisotropy of ε in the x, y plane is filtered out.

We conclude this section by noting that the incident field satisfies

$$\int_\Omega \nabla\varphi_z \cdot \mu_0^{-1}\nabla E_z^i dS - \int_{\partial\Omega^-} (\hat{\mathbf{n}} \times \varphi_z \hat{\mathbf{i}}_z) \cdot \mu_0^{-1}(\nabla E_z^i \times \hat{\mathbf{i}}_z) dl - \omega^2 \int_\Omega \varepsilon_0\varphi_z E_z^i dS - j\omega \int_\Omega \varphi_z J_0 dS \tag{3.34}$$

thus

$$\begin{aligned} f = -\int_\Omega \nabla\varphi_z \cdot \left(\frac{\mu_T^T}{\det(\mu_T)} - \mu_0^{-1} I\right) \nabla E_z^i dS \\ + \int_{\partial\Omega^-} (\hat{\mathbf{n}} \times \varphi_z \hat{\mathbf{i}}_z) \cdot \left(\mu^{-1} - \mu_0^{-1} I\right) (\nabla E_z^i \times \hat{\mathbf{i}}_z) dl \\ + \omega^2 \int_\Omega (\varepsilon_{zz} - \varepsilon_0)\, \varphi_z E_z^i dS\,. \end{aligned} \tag{3.35}$$

Equation (3.35) provides the source term f of (3.32) in terms of the incident field and the variation of the material properties.

3.2.3 Dirichlet-to-Neumann operator

The second integral appearing on the left-hand side of (3.32) can be written as

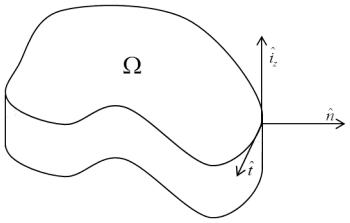

Figure 3.3: The vector product $\hat{\mathbf{n}} \times \hat{\mathbf{i}}_z = \hat{\mathbf{t}}$ on $\partial\Omega$, where t is the unit tangent vector

$$\begin{aligned}
\int_{\partial\Omega^-} \varphi_z(\hat{\mathbf{n}} \times \hat{\mathbf{i}}_z) \cdot \mu^{-1}(\nabla E_z^s \times \hat{\mathbf{i}}_z)\mathrm{d}l &= \int_{\partial\Omega^-} \varphi_z \hat{\mathbf{t}} \cdot \mu^{-1}(-j\omega \mathbf{B}^s)\mathrm{d}l \\
&= -j\omega \int_{\partial\Omega} \varphi_z \left(\hat{\mathbf{t}} \cdot \mathbf{H}^s\right)_- \mathrm{d}l \\
&= -j\omega \int_{\partial\Omega} \varphi_z \left(\hat{\mathbf{t}} \cdot \mathbf{H}^s\right)_+ \mathrm{d}l \\
&= -j\omega \int_{\partial\Omega} \varphi_z \Lambda_H \left[(E_z^s)_+\right] \mathrm{d}l \\
&= -j\omega \int_{\partial\Omega} \varphi_z \Lambda_H \left[(E_z^s)_-\right] \mathrm{d}l \qquad (3.36)
\end{aligned}$$

where we exploited that $\hat{\mathbf{n}} \times \hat{\mathbf{i}}_z = \hat{\mathbf{t}}$ on $\partial\Omega$ and Λ_H is the operator mapping the tangential component of the electric field on $\partial\Omega$ onto the tangential component of the magnetic field on $\partial\Omega$ (Dirichlet-to-Neumann operator):

$$\Lambda_H : (E_z^s)_+ |_{\partial\Omega} \longrightarrow \left(\hat{\mathbf{t}} \cdot \mathbf{H}^s\right)_+ |_{\partial\Omega}, \qquad (3.37)$$

and we have exploited the continuity of the tangential component of the field $\mathbf{E}$ and $\mathbf{H}$ across $\partial\Omega$.

It is worth noting that

$$\begin{aligned}\left(\hat{\mathbf{t}}\cdot\mathbf{H}^s\right)_+ &= -\frac{1}{j\omega\mu_0}\left(\hat{\mathbf{t}}\cdot\nabla\times\mathbf{E}^s\right)_+ \\ &= -\frac{1}{j\omega\mu_0}\left(\nabla E_z^s\right)_+\cdot\hat{\mathbf{i}}_z\times\hat{\mathbf{t}} \\ &= -\frac{1}{j\omega\mu_0}\left(\partial_n E_z^s\right)_+ \end{aligned} \tag{3.38}$$

i.e.

$$\Lambda_H = -\frac{1}{j\omega\mu_0}\Lambda \tag{3.39}$$

being

$$\Lambda : \left(E_z^s\right)_+|_{\partial\Omega} \longrightarrow \left(\partial_n E_z^s\right)_+|_{\partial\Omega}, \tag{3.40}$$

therefore

$$\int_{\partial\Omega^-}\varphi_z(\hat{\mathbf{n}}\times\hat{\mathbf{i}}_z)\cdot\mu^{-1}(\nabla E_z^s\times\hat{\mathbf{i}}_z)\mathrm{d}l = \frac{1}{\mu_0}\int_{\partial\Omega}\varphi_z\Lambda\left[\left(E_z^s\right)_-\right]\mathrm{d}l. \tag{3.41}$$

The governing equation (3.32) is, consequently:

$$\int_\Omega\nabla\varphi_z\cdot\frac{\mu_T^T}{\det(\mu_T)}\nabla E_z^s dS - \frac{1}{\mu_0}\int_{\partial\Omega}\varphi_z\Lambda\left[\left(E_z^s\right)_-\right]\mathrm{d}l - \omega^2\int_\Omega\varepsilon_{zz}\varphi_z E_z^s dS = f. \tag{3.42}$$

We conclude this section by recalling that the exterior problem, with respect to Ω, is defined as follows:

$$\nabla^2 E_z^s + k_0^2 E_z^s = 0 \quad \text{in} \quad \mathbb{R}^2\backslash\Omega \tag{3.43}$$

$$E_z^s = g \quad \text{on} \quad \partial\Omega \tag{3.44}$$

$$\lim_{r\to+\infty} r^{1/2}(\partial_r E_z^s + jk_0 E_z^s) = 0. \tag{3.45}$$

3.3 TEz illumination

In this section we examine the scattering of TE waves from a cylindrical scatterer of arbitrary cross section (invariant along the z-axis) by a differential formulation coupled with the Dirichlet-to-Neumann (DtN) operator. The scatterer may be anisotropic.

3.3.1 Forward problem

Here we assume the source current density is directed in the transverse x, y plane, i.e. $\mathbf{J}_0 = J_{0x}(x,y)\,\hat{\mathbf{i}}_x + J_{0y}(x,y)\,\hat{\mathbf{i}}_y$, we have a TE wave, where both the magnetic flux density and the magnetic field are directed along the z-axis, whereas the electric field and the electric displacement field are directed in the x, y plane. In this setting, it is convenient to assume as unknown the magnetic field that is described by one component only: $\mathbf{H} = H_z(x,y)\hat{\mathbf{i}}_z$. In addition, we notice that since $\mathbf{H}$ is div-conforming, it turns out that $H_z \in H^1(\Omega)$. From Maxwell's equations we have that the magnetic field satisfies:

$$\nabla \times \frac{\varepsilon^{-1}}{j\omega}(\nabla \times \mathbf{H} - \mathbf{J}_0) = -j\omega\mu\mathbf{H} \tag{3.46}$$

that is:

$$\nabla \times (\varepsilon^{-1}\nabla \times \mathbf{H}) - \omega^2\mu\mathbf{H} = \nabla \times \left(\varepsilon^{-1}\mathbf{J}_0\right) \tag{3.47}$$

3.3.2 Weak formulation

The weak form of (3.47) in Ω_e is given by:

$$\int_{\Omega_e} \boldsymbol{\varphi} \cdot \nabla \times (\varepsilon^{-1}\nabla \times \mathbf{H})\mathrm{d}V - \omega^2 \int_{\Omega_e} \boldsymbol{\varphi} \cdot \mu\mathbf{H}\mathrm{d}V = \int_{\Omega_e} \boldsymbol{\varphi} \cdot \nabla \times \left(\varepsilon^{-1}\mathbf{J}_0\right)\mathrm{d}V \tag{3.48}$$

We assume the function $\boldsymbol{\varphi} \in H(rot, \Omega_e)$ be defined as follows:

$$\boldsymbol{\varphi} = \varphi_z(x,y)\hat{\mathbf{i}}_z \tag{3.49}$$

being $\varphi_z \in H^1(\Omega)$. Using the vector identity:

$$\nabla \cdot \left(\boldsymbol{\varphi} \times \varepsilon^{-1}\nabla \times \mathbf{H}\right) = \nabla \times \boldsymbol{\varphi} \cdot \varepsilon^{-1}\nabla \times \mathbf{H} - \boldsymbol{\varphi} \cdot \nabla \times (\varepsilon^{-1}\nabla \times \mathbf{H}) \tag{3.50}$$

we have[2]:

$$\begin{aligned}\int_{\Omega_e} \nabla \times \boldsymbol{\varphi} \cdot \varepsilon^{-1}\nabla \times \mathbf{H}\mathrm{d}V - \int_{\partial\Omega_e} \boldsymbol{\varphi}_- \times \varepsilon_-^{-1}(\nabla \times \mathbf{H})_- \cdot \hat{\mathbf{n}}\mathrm{d}S \\ -\omega^2 \int_{\Omega_e} \boldsymbol{\varphi} \cdot \mu\mathbf{H}\mathrm{d}V = \int_{\Omega_e} \boldsymbol{\varphi} \cdot \nabla \times \left(\varepsilon^{-1}\mathbf{J}_0\right)\mathrm{d}V\end{aligned} \tag{3.51}$$

[2]Here the subscript "-" means that the physical quantities on a closed surface are defined as the limit from the interior.

Let us consider the first integral in (3.51):

$$I_1 = \int_{\Omega_e} \nabla \times \boldsymbol{\varphi} \cdot \varepsilon^{-1} \nabla \times \mathbf{H} \mathrm{d}V \tag{3.52}$$

We notice that:

$$\nabla \times \mathbf{H} = \nabla H_z(x, y) \times \hat{\mathbf{i}}_z \tag{3.53}$$

and, similary,

$$\nabla \times \boldsymbol{\varphi} = \nabla \varphi_z(x, y) \times \hat{\mathbf{i}}_z, \tag{3.54}$$

thus, after replacing in (3.51) and considering that $\mathrm{d}V = \mathrm{d}S\mathrm{d}z$, we have

$$I_1 = \int_0^1 \int_\Omega \nabla \varphi_z \times \hat{\mathbf{i}}_z \cdot \varepsilon^{-1} \left(\nabla H_z \times \hat{\mathbf{i}}_z \right) \mathrm{d}S\mathrm{d}z = \int_\Omega \nabla \varphi_z \times \hat{\mathbf{i}}_z \cdot \varepsilon^{-1} \left(\nabla H_z \times \hat{\mathbf{i}}_z \right) \mathrm{d}S \tag{3.55}$$

We notice that:

$$\left(\mathbf{a} \times \hat{\mathbf{i}}_z \right) \cdot \varepsilon^{-1} \left(\mathbf{b} \times \hat{\mathbf{i}}_z \right) = \mathbf{a}_T \cdot \frac{\varepsilon_T^T}{\det(\varepsilon_T)} \mathbf{b}_T \tag{3.56}$$

The integral I_1 as already seen in the TMz case, becomes:

$$I_1 = \int_\Omega \nabla \varphi_z \cdot \frac{\varepsilon_T^T}{\det(\varepsilon_T)} \nabla H_z \mathrm{d}S. \tag{3.57}$$

Concerning the second integral in (3.51)

$$I_2 = \int_{\partial \Omega_e^-} \boldsymbol{\varphi} \times \varepsilon^{-1} (\nabla \times \mathbf{H}) \cdot \hat{\mathbf{n}} \mathrm{d}S \tag{3.58}$$

it can be cast as

$$\begin{aligned} I_2 = & \int_{S_0^-} \boldsymbol{\varphi} \times \varepsilon^{-1} (\nabla \times \mathbf{H}) \cdot \hat{\mathbf{n}} \mathrm{d}S + \int_{S_1^-} \boldsymbol{\varphi} \times \varepsilon^{-1} (\nabla \times \mathbf{H}) \cdot \hat{\mathbf{n}} \mathrm{d}S \\ & + \int_{S_l^-} \boldsymbol{\varphi} \times \varepsilon^{-1} (\nabla \times \mathbf{H}) \cdot \hat{\mathbf{n}} \mathrm{d}S. \end{aligned} \tag{3.59}$$

The first two integrals are equal apart from the sign, because the normal vectors are equal and opposite on S_0 and S_1, thus:

$$\begin{aligned} I_2 &= \int_{S_l^-} \varphi_z \hat{\mathbf{i}}_z \times \varepsilon^{-1} \left[(\nabla H_z) \times \hat{\mathbf{i}}_z \right] \cdot \hat{\mathbf{n}} \mathrm{d}S \\ &= \int_{S_l^-} \varphi_z \left(\hat{\mathbf{n}} \times \hat{\mathbf{i}}_z \right) \cdot \varepsilon^{-1} \left[(\nabla H_z) \times \hat{\mathbf{i}}_z \right] \mathrm{d}S. \end{aligned} \tag{3.60}$$

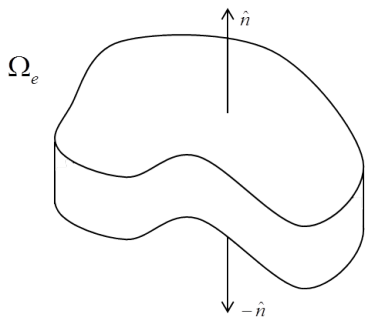

From $\mathrm{d}S = \mathrm{d}l\mathrm{d}z$ we have[3]:

$$I_2 = \int_{\partial\Omega^-} \varphi_z \left(\hat{\mathbf{n}} \times \hat{\mathbf{i}}_z\right) \cdot \varepsilon^{-1} \left[(\nabla H_z) \times \hat{\mathbf{i}}_z\right] \mathrm{d}l. \tag{3.61}$$

Eventually, we consider the third integral of (3.51). Specifically,from $\mathrm{d}V = \mathrm{d}S\mathrm{d}z$ we have:

$$I_3 = \omega^2 \int_{\Omega_e} \boldsymbol{\varphi} \cdot \mu \mathbf{H} \mathrm{d}V = \omega^2 \int_{\Omega} \boldsymbol{\varphi} \cdot \mu \mathbf{H} \mathrm{d}S \tag{3.62}$$

since both $\boldsymbol{\varphi}$ and $\mathbf{H}$ are z-directed, we have that the argument of the integral appearing in (3.62) is:

$$\boldsymbol{\varphi} \cdot \mu \mathbf{H} = \mu_{zz} \varphi_z H_z \tag{3.63}$$

thus

$$I_3 = \omega^2 \int_{\Omega} \mu_{zz} \varphi_z H_z \mathrm{d}S \tag{3.64}$$

The fourth integral of (3.51), i.e the source term

$$I_4 = \int_{\Omega_e} \boldsymbol{\varphi} \cdot \nabla \times \left(\varepsilon^{-1} \mathbf{J}_0\right) \mathrm{d}V \tag{3.65}$$

Using the vector identity

$$\nabla \cdot \left(\varepsilon^{-1} \mathbf{J}_0 \times \boldsymbol{\varphi}\right) = \boldsymbol{\varphi} \cdot \nabla \times \left(\varepsilon^{-1} \mathbf{J}_0\right) - \varepsilon^{-1} \mathbf{J}_0 \cdot (\nabla \times \boldsymbol{\varphi}) \tag{3.66}$$

we have

$$I_4 = \int_{\partial\Omega_e^-} \varepsilon^{-1} (\mathbf{J}_0) \times \boldsymbol{\varphi} \cdot \hat{\mathbf{n}} \mathrm{d}S + \int_{\Omega_e} \varepsilon^{-1} \mathbf{J}_0 \cdot \nabla \times \boldsymbol{\varphi} \mathrm{d}V. \tag{3.67}$$

[3]We also notice that $I_2 = \int_{\partial\Omega} (\varphi_z)_- \hat{\mathbf{n}} \cdot \frac{\varepsilon_T^T}{\det(\varepsilon_T)} (\nabla H_z)_- \mathrm{d}l$.

We notice that

$$\begin{aligned}\int_{\partial\Omega_e^-} \varepsilon^{-1}\left(\mathbf{J}_0\right)\times\boldsymbol{\varphi}\cdot\hat{\mathbf{n}}\mathrm{d}S &= \int_{\partial\Omega_e^-} \varphi_z\hat{\mathbf{i}}_z\times\hat{\mathbf{n}}\cdot\left(\varepsilon^{-1}\mathbf{J}_0\right)\mathrm{d}S\\ &= \int_{S_l^-} \varphi_z\hat{\mathbf{i}}_z\times\hat{\mathbf{n}}\cdot\left(\varepsilon^{-1}\mathbf{J}_0\right)\mathrm{d}S\\ &= \int_{\partial\Omega^-} \varphi_z\hat{\mathbf{i}}_z\times\hat{\mathbf{n}}\cdot\left(\varepsilon^{-1}\mathbf{J}_0\right)\mathrm{d}l \qquad (3.68)\end{aligned}$$

because $\hat{\mathbf{n}}=\pm\hat{\mathbf{i}}_z$ on $S_0\cup S_1$ and $\mathrm{d}S=\mathrm{d}z\mathrm{d}l$ on S_l. Therefore

$$\begin{aligned}I_4 &= \int_{\partial\Omega^-} \varphi_z\hat{\mathbf{i}}_z\times\hat{\mathbf{n}}\cdot\left(\varepsilon^{-1}\mathbf{J}_0\right)\mathrm{d}l+\int_\Omega \varepsilon^{-1}\mathbf{J}_0\cdot\nabla\times\boldsymbol{\varphi}\mathrm{d}S\\ &= \int_{\partial\Omega^-} \varphi_z\hat{\mathbf{i}}_z\times\hat{\mathbf{n}}\cdot\left(\varepsilon^{-1}\mathbf{J}_0\right)\mathrm{d}l+\int_\Omega \varepsilon^{-1}\mathbf{J}_0\cdot\nabla\varphi_z\times\hat{\mathbf{i}}_z\mathrm{d}S\\ &= \int_{\partial\Omega^-} \varphi_z\hat{\mathbf{i}}_z\times\hat{\mathbf{n}}\cdot\left(\varepsilon^{-1}\mathbf{J}_0\right)\mathrm{d}l+\int_\Omega \nabla\varphi_z\cdot\hat{\mathbf{i}}_z\times\varepsilon^{-1}\mathbf{J}_0\mathrm{d}S. \qquad (3.69)\end{aligned}$$

Summing up, equation (3.51) becomes:

$$\begin{aligned}&\int_\Omega \nabla\varphi_z\cdot\frac{\varepsilon_T^T}{\det(\varepsilon_T)}\nabla H_z\mathrm{d}S\\ &\qquad -\int_{\partial\Omega^-}\varphi_z\left(\hat{\mathbf{n}}\times\hat{\mathbf{i}}_z\right)\cdot\varepsilon^{-1}\left[\left(\nabla H_z\right)\times\hat{\mathbf{i}}_z\right]\mathrm{d}l\\ &\qquad\qquad -\omega^2\int_\Omega \mu_{zz}\varphi_z H_z\mathrm{d}S\\ &\qquad =\int_{\partial\Omega^-}\varphi_z\left(\hat{\mathbf{i}}_z\times\hat{\mathbf{n}}\right)\cdot\left(\varepsilon^{-1}\mathbf{J}_0\right)\mathrm{d}l+\int_\Omega\nabla\varphi_z\cdot\hat{\mathbf{i}}_z\times\varepsilon^{-1}\mathbf{J}_0\mathrm{d}S. \qquad (3.70)\end{aligned}$$

Let the scattered field be defined, as usual, as $\mathbf{H}^s=\mathbf{H}-\mathbf{H}^i$, where $\mathbf{H}^i$ is the incident field . Then, it follows that:

$$\begin{aligned}&\int_\Omega \nabla\varphi_z\cdot\frac{\varepsilon_T^T}{\det(\varepsilon_T)}\nabla\left(H_z^i+H_z^s\right)\mathrm{d}S\\ &\qquad -\int_{\partial\Omega^-}\varphi_z\left(\hat{\mathbf{n}}\times\hat{\mathbf{i}}_z\right)\cdot\varepsilon^{-1}\left[\nabla\left(H_z^i+H_z^s\right)\times\hat{\mathbf{i}}_z\right]\mathrm{d}l\\ &\qquad\qquad -\omega^2\int_\Omega \mu_{zz}\varphi_z\left(H_z^i+H_z^s\right)\mathrm{d}S\\ &\qquad =\int_{\partial\Omega^-}\varphi_z\left(\hat{\mathbf{i}}_z\times\hat{\mathbf{n}}\right)\cdot\left(\varepsilon^{-1}\mathbf{J}_0\right)\mathrm{d}l+\int_\Omega\nabla\varphi_z\cdot\hat{\mathbf{i}}_z\times\varepsilon^{-1}\mathbf{J}_0\mathrm{d}S \qquad (3.71)\end{aligned}$$

thus

$$\int_{\Omega} \nabla\varphi_z \cdot \frac{\varepsilon_T^T}{\det(\varepsilon_T)} \nabla H_z^s \mathrm{d}S - \int_{\partial\Omega^-} \varphi_z \left(\hat{\mathbf{n}} \times \hat{\mathbf{i}}_z\right) \cdot \varepsilon^{-1} \left[(\nabla H_z^s) \times \hat{\mathbf{i}}_z\right] \mathrm{d}l - \omega^2 \int_{\Omega} \mu_{zz}\varphi_z H_z^s \mathrm{d}S = f \quad (3.72)$$

where

$$f = \int_{\partial\Omega^-} \varphi_z \left(\hat{\mathbf{i}}_z \times \hat{\mathbf{n}}\right) \cdot \left(\varepsilon^{-1}\mathbf{J}_0\right) \mathrm{d}l + \int_{\Omega} \nabla\varphi_z \cdot \hat{\mathbf{i}}_z \times \varepsilon^{-1}\mathbf{J}_0 \mathrm{d}S$$
$$\int_{\Omega} \nabla\varphi_z \cdot \frac{\varepsilon_T^T}{\det(\varepsilon_T)} \nabla H_z^i \mathrm{d}S + \int_{\partial\Omega^-} \varphi_z \left(\hat{\mathbf{n}} \times \hat{\mathbf{i}}_z\right) \cdot \varepsilon^{-1} \left(\nabla H_z^i \times \hat{\mathbf{i}}_z\right) \mathrm{d}l + \omega^2 \int_{\Omega} \mu_{zz}\varphi_z H_z^i \mathrm{d}S. \quad (3.73)$$

By noting that the incident field satisfies

$$\int_{\Omega} \nabla\varphi_z \cdot \varepsilon_0^{-1} \nabla H_z \mathrm{d}S - \int_{\partial\Omega^-} \varphi_z \left(\hat{\mathbf{n}} \times \hat{\mathbf{i}}_z\right) \cdot \varepsilon_0^{-1} \left(\nabla H_z \times \hat{\mathbf{i}}_z\right) \mathrm{d}l - \omega^2 \int_{\Omega} \mu_0\varphi_z H_z \mathrm{d}S$$
$$= \int_{\partial\Omega^-} \varphi_z \left(\hat{\mathbf{i}}_z \times \hat{\mathbf{n}}\right) \cdot \left(\varepsilon_0^{-1}\mathbf{J}_0\right) \mathrm{d}l + \int_{\Omega} \nabla\varphi_z \cdot \hat{\mathbf{i}}_z \times \varepsilon_0^{-1}\mathbf{J}_0 \mathrm{d}S, \quad (3.74)$$

we have

$$f = \int_{\partial\Omega^-} \varphi_z \left(\hat{\mathbf{i}}_z \times \hat{\mathbf{n}}\right) \cdot \left(\Delta\left(\varepsilon^{-1}\right)\mathbf{J}_0\right) \mathrm{d}l + \int_{\Omega} \nabla\varphi_z \cdot \hat{\mathbf{i}}_z \times \Delta\left(\varepsilon^{-1}\right)\mathbf{J}_0 \mathrm{d}S$$
$$\int_{\Omega} \nabla\varphi_z \cdot \Delta\left(\frac{\varepsilon_T^T}{\det(\varepsilon_T)}\right) \nabla H_z^i \mathrm{d}S + \int_{\partial\Omega^-} \varphi_z \left(\hat{\mathbf{n}} \times \hat{\mathbf{i}}_z\right) \cdot \Delta\left(\varepsilon^{-1}\right) \left(\nabla H_z^i \times \hat{\mathbf{i}}_z\right) \mathrm{d}l + \omega^2 \int_{\Omega} \Delta\mu_{zz}\varphi_z H_z^i \mathrm{d}S \quad (3.75)$$

being

$$\Delta\left(\varepsilon^{-1}\right) = \varepsilon^{-1} - \varepsilon_0^{-1} I \quad (3.76)$$

$$\Delta\left(\frac{\varepsilon_T^T}{\det(\varepsilon_T)}\right) = \frac{\varepsilon_T^T}{\det(\varepsilon_T)} - \varepsilon_0^{-1} I \quad (3.77)$$

$$\Delta\mu_{zz} = \mu_{zz} - \mu_0 \quad (3.78)$$

where I is the identity tensor.

3.3.3 Dirichlet-to-Neumann operator

The quantity $(\hat{\mathbf{n}} \times \hat{\mathbf{i}}_z) = \hat{\mathbf{t}}$ is the unit tangent vector on $\partial\Omega$.The second integral of (3.72) can be written as:

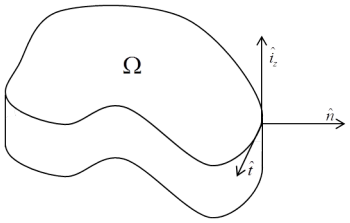

$$\begin{aligned}
\int_{\partial\Omega^-} \varphi_z(\hat{\mathbf{n}} \times \hat{\mathbf{i}}_z) \cdot \varepsilon^{-1}(\nabla H_z^s \times \hat{\mathbf{i}}_z)\mathrm{d}l &= \int_{\partial\Omega^-} \varphi_z \hat{\mathbf{t}} \cdot \varepsilon^{-1}(j\omega\varepsilon\mathbf{E}^s + \mathbf{J}_0)\mathrm{d}l \qquad (3.79)\\
&= j\omega \int_{\partial\Omega} \varphi_z \left(\hat{\mathbf{t}} \cdot \mathbf{E}^s\right)_- \mathrm{d}l + \int_{\partial\Omega^-} \varphi_z \hat{\mathbf{t}} \cdot \varepsilon^{-1}\mathbf{J}_0\mathrm{d}l\\
&= j\omega \int_{\partial\Omega} \varphi_z \left(\hat{\mathbf{t}} \cdot \mathbf{E}^s\right)_+ \mathrm{d}l + \int_{\partial\Omega^-} \varphi_z \hat{\mathbf{t}} \cdot \varepsilon^{-1}\mathbf{J}_0\mathrm{d}l\\
&= j\omega \int_{\partial\Omega} \varphi_z \Lambda_E \left[(H_z^s)_+\right] \mathrm{d}l + \int_{\partial\Omega^-} \varphi_z \hat{\mathbf{t}} \cdot \varepsilon^{-1}\mathbf{J}_0\mathrm{d}l\\
&= j\omega \int_{\partial\Omega} \varphi_z \Lambda_E \left[(H_z^s)_-\right] \mathrm{d}l + \int_{\partial\Omega^-} \varphi_z \hat{\mathbf{t}} \cdot \varepsilon^{-1}\mathbf{J}_0\mathrm{d}l
\end{aligned}$$

where Λ_H is the operator mapping the tangent component of the magnetic field on $\partial\Omega$ onto the tangent component of the electric field on $\partial\Omega$ (Dirichlet-to-Neumann operator):

$$\Lambda_E : (H_z^s)_+ |_{\partial\Omega} \longrightarrow \left(\hat{\mathbf{t}} \cdot \mathbf{E}^s\right)_+ |_{\partial\Omega}, \qquad (3.80)$$

Moreover, it is worth noting that

$$\begin{aligned}
\left(\hat{\mathbf{t}} \cdot \mathbf{E}^s\right)_+ &= \frac{1}{j\omega\varepsilon_0} \left(\hat{\mathbf{t}} \cdot \nabla \times \mathbf{H}^s\right)_+\\
&= \frac{1}{j\omega\varepsilon_0} \left(\nabla H_z^s\right)_+ \cdot \hat{\mathbf{i}}_z \times \hat{\mathbf{t}}\\
&= \frac{1}{j\omega\varepsilon_0} \left(\partial_n H_z^s\right)_+ \qquad (3.81)
\end{aligned}$$

i.e.,

$$\Lambda_H = \frac{1}{j\omega\varepsilon_0}\Lambda \qquad (3.82)$$

being

$$\Lambda : (H_z^s) |_{\partial\Omega^+} \longrightarrow (\partial_n H_z^s) |_{\partial\Omega^+}, \qquad (3.83)$$

therefore

$$\int_{\partial\Omega^-} \varphi_z(\hat{\mathbf{n}}\times\hat{\mathbf{i}}_z)\cdot\varepsilon^{-1}(\nabla H_z^s\times\hat{\mathbf{i}}_z)\mathrm{d}l = \frac{1}{\varepsilon_0}\int_{\partial\Omega^-}\varphi_z\Lambda\left(H_z^s\right)\mathrm{d}l + \int_{\partial\Omega^-}\varphi_z\hat{\mathbf{t}}\cdot\varepsilon^{-1}\mathbf{J}_0\mathrm{d}l. \quad (3.84)$$

The governing equation (3.72) is, consequently:

$$\int_\Omega \nabla\varphi_z\cdot\frac{\varepsilon_T^T}{\det(\varepsilon_T)}\nabla H_z^s dS - \frac{1}{\varepsilon_0}\int_{\partial\Omega^-}\varphi_z\Lambda\left(H_z^s\right)\mathrm{d}l - \omega^2\int_\Omega \mu_{zz}\varphi_z H_z^s dS = f \quad (3.85)$$

being:

$$\begin{aligned} f = &-\int_\Omega \nabla\varphi_z\cdot\frac{\varepsilon_T^T}{\det(\varepsilon_T)}\nabla H_z^i dS \\ &+\int_{\partial\Omega}(\hat{\mathbf{n}}\times\varphi_z\hat{\mathbf{i}}_z)\cdot(\varepsilon^{-1}\nabla H_z^i\times\hat{\mathbf{i}}_z)dl + \omega^2\int_\Omega\mu_{zz}\varphi_z H_z^i dS \\ &+\int_\Omega\nabla\varphi_z\cdot\hat{\mathbf{i}}_z\times\varepsilon^{-1}\mathbf{J}_0 dS + \int_{\partial\Omega^-}\varphi_z\hat{\mathbf{t}}\cdot\varepsilon^{-1}\mathbf{J}_0\mathrm{d}l \end{aligned} \quad (3.86)$$

We conclude this section by recalling that the exterior problem, with respect to Ω, is defined as follows:

$$\nabla^2 H_z^s + k_0^2 H_z^s = 0 \quad \text{in } \mathbb{R}^2\backslash\Omega \quad (3.87)$$

$$H_z^s = g \quad \text{on } \partial\Omega \quad (3.88)$$

$$\lim_{r\to+\infty} r^{1/2}\left(\partial_r H_z^s + jk_0 H_z^s\right) = 0. \quad (3.89)$$

Chapter 4

NUMERICAL MODEL

This chapter focuses on the numerical implementation of the formulation discussed in Chapter 2. The first part of the chapter starts with a brief introduction of the finite element theory. The numerical models for both the external and internal DtN operators are considered.

The DtN operators in their discrete form are represented by fully populated matrices. This is a serious issue when dealing with the Internal DtN operator. Indeed, we proved (4.3.1) that it does not reduce the computational cost with respect to the standard FEM. However, we found that the DtN operators corresponds to low-rank matrices. Therefore, we developed two sparsification approaches (4.4.1 and 4.4.3) to reduce the computational cost of the matrix-by-vector product. The first one is based on an analytical factorization of the DtN operators, the second one is based onto the Fast Fourier Transform (FFT) algorithm.

4.1 Finite Element method for the scattering problem

One of most widely used numerical methods to solve PDE is the finite element method (FEM). This method [47] is a numerical technique for finding approximate solutions of partial differential equations (PDE).

The three fundamental steps of the FEM method are:

1. write the PDE in weak form starting from the strong form

2. approximate the sought solution through an element of a finite dimensional linear space W^M.

3. impose the weak form for each test function belonging to the same spaces for W^M.

In finite element modeling, the problem of finding the solution of PDE problem is recasted as the problem of finding the solution of a linear algebraic system. About the first point, equations (2.6) and (2.20) are already written in weak form. Regarding the second point, considering a subspace W^M of finite dimension M and with basic functions $B_m = \{w_1, ..., w_M\}$ the scattered field can be expressed as follows:

$$w_s = \sum_{i=1}^{M} x_i \varphi_i(x, y) \tag{4.1}$$

where the φ_i's are linearly independent functions, so called 'shape functions' (or test functions) and x_i are the unknown coefficients (Degrees of Freedom, DoF), respectively.

In order to define the shape functions, we introduce the mesh discretization of a domain Ω, in term of partitioning sub-domains $T = \{\Omega_i, ..., \Omega_n\}$. Consider a two-dimensional domain, and a triangular partition T_r as shown in the figure 4.1, we can indicate with $P_1, P_2, ..., P_{N_i}$ the internal nodes of the partition T_r and with $P_{N_i+1}, P_{N_i+2}, ..., P_{N_i+N_j}$ the boundary nodes.

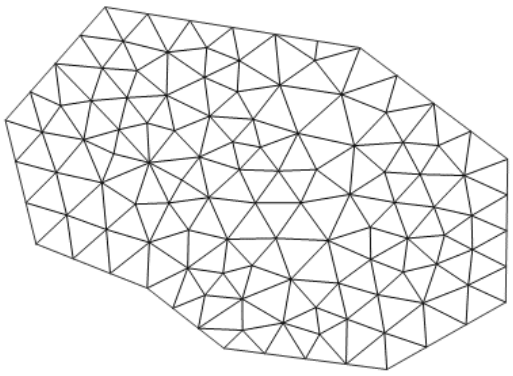

Figure 4.1: Meshing the domain Ω

A test function is associated with each node, and resulting in $M = N_i + N_j$ functions

$$w_1, w_2, ..., w_M. \tag{4.2}$$

The set of nodes, edges and triangles constitutes the mesh. A common choice to define the shape functions is to consider piecewise linear functions, "hat" functions (first order shape functions) such that:

$$\varphi_h(P_i) = \delta_{h,i} \tag{4.3}$$

where $\delta_{h,i}$ is the Kronecker symbol. The functions φ_h are only related to the mesh. Moreover the support of the basic function φ_h is the union of all triangles of T_r which have the node P_h as the vertex. Consider a triangle with vertices P_h, P_i, P_j and their coordinates

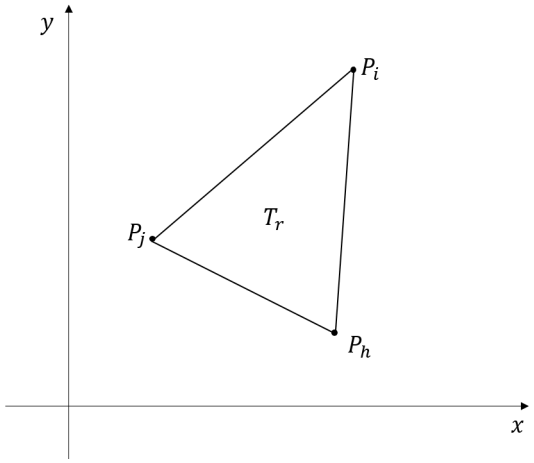

Figure 4.2: Generic mesh triangle

(x_h, y_h), (x_i, y_i), (x_j, y_j) respectively, as shown in the figure 4.2. The restriction of the test function w_h to the triangle T_r has the following analytical expression:

$$\varphi_h^r(x, y) = a_h^r x + b_h^r y + c_h^r \tag{4.4}$$

where

$$a_h^r = \frac{1}{2A_r}(y_i - y_h) \tag{4.5a}$$

$$b_h^r = \frac{1}{2A_r}(x_j - x_h) \tag{4.5b}$$

$$c_h^r = \frac{1}{2A_r}(x_i y_j - x_j y_i) \tag{4.5c}$$

and the area of the triangle T_r:

$$A_r = \frac{1}{2}\left[(x_i y_j - x_j y_i) + (x_j y_h - x_h y_j) + (x_h y_i - x_i y_h)\right] \tag{4.6}$$

similar analytical expressions can be obtained for w_i^r and w_j^r. The gradient of $w_h^r(x,y)$ is given by:

$$\bigtriangledown\varphi_h^r(x,y) = a_h^r\hat{x} + b_h^r\hat{y} \tag{4.7}$$

and the gradient of w_i^r and w_j^r are give by:

$$\bigtriangledown\varphi_i^r(x,y) = a_i^r\hat{x} + b_i^r\hat{y} \tag{4.8}$$

$$\bigtriangledown\varphi_j^r(x,y) = a_j^r\hat{x} + b_j^r\hat{y} \tag{4.9}$$

So far. we have completely defined the shape functions (step 2). The final step is to find the x_i's in (4.1). To this end, we impose the weak formulation for each shape function, which as matter of fact is a linear equation. Gathering all equations, we obtain a linear algebric system. Full details will be provided in the next sections.

4.2 Numerical model for the differential formulation coupled to the external DtN operator

The scattering problem, as explained in Chapter 2, can be solved numerically starting from the weak form of (2.2) given by (2.6). Using the guidelines of the FEM methods explained in section 4.1, we can obtain the discrete model. First, we express the unknown as

$$w^s = \sum_{i=1}^{N} x_i\varphi_i \tag{4.10}$$

where the shape functions are first-order isoparametric nodal elements, the x_n's are the unknown coefficients, the so-called Degrees of Freedom (DoF) and N is the total number of nodes of the finite element mesh. The (2.6) is the weak form of the (2.2) (step 1, see section 4.1). Then, the Galerkin approach is applied to (2.6) to obtain the following linear system of equations for the DoFs (step 3, see section 4.1):

$$(\boldsymbol{\Lambda} - \boldsymbol{A} + \boldsymbol{B})\boldsymbol{x} = \boldsymbol{f} \tag{4.11}$$

where

$$\Lambda_{h,i} = \int_{\partial B_R} \varphi_h(\Lambda_R\varphi_i)dl \tag{4.12}$$

$$A_{h,i} = \int_{B_R} \nabla\varphi_h \cdot \nabla\varphi_i dS \tag{4.13}$$

$$B_{h,i} = k^2 \int_{B_R} m^2 \varphi_h \varphi_i dS \tag{4.14}$$

$$f_h = -k^2 \int_{B_R} (m^2 - 1)\varphi_h w^i dS \tag{4.15}$$

It is convenient partitioning the unknowns DoFs in $\boldsymbol{x}_b$ and $\boldsymbol{x}_i$ which are related to the boundary and the internal nodes of the finite element mesh. In this way, we get:

$$\left(\begin{bmatrix} \boldsymbol{\Lambda}_{bb} & 0 \\ 0 & 0 \end{bmatrix} - \begin{bmatrix} \boldsymbol{A}_{bb} & \boldsymbol{A}_{bi} \\ \boldsymbol{A}_{ib} & \boldsymbol{A}_{ii} \end{bmatrix} + \begin{bmatrix} \boldsymbol{B}_{bb} & \boldsymbol{B}_{bi} \\ \boldsymbol{B}_{ib} & \boldsymbol{B}_{ii} \end{bmatrix} \right) \begin{bmatrix} \boldsymbol{x}_b \\ \boldsymbol{x}_i \end{bmatrix} = \begin{bmatrix} \boldsymbol{f}_b \\ \boldsymbol{f}_i \end{bmatrix} \tag{4.16}$$

A is the **stiffness matrix** of the system that can be calculated as:

$$\begin{aligned} A_{h,i} &= \int_{B_R} \nabla\varphi_h \cdot \nabla\varphi_i dS \\ &= \sum_{r=1}^{N_t} \int_{T_R} \nabla\varphi_h^r \cdot \nabla\varphi_i^r \\ &= \sum_{r=1}^{N_t} \left(a_h^{(r)} a_i^{(r)} + b_h^{(r)} b_i^{(r)} \right) A_r. \end{aligned} \tag{4.17}$$

where N_t is the number of triangles of the mesh. It is worth noticing that from the features of the shape functions coefficients $a_h^{(r)}$, $a_i^{(r)}$, $b_h^{(r)}$, $b_i^{(r)}$ are different from zero only in the r-th triangle and therefore only those triangles that have both vertices P_i and P_p in common contribute to the coefficient $A_{h,i}$. Hence the matrix A is sparse.

B is the **mass matrix** that can be calculated as follows [47]:

$$B_{h,i} = k^2 m^2 \int_{B_R} \varphi_h \varphi_i dS \tag{4.18}$$

$$= k^2 m^2 \sum_{r=1}^{N_t} A_r \frac{h!i!}{h+i+2} \tag{4.19}$$

Note that, for the same reasons, also B is sparse matrix. It is worth noticing that matrices $\boldsymbol{A}$ and $\boldsymbol{B}$ are well known in the community of FEM , whereas the study of the $\boldsymbol{\Lambda_{bb}}$ matrix is an original content of this Thesis. We will discuss details of $\boldsymbol{\Lambda_{bb}}$ in the next sections.

Equation (4.16) can be rewritten as:

$$\begin{bmatrix} \boldsymbol{L}_{bb} & \boldsymbol{L}_{bi} \\ \boldsymbol{L}_{ib} & \boldsymbol{L}_{ii} \end{bmatrix} \begin{bmatrix} \boldsymbol{x}_b \\ \boldsymbol{x}_i \end{bmatrix} = \begin{bmatrix} \boldsymbol{f}_b \\ \boldsymbol{f}_i \end{bmatrix} \tag{4.20}$$

where the subscripts 'i' and 'b' refer to the internal and boundary nodes of the computational domain B_R, respectively and $\boldsymbol{L} = \boldsymbol{\Lambda} - \boldsymbol{A} + \boldsymbol{B}$ is the sum of DtN, stiffness and mass matrix. Due to non local nature of the DtN operator, $\boldsymbol{\Lambda_{bb}}$ is a $N_B \times N_B$ dense matrix (see Chapter 2 section 2.2.1), being N_B the number of degrees of freedom (DoFs) located on ∂B_R. In the typical cases of interest the N_B (boundary nodes) are much less than N_I (internal nodes). This mean that $\boldsymbol{\Lambda_{bb}}$ is a very small part compared to the left part of $\boldsymbol{L}$ matrix. This basically means that $\boldsymbol{L}$ is sparse. The equation (4.20) can be written in compact form as:

$$\boldsymbol{L}x = f \tag{4.21}$$

As stated, the initial problem is converted into the solution of a linear algebric system. Moreover we note that the sparsity of $\boldsymbol{L}$ is a great advantage from computation point of view, because specialized solver exist both for direct and iterative methods.

4.2.1 DtN integral

Here we compute $\boldsymbol{\Lambda}$.

On the boundary ∂B_R w_s, can be represented as:

$$w_s = \sum_{i \in N_B} x_i \varphi_i \tag{4.22}$$

being N_B a set of boundary nodes.The discretization of:

$$\int_{\partial B_R} \varphi(\Lambda_R w^s) dl = \int_{\partial B_R} \varphi_p(\Lambda_R \varphi_i) dl \tag{4.23}$$

in accord with (2.12) corresponds to:

$$
\begin{aligned}
&= \int_0^{2\pi} \varphi_p(R,\theta)\frac{k}{4\pi}\sum_{n=-\infty}^{\infty}\left[\frac{H_{n-1}^{(2)}(kR)-H_{n+1}^{(2)}(kR)}{H_n^{(2)}(kR)}\int_0^{2\pi}\varphi_i(R,\theta')e^{-\jmath n\theta'}d\theta'\right]e^{\jmath n\theta}Rd\theta \\
&= \frac{kR}{4\pi}\sum_{n=-\infty}^{\infty}\frac{H_{n-1}^{(2)}(kR)-H_{n+1}^{(2)}(kR)}{H_n^{(2)}(kR)}\int_0^{2\pi}\varphi_i(R,\theta')e^{-\jmath n\theta'}d\theta'\int_0^{2\pi}\varphi_p(R,\theta)e^{\jmath n\theta}d\theta \\
&= \pi kR\sum_{n=-\infty}^{\infty}\frac{H_{n-1}^{(2)}(kR)-H_{n+1}^{(2)}(kR)}{H_n^{(2)}(kR)}\Phi_{i,n}\Phi_{p,n}^{*}
\end{aligned}
\tag{4.24}
$$

where the symbol * means the complex conjugate, and

$$
\Phi_{i,n} = \frac{1}{2\pi}\int_0^{2\pi}\varphi_i(R,\theta')e^{-\jmath n\theta'}d\theta' \tag{4.25}
$$

Assuming a piecewise linear approximation for $\varphi_i|_{\partial B_R}$ we have:

$$
\Phi_{i,n} = \frac{1}{2\pi n^2}\left[\frac{e^{-\jmath n\theta_0^i}-e^{-\jmath n\theta_N^i}}{\theta_0^i-\theta_N^i}+\frac{e^{-\jmath n\theta_P^i}-e^{-\jmath n\theta_0^i}}{\theta_P^i-\theta_0^i}\right] \tag{4.26}
$$

where θ_0^i is the angle for node i and $\theta_P^i = \theta_0^{i-1}$ and $\theta_N^i = \theta_0^{i+1}$. We provide the details of (4.26) in Appendix C.

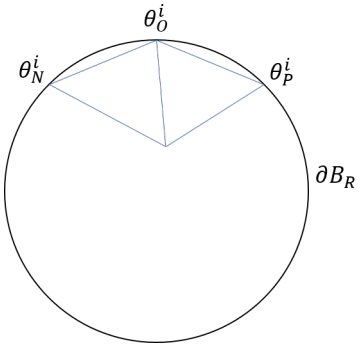

Figure 4.3: Polyhedric approximation of boundary

It is worth noting that the DtN matrix is symmetric.

$$
\int_{\partial B_R}\varphi_p(\Lambda_R\varphi_i)dl = \int_{\partial B_R}\varphi_i(\Lambda_R\varphi_p)dl \tag{4.27}
$$

4.3 Numerical model of differential formulation coupled the Internal and External DtN operator

Using similar steps of the previous section 4.2, the DtN integral is divided in two parts relative to the external and internal DtN, respectively. The linear system of the weak-form equations (2.20) for DoFs can be written as:

$$(\boldsymbol{\Lambda^I} + \boldsymbol{\Lambda^O} - \boldsymbol{A} + \boldsymbol{B})\boldsymbol{x} = \boldsymbol{f} \tag{4.28}$$

where

$$\Lambda^I_{h,i} = \int_{\partial B^I_R} \varphi_h(\Lambda^I_R \varphi_i) dl \tag{4.29}$$

$$\Lambda^O_{h,i} = \int_{\partial B^O_R} \varphi_h(\Lambda^O_R \varphi_i) dl \tag{4.30}$$

$$A_{h,i} = \int_{B_R} \nabla\varphi_h \cdot \nabla\varphi_i dS \tag{4.31}$$

$$B_{h,i} = k^2 \int_{B_R} m^2 \varphi_h \varphi_i dS \tag{4.32}$$

$$f_h = -k^2 \int_{B_R} (m^2 - 1)\varphi_h w^i dS \tag{4.33}$$

Notice that the boundary nodes include those arising from the internal and external DtN operators. By splitting the unknowns (DoFs) in boundary $\boldsymbol{x}_b$ and internal nodes $\boldsymbol{x}_i$ of the finite element mesh, the system (4.28) can be written as :

$$\begin{bmatrix} \boldsymbol{L}_{bb} & \boldsymbol{L}_{bi} \\ \boldsymbol{L}_{ib} & \boldsymbol{L}_{ii} \end{bmatrix} \begin{bmatrix} \boldsymbol{x}_b \\ \boldsymbol{x}_i \end{bmatrix} = \begin{bmatrix} \boldsymbol{f}_b \\ \boldsymbol{f}_i \end{bmatrix} \tag{4.34}$$

where the subscripts *'i'* and *'b'* refer to the internal and boundary nodes of the computational domain B_R, respectively. Again we found (4.21) where the $\boldsymbol{L} = \boldsymbol{\Lambda^I} + \boldsymbol{\Lambda^O} - \boldsymbol{A} + \boldsymbol{B}$ is a matrix composed by the internal and external DtN matrix, stiffness and mass matrix. Note that $\boldsymbol{\Lambda^O}$ and $\boldsymbol{\Lambda^I}$ are the DtN matrices that respectively involve the external and internal boundary nodes. These integrals give rise the dense matrices $N_{B^O} \times N_{B^O}$ and $N_{B^I} \times N_{B^I}$, being N_{B^O} and N_{B^I} the number of DoFs located on ∂B^O_R and ∂B^I_R.

4.3.1 Limits of Internal DtN

This section reports an analysis of the computational cost associated with the internal DtN. The aim is to evaluate the efficacy of the use of the internal DtN coupled with the external one, to solve the scattering problem from hollow objects.

The discretization of the domain is composed of equilateral triangles. If l is the side of a generic equilateral triangle, the area is:

$$A_T = \frac{l^2}{4}\sqrt{3} \tag{4.35}$$

The number of triangles in the internal domain in the case of standard FEM method without the internal DtN is:

$$N_T = \frac{\pi R_i^2}{\frac{l^2}{4}\sqrt{3}} = \frac{4\pi R_i^2}{\sqrt{3}l^2} \tag{4.36}$$

where R_i is the internal radius of ∂B_R^I.

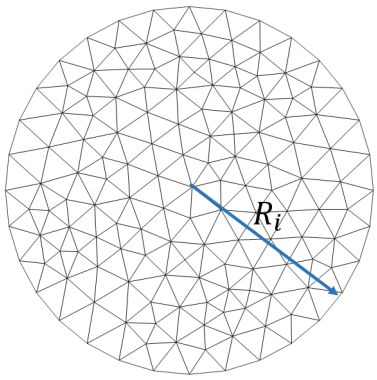

Figure 4.4: Geometry reference for evaluating the computational cost for the internal DtN

As shown in Figure 4.5, each triangle generates 3 nodes and each node is shared by six triangles and is surrounded by six adjacent nodes. Thus the number of internal nodes is given by ;

$$N_N = \frac{3N_T}{6} = \frac{N_T}{2} \tag{4.37}$$

The computational cost is related to the number of non-zero (nnz) elements of the matrix N_c . We note that each entry in the matrix rows is related to the number of adjacent

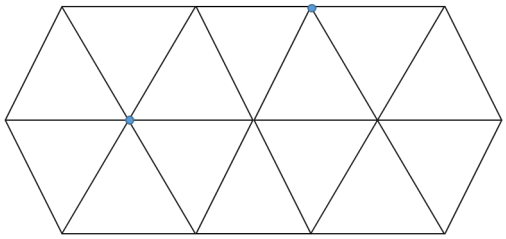

Figure 4.5: Triangular partition

nodes. Hence the number of the entries is twice (symmetry) the number of adjacent nodes plus the diagonal entries. For this reason the computational cost is given by:

$$N_{\text{C,FEM}} \;=\; 13N_N \;=\; 13\frac{N_T}{2} \;=\; \frac{13}{2}\frac{4\pi R_i^2}{\sqrt{3}l^2} \tag{4.38}$$

Instead, the computational cost associated with the use of the internal DtN is given by, as shown in the Figure 4.4:

$$N_{\text{C,DtNi}} = \left(\frac{2\pi R_i}{l}\right)^2 \tag{4.39}$$

The ratio between the costs is:

$$\frac{N_{\text{C,DtNi}}}{N_{\text{C,FEM}}} = \frac{\frac{4\pi^2 R_i^2}{l^2}}{\frac{13}{2}\frac{4\pi R_i^2}{\sqrt{3}l^2}} = \frac{2\sqrt{3}}{13}\pi \simeq 0.83 \tag{4.40}$$

It is evident from the result the use of Internal DtN, for hollow objects, is not efficient in term of the computational cost. To overcome this limit a sparsification of the DtN matrix is mandatory. The speedup of this matrix decreases the computational cost and makes the DtN effective for the interior problem, this sparsification is tried in section 4.4.

4.4 Sparsification of the DtN

Matrix $\mathbf{\Lambda}_{bb}$ can be properly sparsified through different techniques. We propose two approaches: one based on a factorization and an the other based on Fast Fourier Transform (FFT). The aim is to reduce the number of multiplications N_b^2 of the matrix-by-vector product $\mathbf{\Lambda}_{bb}\boldsymbol{x}_b$ keeping the same accuracy. In the following subsections we will show that the computational cost of the two proposed approaches is approximately the same.

4.4.1 Factorization

The first approach for sparsifying the DtN integral, is based on a factorization. The starting point is the discrete version of (4.12):

$$\int_{\partial B_R} \varphi_p(\Lambda_R \varphi_i) dl = \pi k R \sum_{n=-\infty}^{+\infty} \frac{H_{n-1}^{(2)}(kR) - H_{n+1}^{(2)}(kR)}{H_n^{(2)}(kR)} \Phi_{n,i} \Phi_{n,p}^* \tag{4.41}$$

where

$$\Phi_{n,i} = \frac{1}{2\pi} \int_0^{2\pi} \varphi_i(R,\theta) e^{-jn\theta'} d\theta'. \tag{4.42}$$

We can write integral (4.41) in matrix form as:

$$\boldsymbol{\Phi}^\dagger \boldsymbol{S} \boldsymbol{\Phi} \tag{4.43}$$

where the symbols * and † indicates the conjugate and conjugate transpose of the referred matrix, respectively.

Truncating the sum of (4.41) between $n = -N_A ..., 0, ... N_A$, and denoting the number of boundary nodes on ∂B_R as N_B, then $\boldsymbol{\Phi}$ is a $(2N_A+1) \times N_B$ matrix:

$$\begin{aligned} \boldsymbol{\Phi} &= \begin{bmatrix} \phi_{-N_A,1} & \cdots & \phi_{-N_A,N_B} \\ \vdots & \vdots & \vdots \\ \phi_{N_A,1} & \cdots & \phi_{N_A,N_B} \end{bmatrix} \\ &= \begin{bmatrix} \boldsymbol{\phi}_{n1}, & \cdots & \boldsymbol{\phi}_{nN_B} \end{bmatrix} \end{aligned} \tag{4.44}$$

while **S** is the $(2N_A+1) \times (2N_A+1)$ diagonal matrix

$$\boldsymbol{S} = \text{diag}(d_n) = \begin{bmatrix} d_{-N_A} & & & & \\ & \ddots & & & \\ & & d_0 & & \\ & & & \ddots & \\ & & & & d_{N_A} \end{bmatrix} \tag{4.45}$$

where

$$d_n = \pi k R \frac{H_{n-1}^{(2)}(kR) - H_{n+1}^{(2)}(kR)}{H_n^{(2)}(kR)}. \tag{4.46}$$

Thus, the integral (4.41) in matrix form becomes:

$$\boldsymbol{\Phi}^{\dagger}\boldsymbol{S}\boldsymbol{\Phi} = \begin{bmatrix} \boldsymbol{\phi}_{n1}^{\dagger} \\ \vdots \\ \boldsymbol{\phi}_{N_B n}^{\dagger} \end{bmatrix} \begin{bmatrix} d_{-N_A} & & & & \\ & \ddots & & & \\ & & d_0 & & \\ & & & \ddots & \\ & & & & d_{N_A} \end{bmatrix} \begin{bmatrix} \boldsymbol{\phi}_{n1}, & \dots & \boldsymbol{\phi}_{nN_B} \end{bmatrix}$$

$$= \boldsymbol{\Lambda_{b,b}} \tag{4.47}$$

where the $(N_B \times N_B)$ matrix $\boldsymbol{\Lambda_{b,b}}$ is the DtN matrix.

4.4.2 Computational cost for the factorization approach

Using the factorization form (4.47), we carry out the matrix by vector multiplications in 3 steps:

1. $y = \boldsymbol{\Phi} x$, number of multiplications $(2N_A + 1) \times (2N_B + 1)$
2. $z = \boldsymbol{S} x$, number of multiplications $(2N_A + 1)$
3. $y = \boldsymbol{\Phi}^{\dagger} z$, number of multiplications $(2N_A + 1) \times (2N_B + 1)$

Summing up the computational cost for computing $\boldsymbol{\Lambda_{bb}} x_b$ is reduced to:

$$N_{\text{C,fact}} = (2N_A + 1) \times (2N_B + 1) \tag{4.48}$$

where N_A is the maximum number of the harmonics. We define the gain for the computational cost as the ratio between the number of multiplications originally required and the number of multiplications with the factorization, i.e.,

$$G_{\text{fact}} = \frac{N_B^2}{(2N_A + 1) \times (2N_B + 1)} \tag{4.49}$$

If $N_A, N_B \gg 1$

$$G_{\text{fact}} = \frac{N_B^2}{4N_B N_A} = \frac{N_B}{4N_A}. \tag{4.50}$$

In the next chapter, during the validation of the method, we will prove numerically the decrease of computational cost.

4.4.3 FFT approach

Another approach to sparsify the DtN integral is based on the Fast Fourier Transform (FFT) [49]. Indeed, it can be observed that the representation of the field (2.10) on the boundary ∂B_R can been see as a Forier series:

$$w(R,\theta) = \sum_{n=-\infty}^{+\infty} a_n e^{jn\theta} \tag{4.51}$$

with coefficients

$$a_n = w_n H_n^{(2)}(kR) \tag{4.52}$$

and the radial derivative of (4.51) can be written as:

$$\begin{aligned} \partial_r w(R,\theta) &= \sum_{n=-\infty}^{+\infty} w_n \frac{dH_n^{(2)}}{dr}(kR) e^{jn\theta} \\ &= \sum_{n=-\infty}^{+\infty} a_n \frac{H_{n-1}^{(2)}(kR) - H_{n+1}^{(2)}(kR)}{2H_n^{(2)}(kR)} e^{jn\theta} \end{aligned} \tag{4.53}$$

In order to speedup the computation, the Fourier coefficients can be calculated with the help of the FFT on the boundary ∂B_R. It is worth noting that the mesh boundary values $\boldsymbol{x}_b$ are associated to nodes which are not equally spaced on ∂B_R, as shown in the Figure 4.6. For this reason it is necessary to use a linear interpolation from the boundary values to N_F equispaced samples with step $\theta = 2\pi/N_F$.

In the following we report the necessary steps involved to speedup the matrix-by-vector product $\boldsymbol{\Lambda}_{bb}\boldsymbol{x}_b$ using the FFT approach.

1. The values of field on equispaced sampling points N_F can be computed with a linear interpolation starting from the mesh boundary values:

$$p(\theta_i) = p_1 + \frac{(\theta_i - \alpha_1)}{\alpha_2 - \alpha_1}(p_2 - p_1) \qquad \alpha_1 \leq \theta_i \leq \alpha_2 \tag{4.54}$$

   where $p_1 = w(R,\alpha_1)$ and $p_2 = w(R,\alpha_2)$ are the values of the field in two consecutive nodes respectively, and α_1 and α_2 the values of the angle of p_1 and p_2. The number of multiplications is $N_F + N_B$.

2. The FFT returns coefficients a_n as follows:

$$w_n = \frac{a_n}{H_n^{(2)}(kR)}. \tag{4.55}$$

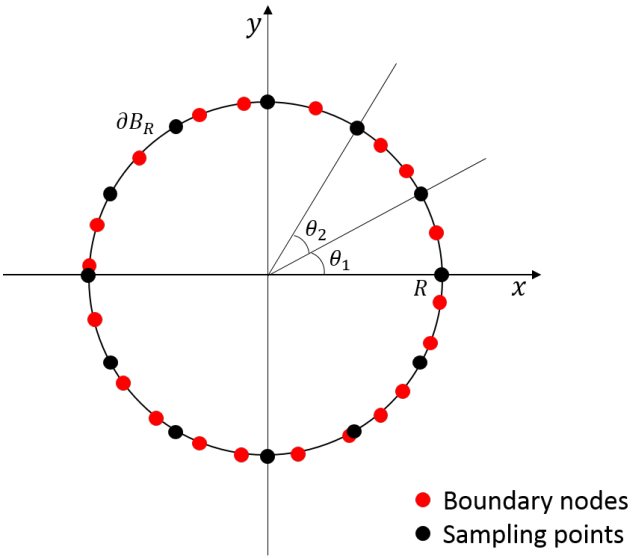

Figure 4.6: The N_B meshing nodes (boundary nodes) are non equispaced, the N_F FFT nodes (sampling nodes) are equispaced

Notice that the number of required multiplications of the FFT is $N_F \log_2(N_F)$.

3. From (4.53) it follows that the coefficients of the normal derivative of the field are given by:
$$b_n = \frac{a_n}{2} \frac{H^{(2)}_{n-1}(kR) - H^{(2)}_{n+1}(kR)}{H^2_n(kR)} \tag{4.56}$$
with computational cost equal to N_A+1.

4. The radial derivative by means of $\partial_r w(R,\theta)$ can be found as the inverse FFT of b_n:
$$\frac{\partial w(R,\theta_i)}{\partial n} = IFFT(b_n) \quad i = 1, ...N_F. \tag{4.57}$$
Notice that the number of required multiplications is the same of step 2.

5. Equation (4.57) returns the value of normal derivative of the field in on the regular sampling of the boundary ∂B_R. To get the values of the normal derivative of the boundary nodes of the mesh we need another linear interpolation. For this reason the computational cost is the same od step 1.

6. Finally, the Gauss-Legendre rule can be used to calculate the DtN integral (4.12) as internal scalar product. Which computational cost is proportional of N_B.

Finally, as observed the use of FFT is a change of the representation from nodal values of the field to harmonic series development.

4.4.4 Computational cost of the FFT approach

The computational cost for evaluating $\mathbf{\Lambda_{bb}} x_b$ with the FFT approach is

$$N_{\text{C,FFT}} = 2(N_F + N_B) + 2N_F \log_2(N_F) + (2N_A + 1) + N_B \tag{4.58}$$

where N_F is the number of sampling points.

The gain in terms of computational cost for the FFT is given by:

$$G_{\text{FFT}} = \frac{N_B^2}{2(N_F + N_B) + 2N_F \log_2(N_F) + (2N_A + 1) + N_B} \,. \tag{4.59}$$

In the next chapter, we will see that the number of harmonics N_A required for calculating the integral DtN $\mathbf{\Lambda_{bb}} x_b$ is low because is related to the slow variation of the field on the boundary. Finally, notice that for $N_B \gg 1$ we have G_{FFT} (4.50) still holds:

$$G_{\text{FFT}} = \frac{N_B}{3N_B + 2N_F \left(\log_2(N_F) + 1\right)} \tag{4.60}$$

Hence, as afore mentioned, the two different approaches (factorization and FFT) have the same asymptotic computation cost behavior. By comparing the two approaches for $N_A, N_B \gg 1$ it is possible to conclude that the computational cost gain of Factorization is slightly better than that of FFT.

Chapter 5

VALIDATION

In this chapter, the Dirichlet-to-Neumann (DtN) approach presented in this Thesis is applied to three different electromagnetic scattering problems. The proposed method is here compared to a classical approach, based on the implementation of the state-of-the-art absorbing boundary conditions, i.e. the Perfect Matching Layer.

The first problem is used to validate the proposed technique: indeed, the DtN numerical solution and that obtained from the PML approach are compared to an analytical reference solution. In the second case the scattering from a PVC tube contained in an annulus, bounded by two boundaries is presented. This case refers to a problem typically found in non-destructive testing applications. In the last case, a cable bundle is reported, in a typical configuration of interest of the electromagnetic compatibility (EMC) analysis. This validation proves the superiority of the DtN based approach with respect to PML both in terms of reduced number of multiplication for computing the matrix-by-vector product for a prescribed accuracy and in terms of better condition number of the relevant stiffness matrix.

5.1 Scattering from a penetrable cylinder

For the first case an infinitely long penetrable cylinder is considered. The scatterer is illuminated by a TM_z plane wave, with wave-vector **k** oriented along the x-axis, as shown in Figure 5.1. The incident field is thus given by:

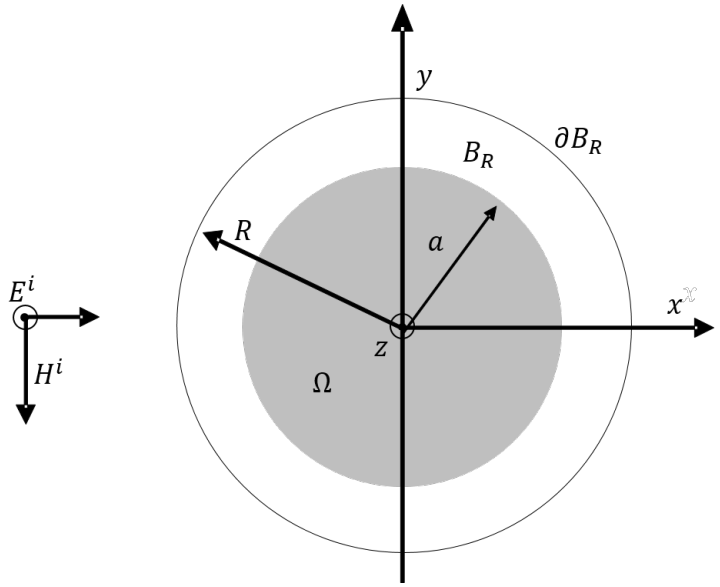

Figure 5.1: Case-study 1. Geometry of the problem: scattering from an infinitely long penetrable cylinder, illuminated by a TM_z plane wave.

$$E^i(r,\theta) = E_0 e^{-\jmath k r \cos(\theta)} \tag{5.1}$$

We assume a scatterer with a radius $a = 0.1\,\mathrm{m}$ and the DtN boundary with a radius $B_R = 0.12\,\mathrm{m}$, and $\epsilon_r = 4$. The scatterer is hit by a plane-wave of frequency $f = 300\,\mathrm{MHz}$ (wavelength $\lambda = 1\,\mathrm{m}$).

The spatial distribution of the magnitude of the scattered field normalized to the incident field is showed in Figure 5.2, calculated from the analytical solution provided in [50].

5.1.1 Numerical result: DtN versus PML

The DtN numerical solution is implemented by a FE numerical model using a standard triangular mesh and nodal shape functions of the first order. The linear system of equations arising from the Finite Element Model has been solved through the Biconiugate Gradient Stabilized (BICGSTAB) [51], [52] combined with Incomplete LU (ILU) preconditioner [53]- [54].

This solution is compared to a PML-based one obtained by using COMSOL Multiphysics®

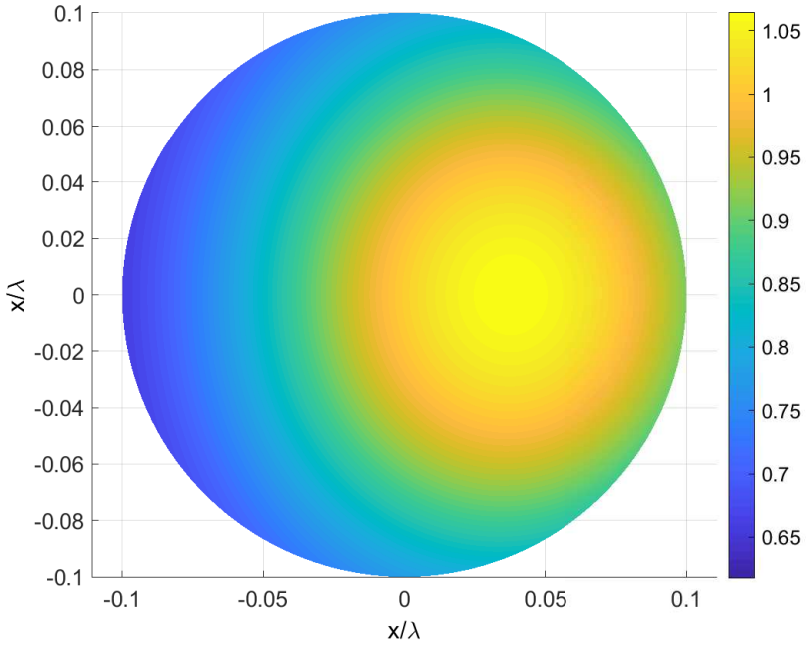

Figure 5.2: Scattering from a penetrable cylinder. Spatial distribution of the amplitude of the scattered field, normalized to the incident field.

[55]. This latter approach requires a layer of thickness δ to be added externally to the scatterer. In this case the propagating waves are attenuated as:

$$e^{\jmath(\omega t - kr) - \frac{k}{\omega}\int_{\sigma}^{\delta}\sigma(r')dr'} \tag{5.2}$$

being σ a positive function of the distance. The thickness δ and the distance of the layer have been optimized as shown in Figure 5.3, which shows the behavior of the. The relative error defined as

$$e_{\infty} = \frac{||E_n^s - E_a^s||_{\infty}}{||E_a^s||_{\infty}} \tag{5.3}$$

where the subscript *'n'* and *'a'* refer to the numerical and analytical solutions [50], respectively.

With the DtN approach the boundary of the computational domain can be placed close to the scatterer, as shown in Figure 5.4 where for different radius is reported the relative 2-norm error defined as

$$e_2 = \frac{||E_n^s - E_a^s||_2}{||E_a^s||_2}. \tag{5.4}$$

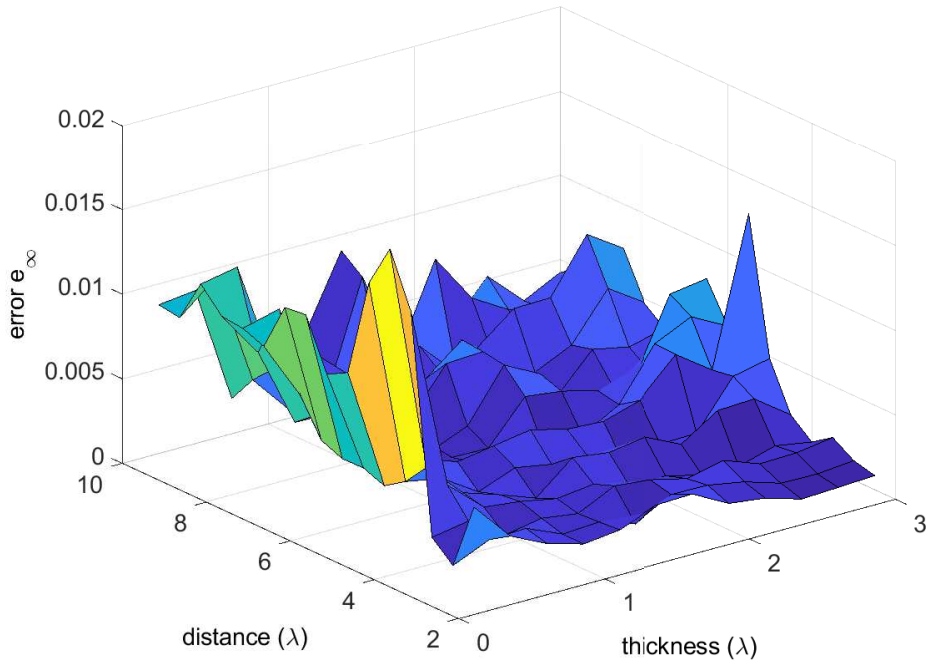

Figure 5.3: PML optimization. Relative (infinity norm) error versus the values of distance and thickness of the PML layer. The values are normalized to the wavelength.

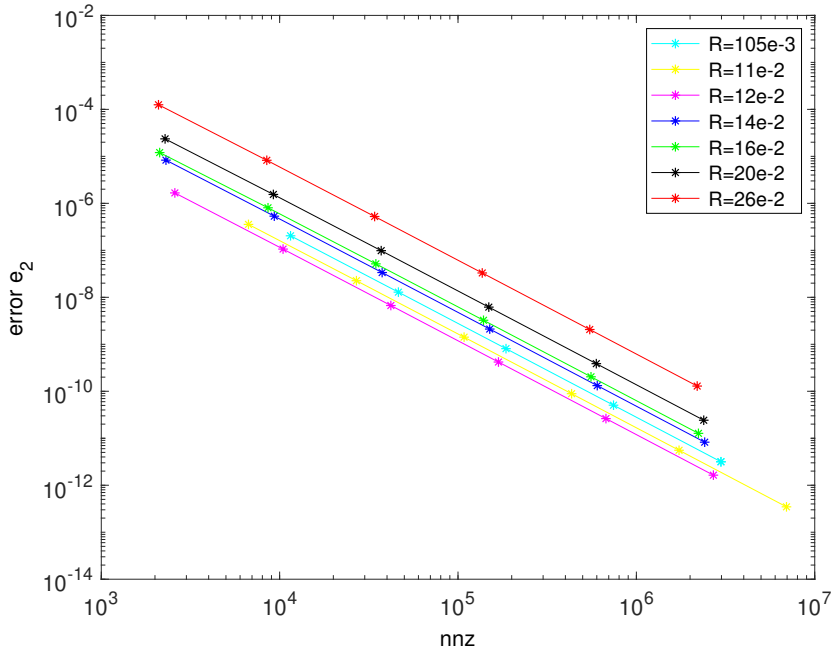

Figure 5.4: DtN boundary radius optimization. Relative 2-norm error versus as a function of the total number of non-zero elements, for different radius of the DtN boundary.

For both approaches, the optimized configurations are reported in Figures 5.5. It is evident that the DtN approach reduces the solution domain respect to the PML approach.

To prove the accuracy of the DtN approach, the plot of real and imaginary part of scattering field and their difference respect to the reference solution are reported in Figures 5.6-5.7.

Figures 5.8 and 5.9 compare the DTN and PML solutions accuracy with to both the relative 2-norm error. These errors are plotted as functions of the number of non-zero (nnz) elements of the stiffness matrix, that is a measure of the computational cost, as shown in Chap.4. It is evident that for a given computational cost, the accuracy gain in using the DtN is about two order of magnitude.

Another important quantity is the **condition number**, that affects the rate of convergence of iterative methods. The condition number of a matrix $\mathbf{A}$ is defined as:

$$k(\boldsymbol{A}) = ||\boldsymbol{A}||\,||\boldsymbol{A}^{-1}|| \tag{5.5}$$

where $||\boldsymbol{A}||$ is the 2-matrix norm defined as $||\boldsymbol{A}|| = (\max_i \lambda_i)^{\frac{1}{2}}$, λ_i being the eigenvalues

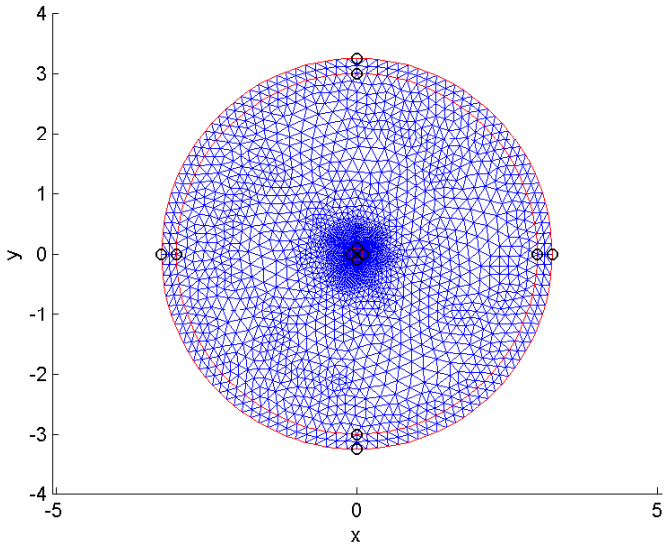

(a)

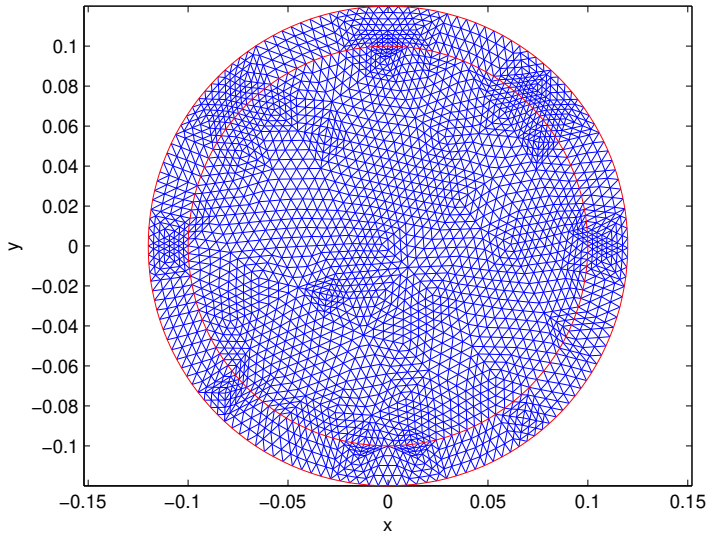

(b)

Figure 5.5: Scattering from a penetrable cylinder optimized positions for the boundary of DTN (a) and for the PML position and thickness (b).

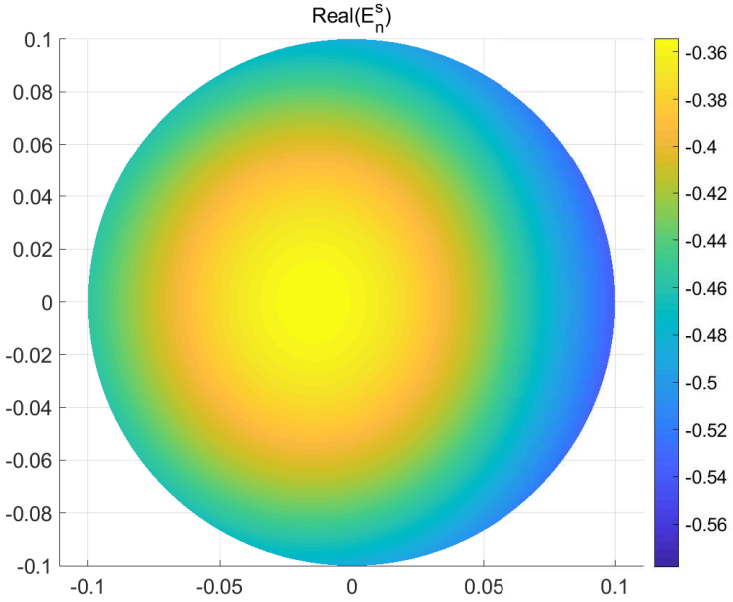

(a)

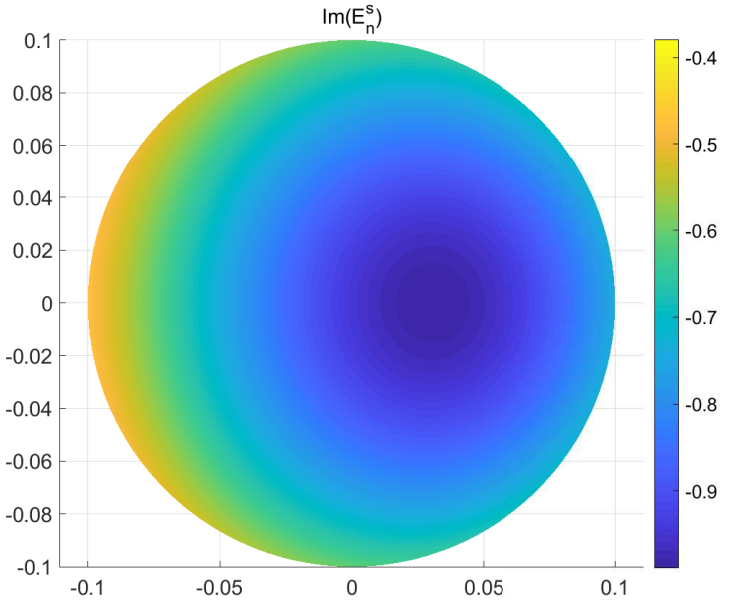

(b)

Figure 5.6: Scattering from a penetrable cylinder, obtained by means of the DTN approach. (a)-(b) Spatial distribution of the real and imaginary part of the scattered field, respectively.

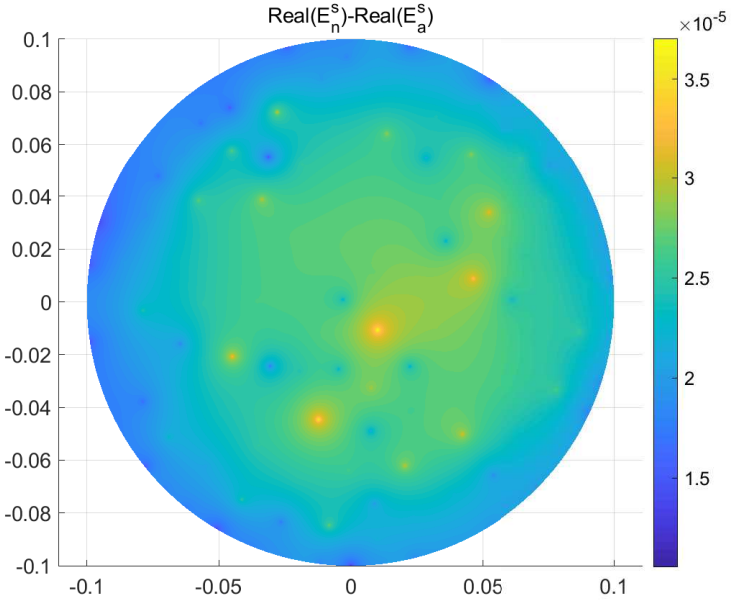

(a)

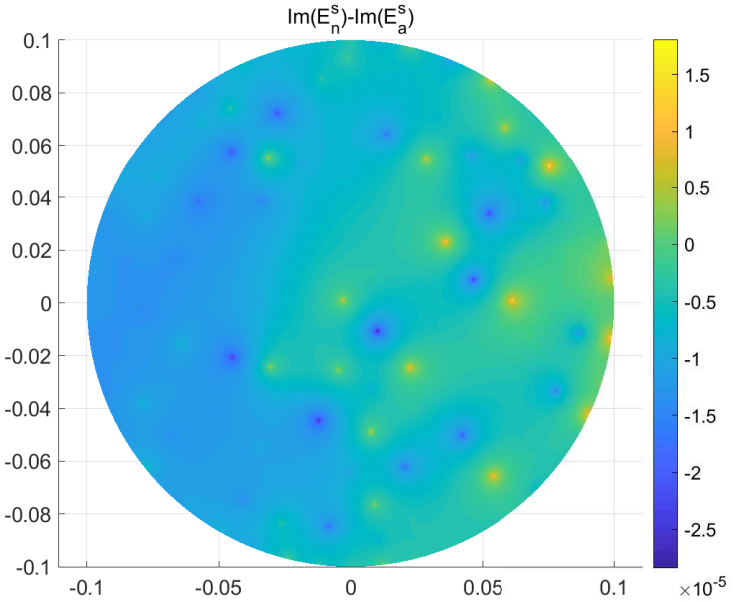

(b)

Figure 5.7: Scattering from a penetrable cylinder, obtained by means of the DTN approach. (a)-(b) Spatial distribution real and imaginary parts of the difference between numerical and reference solution.

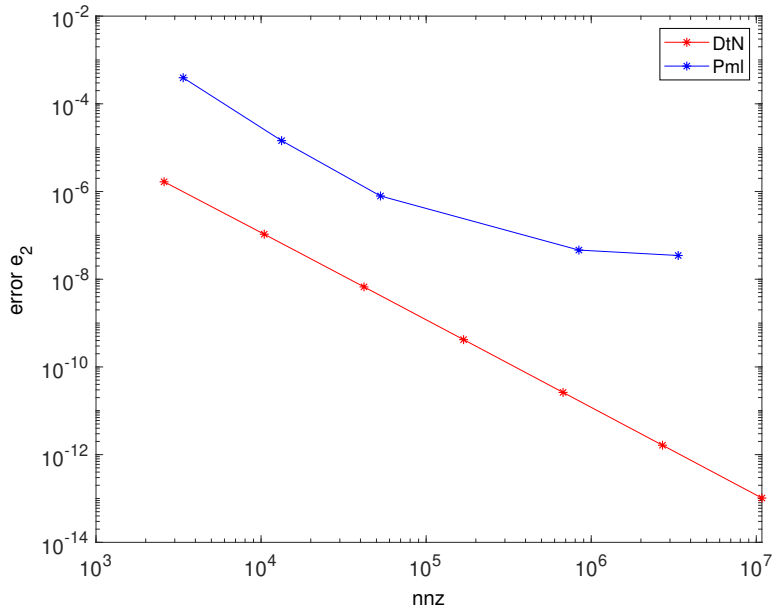

Figure 5.8: Relative 2-error as a function of the total number of non-zero elements, for DtN and PML approaches.

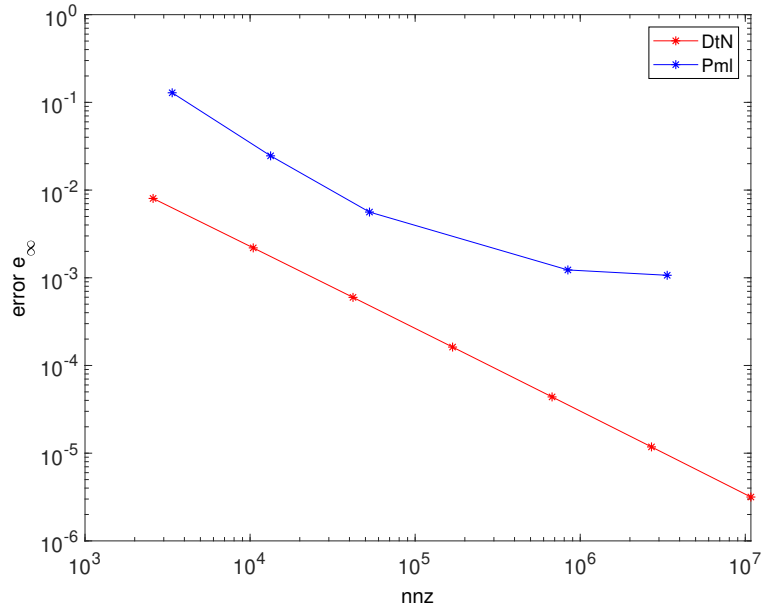

Figure 5.9: Relative infinity error as a function of the total number of non-zero elements, for DtN and PML approaches.

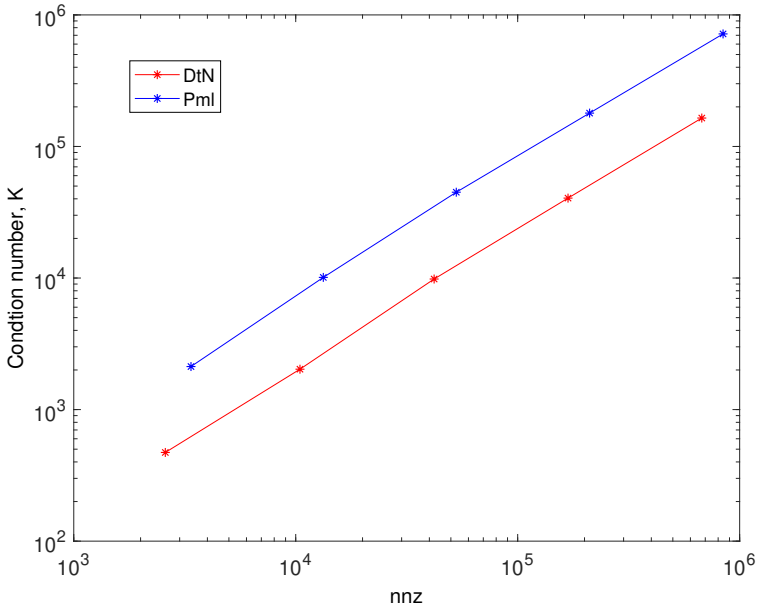

Figure 5.10: Relative infinity error as a function of the total number of non-zero elements, for DtN and PML approaches.

of $\boldsymbol{A}^H\boldsymbol{A}$. A problem with a low condition number is said to be well-conditioned, while a problem with a high condition number is said to be ill-conditioned. In Figure 5.10 it is reported the condition number k versus the total number of non-zero elements of the stiffness matrix. The DtN scheme provides a lower condition number, hence outperforming the PML one also in this sense.

5.1.2 Speed up of DtN matrix

As detailed in Chapter 4, the computational cost to solve the linear system, starting from the numerical model (4.20) is given by the number of non zero elements of the stiffness matrix $\boldsymbol{L}$ and by N_B^2 being N_B the number of the DoFs located on the DtN boundary (see Chap.4).

In Chapter 4 two different approaches for reducing the computational cost are proposed: the factorization and the FFT. As regards to the first approach, the reduction of the cost is related to the number of harmonics needed for truncating the sum of the discrete form of the DtN integral (4.41). It can been that the number of harmonics required for

calculating the DtN matrix without losing the accuracy is very small. Indeed, Figure 5.11 shows the relative 2-norm error calculated with respect to the reference solution versus the N_a number of harmonics for two different meshes. It is evident that for a small value of N_a the accuracy of the solution does not change, therefore the minimum value that can be chosen to calculate the DtN matrix with the factorization and/or the FFT is $N_a = 5$. As stated in Chapter 4, the computational gain of both approaches to speed up the DtN matrix are:

$$G_{\text{fact}} = \frac{N_B^2}{(2N_A + 1) \times (2N_B + 1)} \tag{5.6a}$$

$$G_{\text{FFT}} = \frac{N_B^2}{2(N_F + N_B) + 2N_F \log_2 N_F + (2N_A + 1)} \tag{5.6b}$$

Figure 5.12 shows the gain for the FFT 5.6b and the Factorization 5.6a approach versus the relative error, i.e., versus the accuracy of numerical model. It is evident that for high accuracy we have a gain in terms of computational cost with the FFT approach. For example, to get an accuracy of 10^{-10} we have a gain equal to 2.

Finally, the relative 2-error versus the number of multiplications is reported in Figure 5.13. It is easy to observe the advantage of using the FFT and Factorization approach.

5.2 Scattering from a PVC tube

The second problem is referred to an application of non-destructive testing, and specifically on the analysis of the degradation of a PVC tube, based on its electromagnetic response. The PVC tubes are used in many fields, for example in thermal power plant, compressed air systems, water system and so on.

Degradation of PVC can be a consequence of the environmental stresses, the chemical and thermal degradation, the mechanical force and UV, gamma and other forms of radiation. For this reason, the nondestructive methods are important for deterioration diagnosis, which involve the study of the electromagnetic scattering to obtain information on the object under examination.

Specifically, the second case presented in this section is referred to the scattering by a PVC tube infinitely long in the z-direction (Figure 5.14). The object is penetrable by the

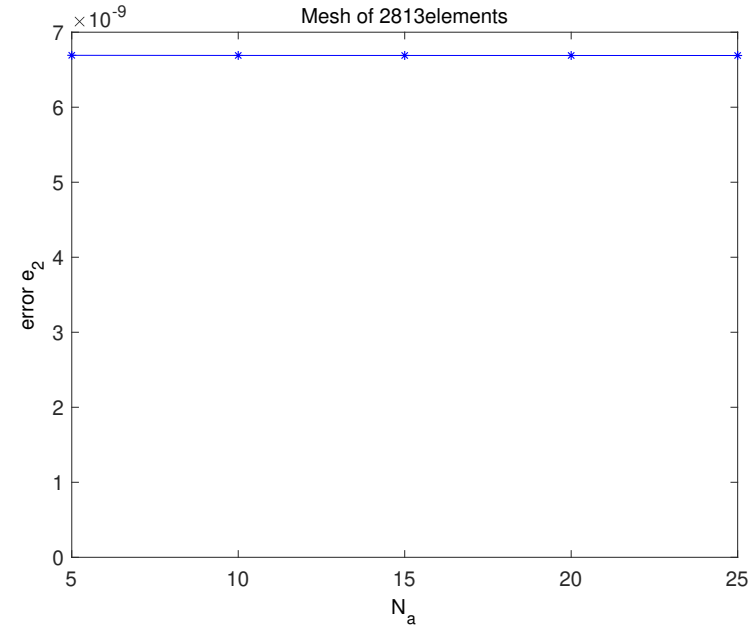

(a)

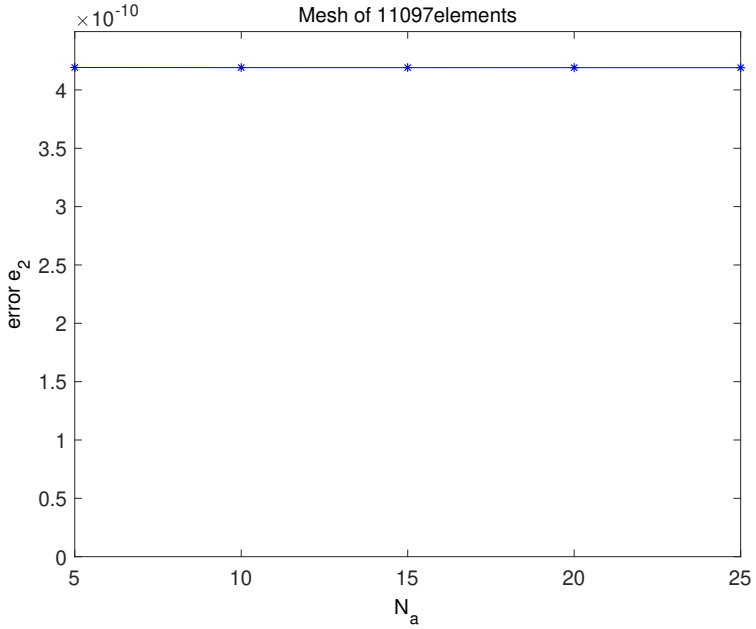

Figure 5.11: Relative 2-error as a function of the number of harmonics Na for a mesh of (a) 2813 elements and (b) 11097 elements. .

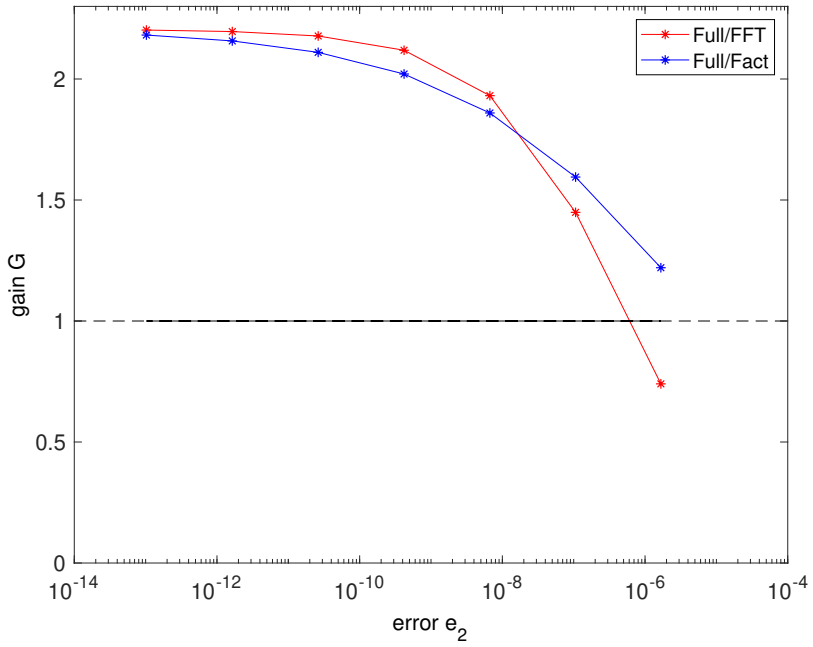

Figure 5.12: Gain versus the relative error for both the approaches for acceleration of DtN matrix: FFT and Factorization

electromagnetic field, being a dielectric of relative permittivity $\epsilon_r = 3$. Its dimensions are $R^i = 0.13\,\mathrm{m}$ and $R^O = 0.2\,\mathrm{m}$ for the internal and external boundary respectively.

We consider a PVC scatterer with an internal and external radius $0.19\,\mathrm{m}$ and $0.2\,\mathrm{m}$ respectively, hit by a plane-wave propagating along x, with a frequency $f = 300\,\mathrm{MHz}$ (wavelength $\lambda = 1\,\mathrm{m}$).

The scattered electric field (z-component) is mapped in Figure 5.15, normalized to that of the incident field. This result has been obtained by means of [50] and will be taken as the reference solution hereafter.

5.2.1 Numerical results: DtN versus PML

The numerical solution of the DtN-based formulation is obtained with a FE numerical model using a standard triangular mesh and nodal shape functions of the first order. Two numerical solutions are here evaluated based on DtN formulation, one referred at only use one DtN imposed on the external close boundary (2.6) and one that also involves the use

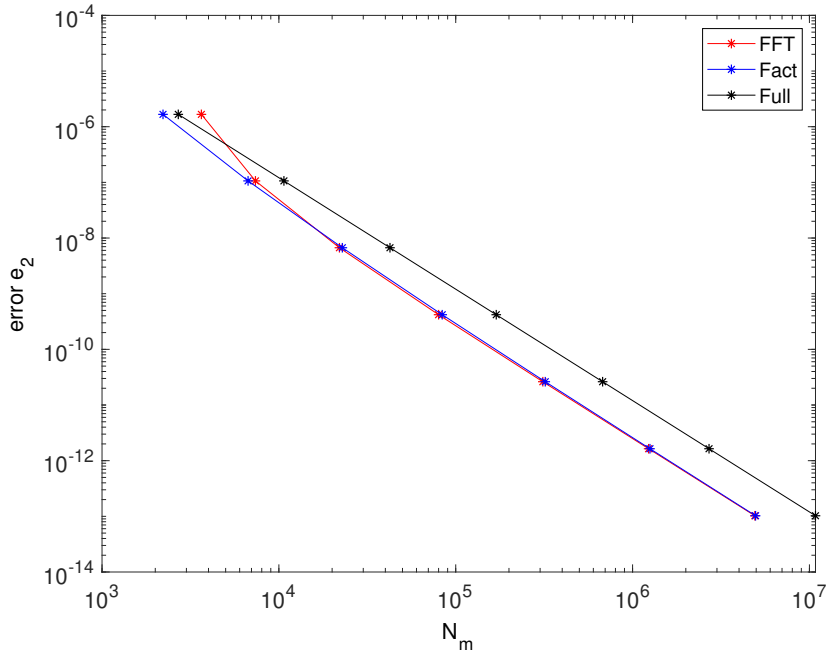

Figure 5.13: Relative error versus number of multiplications for the original, FFT or Factorization approach.

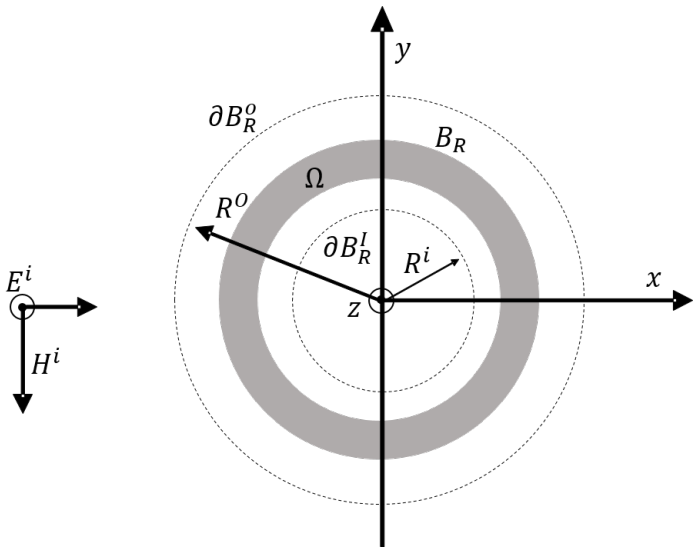

Figure 5.14: Case-study 2. Geometry and references for evaluating the scattering from an infinitely-long PVC tube, illuminated by a TMz plane wave.

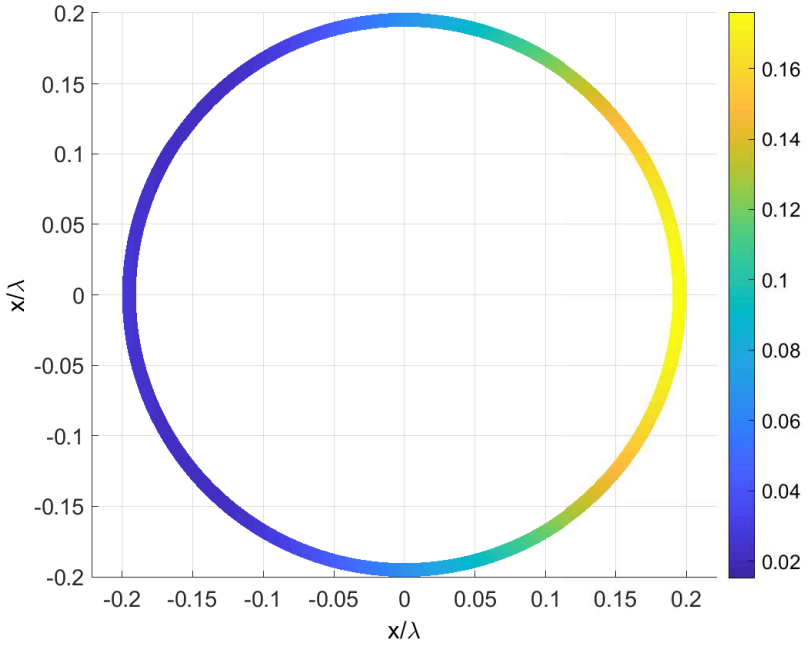

Figure 5.15: Scattering from a PVC tube. Spatial distribution of the amplitude of the scattered field, normalized to the incident field.

of internal DtN (2.20).

Figures 5.16-5.17 shows the plot of real and imaginary part of the scattered field obtained by using the DtN, along with their difference respect to the reference solution.

The errors of the two DTN numerical solution and the PML one are reported in Figure 5.18 showing the accuracy gain of the DtN approaches for a given computational cost. As already mentioned in Chapter 4 the sparsification of the DtN is mandatory to benefit from the internal DtN in terms of computational gain. Indeed, this figure clearly shows that tue use of internal DtN without sparsification does not provide a significant gain. Figure 5.19 shows the behavior of the infinite-error, which exhibit a similar behavior (in this case the use of the internal DtN does not provided any improvement).

In order to better estimate the gain in terms of computational cost, besides the number of nonzero elements *nnz* it is of interest to compare the condition number K of the resulting stiffness matrix associated with the two numerical models.

In Figure 5.20 it is reported the condition number K versus the number of no zero

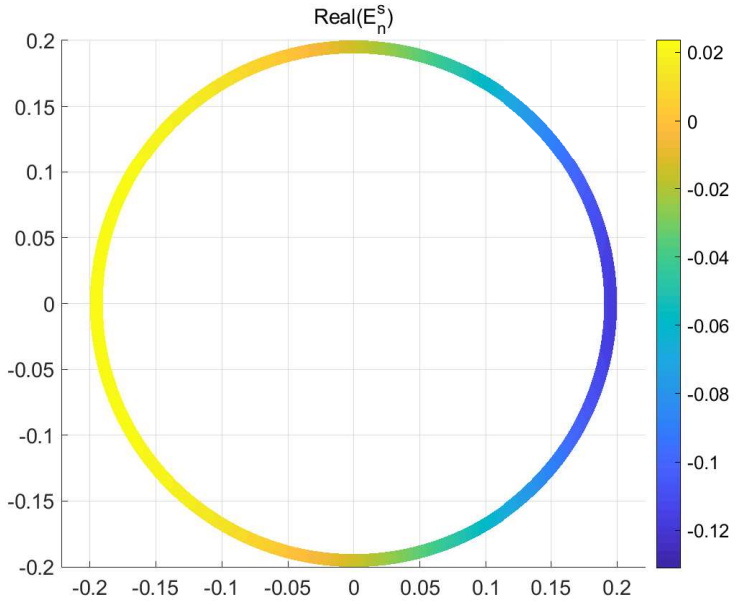

(a)

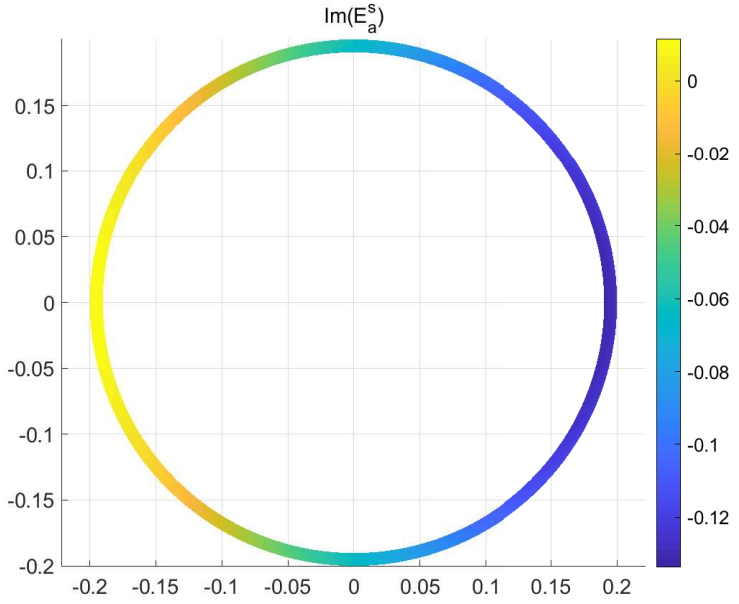

(b)

Figure 5.16: Scattering from a penetrable PVC tube. (a)-(b) Spatial distribution of the real and imaginary part of the scattered field, respectively.

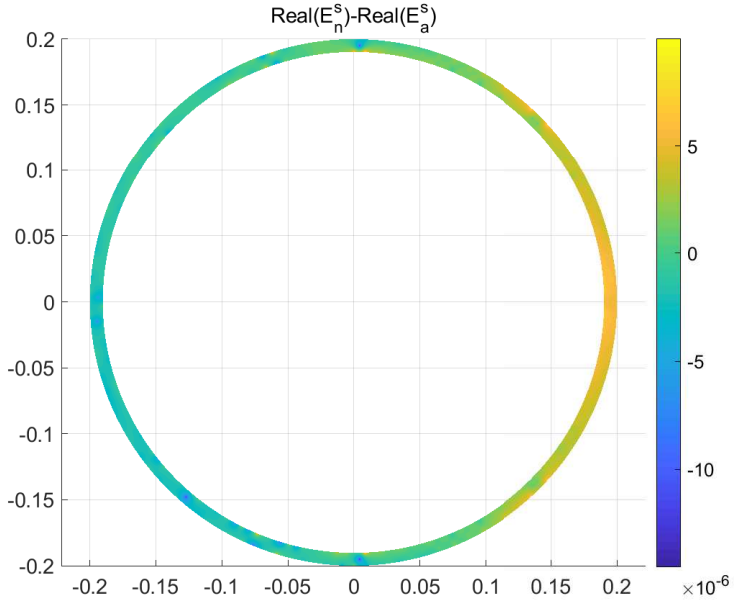

(a)

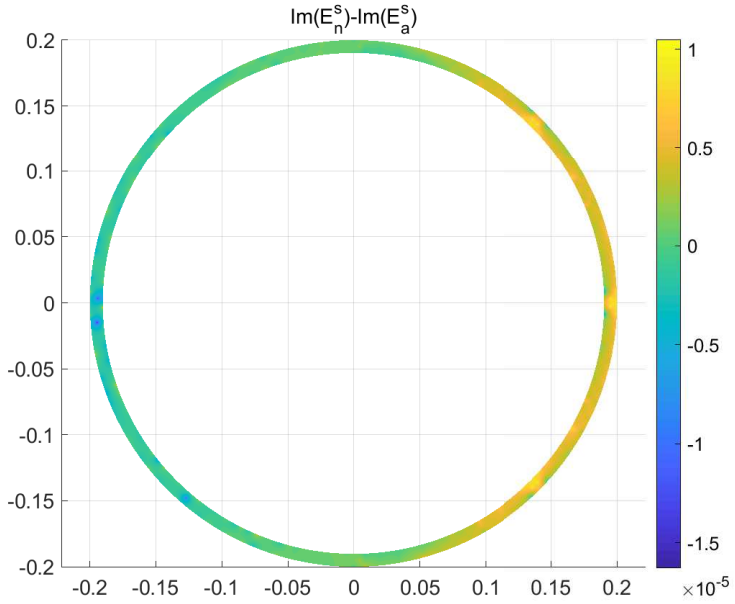

(b)

Figure 5.17: Scattering from a penetrable PVC tube. (a)-(b) Spatial distribution of the difference between the real and imaginary part of the scattered field and the reference solution in Fig. 5.15, respectively.

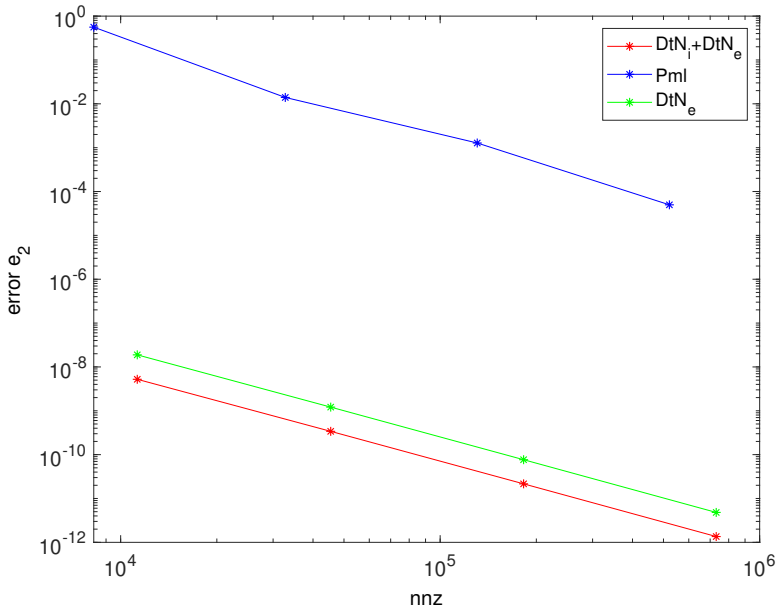

Figure 5.18: Relative 2-error as a function of the total number of non-zero elements, for PML approaches (in blue) external (in green) and external plus internal DtN (in red).

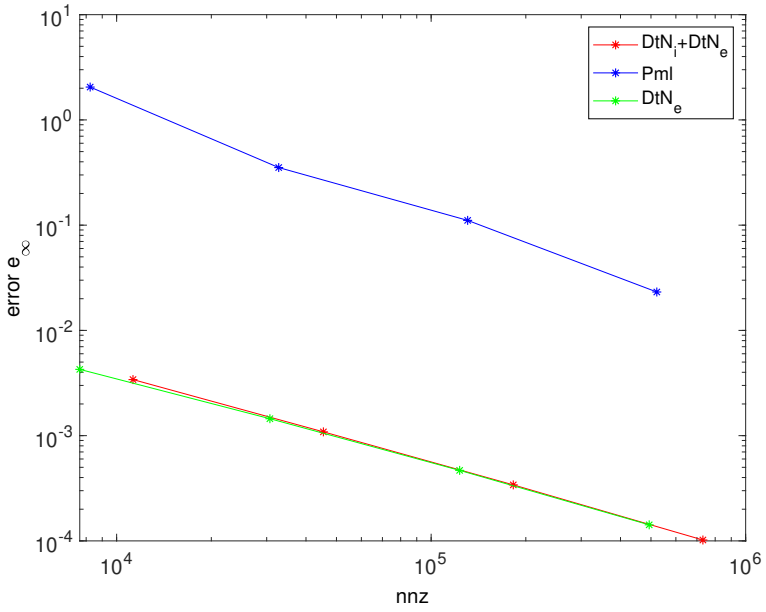

Figure 5.19: Relative infinity-error as a function of the total number of non-zero elements, for PML approaches (in blue) external (in green) and external plus internal DtN (in red)

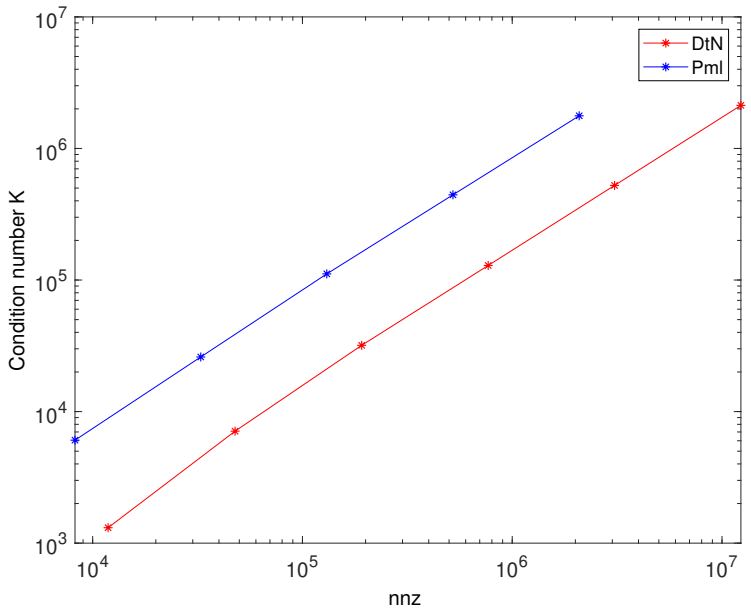

Figure 5.20: Condition number of the stiffness matrices associated to the two numerical solutions, versus the number of nonzero elements.

element of the stiffness matrix.

5.2.2 Speed up of DtN matrix

As shown in Chapter 4, the computational cost to solve the linear system, starting from the numerical model (4.34) is given by the number of no zero elements of stiffness matrix $\boldsymbol{L}$ plus N_{BO}^2 and N_{BI}^2 of N_{BO} and N_{BI} the Dof associated to the external and internal DtN boundaries, respectively. The computational cost for the two approaches Factorization and FFT for the case of PVC tube is given by:

$$\begin{aligned} N_{\text{C,fact}} &= [(2N_A+1)\times(2N_B+1)] + [(2N_A+1)\times(2N_{Bi}+1)] \\ &= (2N_A+1)\times[(2N_B+1)+(2N_{Bi}+1)] \end{aligned} \tag{5.7}$$

$$\begin{aligned} N_{\text{C,FFT}} &= [2(N_F+N_B) + 2N_F\log_2 N_F + (2N_A+1)] \\ &\quad + [2(N_F+N_{Bi}) + 2N_F\log_2 N_F + (2N_A+1)] \\ &= 2(2N_A+1) + 4N_F + 4N_F\log_2 N_F + 2(N_B+N_{Bi}) \end{aligned} \tag{5.8}$$

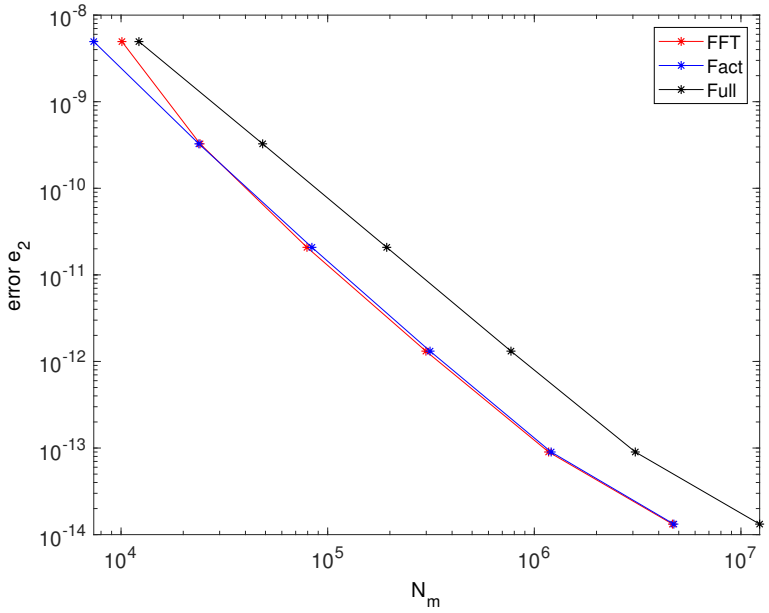

Figure 5.21: Relative error versus number of multiplications for the the original DtN numerical solution, and for those obtained by using, FFT or Factorization approach.

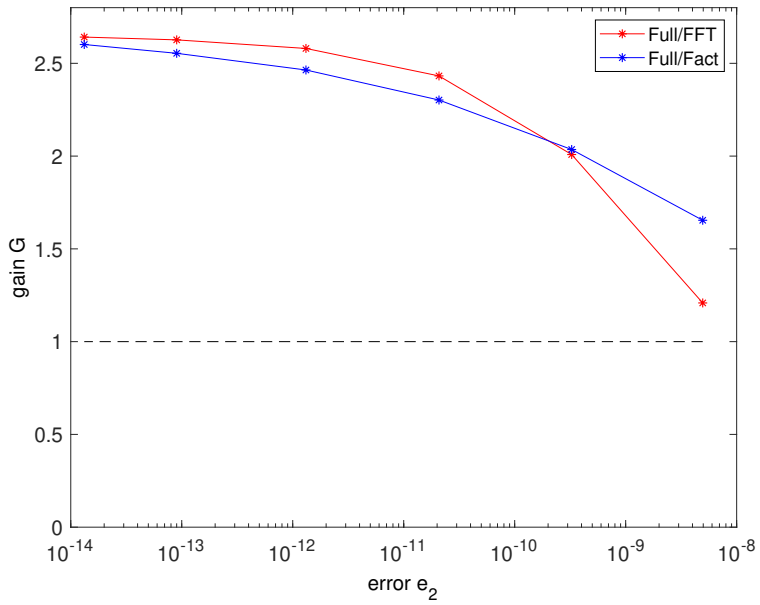

Figure 5.22: Gain versus the relative error for the both approaches for acceleration of DtN matrix: FFT and Factorization

In Figure 5.21 is reported the relative 2-norm error versus the number of multiplications to solve the numerical model (4.34). Here N_m is given by the number of non-zero elements of stiffness matrix $\boldsymbol{L}$ plus Nc_{fact} or Nc_{fft} for factorization or FFT approach respectively. The gain in term of computational cost with to the original approach versus the relative 2-norm error is reported in Figure 5.22.

5.3 Scattering from a cable bundle

As a final example of application of the DtN approach, we study here the scattering from a bundle of cable. This problem is of great interest for instance in the Electromagnetic Compatibility (EMC) analysis of automotive and/or aerospace applications. Specifically, the EMC/EMI issues with cable harnesses have become a major challenge due to the proliferation of electrical systems in vehicles, aircraft, ships, and buildings, which require the use of several kilometers of cables, bundled in harnesses. When the above systems are illuminated by an external field, it is essential to provide an accurate and efficient evaluation of the near-field distribution in proximity of scattering objects [56]-[57]. These results have been presented in the papers [58], [59], [60].

5.3.1 Scattering from a Cable Bundle in Air

As Case-Study 1, we refer to the geometry shown in Figure 5.23, where three conducting wires are bundled in an unshielded cable, surrounded by air ($\epsilon_r = 1$). The frequency is again assumed to be equal to $3\,\mathrm{GHz}$, with the wire radius $a = \lambda/6$, and the cable radius $b = \lambda$. The three wires are reciprocally rotated by 120° and their centers are placed at a distance equal to $c = \lambda/2$ from the cable center.

The DtN solution is calculated by choosing a circular boundary of radius $R = 1.2\lambda$. For this case, no analytical solution is available, and thus the reference solution is assumed to be that associated to the numerical solution provided by commercial code COMSOL Multiphysics® with PML approach, stabilized to an accuracy below 10^{-4}. For this example, computing the reference solution requires about 1.1×10^6 mesh elements. The obtained distribution of the amplitude of the scattered field is plotted in Figure 5.24.

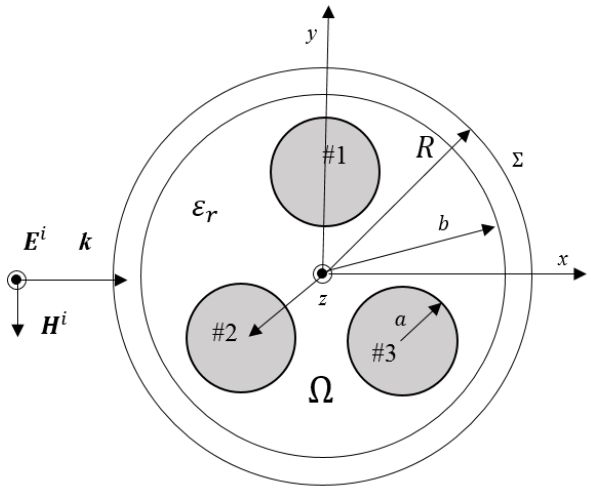

Figure 5.23: Case-study 1 (cable bundle in air). Geometry and references for evaluating the scattering from the cable bundle, illuminated by a TMz plane wave.

The evaluation of the maximum scattered field is important in EMC analysis, since it could provide the worst-case estimation of unwanted radiated emission and/or crosstalk noise between the conductors in the cable. Therefore, in the following case study we estimate the maximum value of the scattered field in the near-field region, namely inside the circle of radius $R = 1.2\lambda$. According to the solution in Figure 5.25, the maximum value of the scattered field, normalized to the amplitude of the incident wave, is equal to $\left|E^S\right| / E_0 = 1.604$.

From the plotted results, it is clear that the DtN solution converges to the reference value much faster than the PML one. In Figure 5.26, the condition number k defined as in Equation (5.5) is reported, highlighting a similar behavior compared to the other two scattering problems analyzed in this Chapter.

5.3.2 Scattering from a Cable Bundle in a Dielectric Coating

A Case-study 2 for the considered scattering problem is here analyzed, which has the same geometry as Case-study 1, but assuming the wires surrounded by a dielectric of relative permittivity are equal to $\varepsilon_r = 4$. The spatial distribution of the scattered field is now given in Figure 5.28, giving a maximum value of the scattered field, normalized to

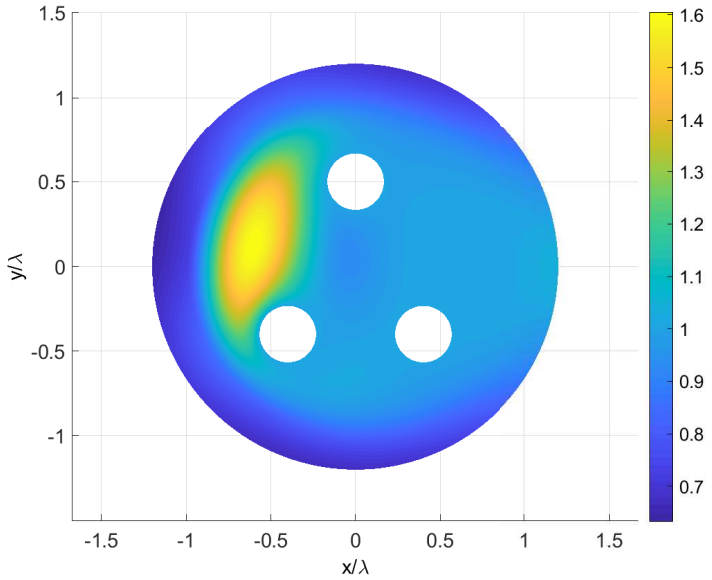

Figure 5.24: Case-study 1: distribution of the amplitude of the scattered field, normalized to that of the incident field. The axes x and y are normalized to the wavelength value.

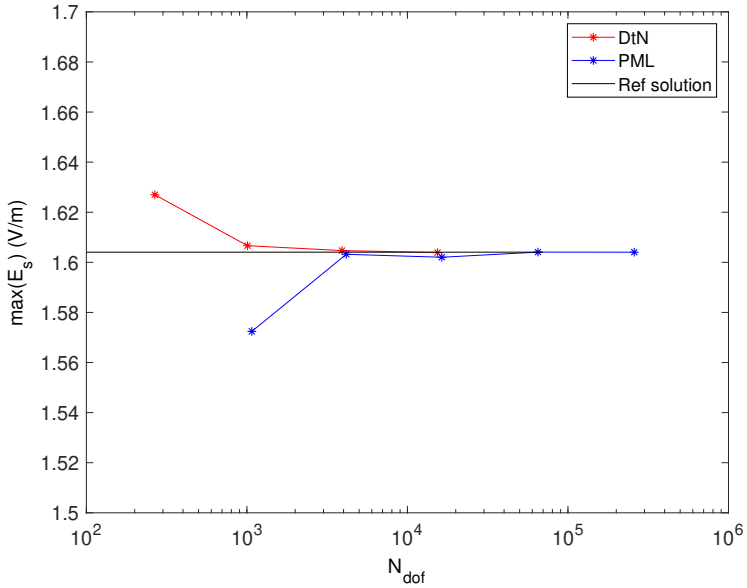

Figure 5.25: Maximum value of the scattered field, normalized to amplitude of the incident field, versus the number of mesh nodes: The DtN and PML solutions are compared to the reference one

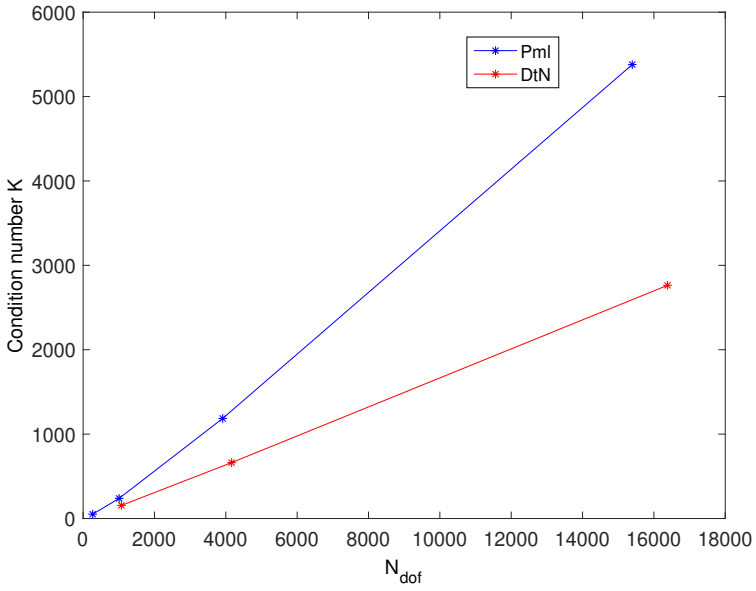

Figure 5.26: (Cable bundle with dielectric). Condition number of the stiffness matrices associated to the two numerical solutions versus the number of mesh nodes

	DtN	PML
w/o dielectric	511	2638
w dielectric	11573	59534

Table 5.1: Required number of mesh nodes (DoF) for 1% accuracy with and without the dielectric

the amplitude of the incident wave, equal to $\left|E^S\right|/E_0 = 3.3505$. The reference solution is again obtained by using COMSOL Multiphysics® with an accuracy below 10^{-4}.

In this example, the computation of the reference solution requires about $16,5 \times 10^6$ mesh elements. In Figure 5.28, we compare the DtN and PML numerical solution for increasing value of N_{dof}, of the mesh nodes: Once again, the DtN solution converges to the reference value much faster than the PML one. In Figure 5.29, the condition number k is reported, highlighting a similar behavior compared to other cases.

Finally, the required values of number of mesh nodes (DoF) for getting an accuracy of 1% is reported in Table 5.1 The computational gain in using the DtN is about a factor 5.

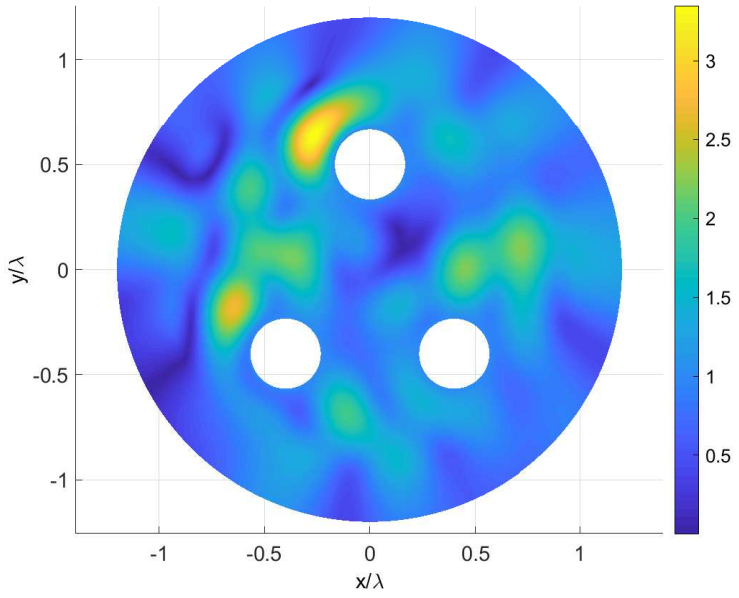

Figure 5.27: Distribution of the amplitude of the scattered field, normalized to that of the incident field. The axes x and y are normalized to the wavelength value

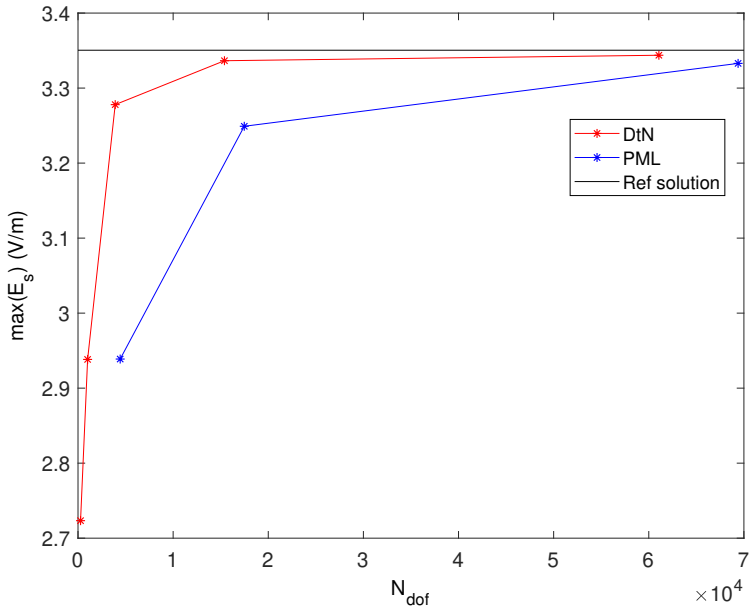

Figure 5.28: Maximum value of the scattered field, normalized to amplitude of the incident field, versus the number of mesh nodes: The DtN and PML solutions are compared to the reference one

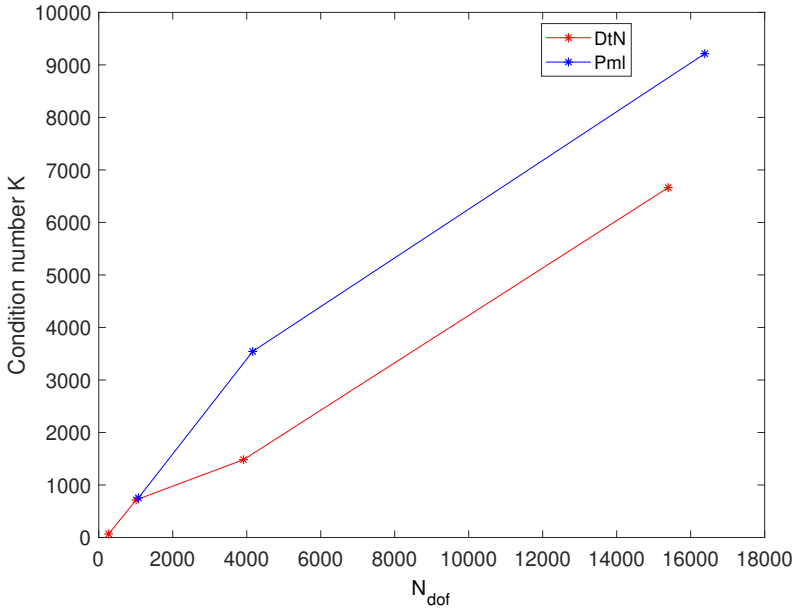

Figure 5.29: (Cable bundle with dielectric). Condition number of the stiffness matrices associated to the two numerical solutions versus the number of mesh nodes

Chapter 6

CONCLUSIONS

In this Thesis, the Dirichlet-to-Neumann operator has been used to develop a fast and accurate numerical model for computing the scattering of electromagnetic waves from a material body. Specifically, the DtN operator has been used to impose an exact boundary condition on the boundary of the computational domain. The underlying formulation is a differential one.

Since the boundary conditions imposed by means of the DtN operator are exact, the computational domain can be truncated rather close to the scatterer, thus reducing the computational cost. The performances of the proposed method have been compared to those of a state-of-the-art PML method. The comparison shows the superiority of the DtN based approach on the PML one. Performances have been compared with reference to two canonical geometries (a cylinder and a tube) and a practical configuration (bundle cables).

The original contributions of this Thesis are multiple. The first one is the introduction of the sparsification of the discrete representation of the DtN operator by means of two approaches [58], [59], [60]: an analytical factorization of the DtN matrix and the computation of the (DtN) matrix-by-vector product through FFT (Chapter 4). Both methods rely on the low rank property of the DtN matrix. The second contribution is the introduction of the DtN operator for the internal problem (Chapter 2). This operator is useful for treating problems where materials have cavities, as in the case of a tube (Chapter 4). The third contribution is the extension of the theory from the 2D scalar Helmholtz to the scattering

of electromagnetic wave from a z-invariant material, under either the TMz or TEz illuminations. The material can be isotropic or anisotropic, homogeneous or inhomogeneous, with either dielectric and/or magnetic properties. An exhaustive numerical campaign has been developed in Chapter 5.

Appendix A

HELMHOLTZ'S EQUATION IN CYLINDIRCAL COORDINATES

In cylindrical coordinates the Laplacian is given by (2D case)

$$\nabla^2 w = \frac{1}{r}\frac{\partial w}{\partial r} + \frac{\partial^2 w}{\partial r^2} + \frac{1}{r^2}\frac{\partial^2 w}{\partial \theta^2} \tag{A.1}$$

and the Helmholtz differential equation becomes:

$$\frac{1}{r}\frac{\partial w}{\partial r} + \frac{\partial^2 w}{\partial r^2} + \frac{1}{r^2}\frac{\partial^2 w}{\partial \theta^2} + k^2 w = 0\,. \tag{A.2}$$

Let perform a separation of variables in (A.2) [61] as follows:

$$w(r,\theta) = R(r)F(\theta) \tag{A.3}$$

where $F(\theta)$ is periodic of 2π.

Combining equation (A.2) to (A.3) gives

$$\frac{r^2}{R}\left(\frac{d^2 R}{dr^2} + \frac{1}{r}\frac{dR}{dr} + k^2 R\right) = -\frac{1}{F}\frac{\partial^2 F}{\partial \theta^2} \tag{A.4}$$

so that the equation takes a separated form.

Since the solution must be periodic in theta θ from the definition of the circular cylindrical coordinate system, the solution to the second part of (A.4) must have a negative separation constant

$$\frac{1}{F}\frac{d^2 F}{d^2 \theta} = -m\,. \tag{A.5}$$

Equation (A.4) becomes:

$$r^2\frac{d^2R}{dr^2}+r\frac{dR}{dr}+(k^2r^2-m)R=0 \tag{A.6}$$

whose solution, if $m>0$, is

$$F(\theta)=a_ne^{\jmath\sqrt{m}\theta}+b_ne^{-\jmath\sqrt{m}\theta} \tag{A.7}$$

where the exponentials are both periodic with period $T=2\pi/\sqrt{m}$. To guarantee the condition $m>0$, let assume

$$m=n^2 \qquad \text{with } n\in\mathbb{N} \tag{A.8}$$

so that the solution (A.7) becomes:

$$F(\theta)=a_ne^{\jmath n\theta}+b_ne^{-\jmath n\theta}\,. \tag{A.9}$$

According to (A.8), equation (A.6) can be rewritten as:

$$r^2\frac{d^2R}{dr^2}+r\frac{dR}{dr}+(k^2r^2-n^2)R=0 \tag{A.10}$$

and then

$$\frac{d^2R}{dr^2}+\frac{1}{r}\frac{dR}{dr}-\left(k^2-\frac{n^2}{r^2}\right)R=0\,. \tag{A.11}$$

Equation (A.11) is just a modified form of the Bessel differential equation, which has a solution:

$$R(r)=c_nJ_n\left(rk\right)+d_nY_n\left(rk\right) \tag{A.12}$$

where $J_n(x)$ and $Y_n(x)$ are Bessel functions of the first and second kinds, respectively.

The general solution is therefore:

$$w(r,\theta)=\sum_{n=-\infty}^{\infty}\left(c_nJ_n\left(rk\right)+d_nY_n\left(rk\right)\right)\left(a_ne^{\jmath n\theta}+b_ne^{-\jmath n\theta}\right),\quad n\in\mathbb{N} \tag{A.13}$$

or

$$w(r,\theta)=\sum_{n=0}^{\infty}\left(c_nJ_n\left(rk\right)+d_nY_n\left(rk\right)\right)\left(a_ne^{\jmath n\theta}\right),\quad n\in\mathbb{N}\,. \tag{A.14}$$

Appendix B

HANKEL FUNCTIONS

Two types of functions are known as Hankel functions and were introduced by H. Hankel in 1869. These functions are more common as Bessel functions of the third kind, or Cylinder functions. They are a linear combination of Bessel functions of the first and second kinds [48].

$$H_\nu^{(1)} = J_\nu + \jmath Y_\nu \tag{B.1}$$

$$H_\nu^{(2)} = J_\nu - \jmath Y_\nu \tag{B.2}$$

where ν is here a complex parameter.

J_ν is the Bessel functions of the first kind defined as

$$J_\nu(z) = \sum_0^\infty \frac{(-1)^m}{m!\Gamma(m+\nu+1)} \left(\frac{z}{2}\right)^{2m+\nu} \tag{B.3}$$

where $\Gamma(\cdot)$ is the Gamma function. Y_ν is the Bessel function of the second kind also called Weber functions, as they was introduced by H. M. Weber (1873), and also Neumann functions after Carl Neumann and there are define as

$$Y_\nu(z) = \frac{J_\nu(z)\cos(\nu z) J_{-\nu}(z)}{\sin(\nu z)} \tag{B.4}$$

In particular, when $\nu \notin \mathbb{Z}$, we have the expressions

$$H_\nu^{(1)}(z) = \frac{J_{-\nu}(z) - e^{-\nu\pi\jmath} J_\nu + (z)}{\jmath \sin \nu\pi} \tag{B.5}$$

$$H_\nu^{(2)}(z) = \frac{J_{-\nu}(z) - e^{\nu\pi\jmath} J_\nu + (z)}{-\jmath \sin \nu\pi\jmath} \tag{B.6}$$

whereas for integer values n of ν analogous formulas hold if we replace the right hand sides with their limits as $n \to \nu$. This implies the important relations

$$H_{-\nu}^{(1)} = e^{\nu\pi\jmath} H_{\nu}^{(1)} \tag{B.7}$$

$$H_{-\nu}^{(2)} = e^{-\nu\pi\jmath} H_{\nu}^{(2)} \tag{B.8}$$

When $\nu = p$ is real, the Bessel functions of the first kind take real values on the real axis. So it is obvious that, for $\nu = p$ real, $H_p^{(1)}$ and $H_p^{(2)}$ take complex conjugate values on the real axis. Moreover,

$$\jmath^{p+1} H_p^{(1)}(\jmath x) \qquad \text{and} \qquad \jmath^{-p-1} H_p^{(2)}(-\jmath x) \tag{B.9}$$

are real if x is real and positive. Hankel functions have simple asymptotic formulas for large $|z|$ when $\nu = p$ is real:

$$H_p^{(1)}(z) \sim \sqrt{\frac{2}{\pi z}} \exp\left(\jmath\left(z - p\frac{\pi}{2} - \frac{\pi}{4}\right)\right) \tag{B.10}$$

$$H_p^{(2)}(z) \sim \sqrt{\frac{2}{\pi z}} \exp\left(-\jmath\left(z - p\frac{\pi}{2} - \frac{\pi}{4}\right)\right) \tag{B.11}$$

The Hankel functions of half-integral $p = n + \frac{1}{2}, n \in \mathbb{Z}$,can be expressed in terms of elementary functions, in particular:

$$H_p^{(1)}(z) \sim \sqrt{\frac{2}{\pi z}} \frac{e^{ijz}}{\jmath} \tag{B.12}$$

$$H_p^{(2)}(z) \sim -\sqrt{\frac{2}{\pi z}} \frac{e^{-\jmath z}}{\jmath} \tag{B.13}$$

B.0.1 Recurrence relations

$$2H_{\nu}^{'}(z) = H_{\nu-1}(z) - H_{\nu+1}(z) \tag{B.14}$$

$$H_{\nu}^{'}(z) = H_{\nu-1}(z) - (\nu/z) H_{\nu}(z) \tag{B.15}$$

$$H_{\nu}^{'}(z) = -H_{\nu+1}(z) + (\nu/z) H_{\nu}(z) \tag{B.16}$$

$$H_0^{(1)'}(z) = -H_1^{(1)}(z) \qquad \text{and} \qquad H_0^{(2)'}(z) = -H_1^{(2)}(z) \tag{B.17}$$

Appendix C

Isoparametric shape functions

The details of (4.26) here has been reported.

$$
\begin{aligned}
2\pi\Phi_{i,n} &= \int_{\theta_N^i}^{\theta_0^i} \frac{\theta' - \theta_N^i}{\theta_0^i - \theta_N^i} e^{\jmath n\theta'} d\theta' + \int_{\theta_0^i}^{\theta_P^i} \left(1 - \frac{\theta' - \theta_0^i}{\theta_P^i - \theta_0^i}\right) e^{\jmath n\theta'} d\theta' \\
&= \frac{e^{-\jmath n\theta_N^i}}{\theta_0^i - \theta_N^i} \int_0^{\theta_0^i - \theta_N^i} \alpha e^{-\jmath n\alpha} d\alpha + e^{-\jmath n\theta_0^i} \int_0^{\theta_P^i - \theta_0^i} \left(1 - \frac{\alpha}{\theta_P^i - \theta_0^i}\right) e^{-\jmath n\alpha} d\alpha \\
&= \frac{e^{-\jmath n\theta_N^i}}{\theta_0^i - \theta_N^i} \left[-\frac{1}{\jmath^2 n^2} e^{-\jmath n\alpha}(\jmath n\alpha + 1)\right]_0^{\theta_0^i - \theta_N^i} \\
&\quad + e^{-\jmath n\theta_0^i} \left[-\frac{1}{\jmath^2 n^2} \frac{e^{-\jmath n\alpha}}{\theta_0^i - \theta_P^i} (\jmath n\alpha - \jmath n(\theta_P^i - \theta_0^i) + 1)\right]_0^{\theta_P^i - \theta_0^i} \\
&= \frac{e^{-\jmath n\theta_N^i}}{n^2(\theta_0^i - \theta_N^i)} \left[e^{-\jmath n(\theta_0^i - \theta_N^i)}(\jmath n(\theta_0^i - \theta_N^i) + 1) - 1\right] \\
&\quad + \frac{e^{-\jmath n\theta_0^i}}{n^2(\theta_0^i - \theta_P^i)} \left[e^{-\jmath n(\theta_P^i - \theta_0^i)} + (\jmath n(\theta_P^i - \theta_0^i) - 1)\right] \\
&= \frac{1}{n^2(\theta_0^i - \theta_N^i)} \left[e^{-\jmath n\theta_0^i}(\jmath n(\theta_0^i - \theta_N^i) + 1) - e^{-\jmath n\theta_N^i}\right] \\
&\quad + \frac{1}{n^2(\theta_0^i - \theta_P^i)} \left[e^{-\jmath n\theta_P^i} + e^{-\jmath n\theta_N^i}(\jmath n(\theta_P^i - \theta_0^i) - 1)\right] \\
&= \frac{1}{n^2(\theta_0^i - \theta_N^i)} \left[e^{-\jmath n\theta_0^i} \jmath n(\theta_0^i - \theta_N^i) + e^{-\jmath n\theta_0^i} - e^{-\jmath n\theta_N^i}\right] \\
&\quad + \frac{1}{n^2(\theta_0^i - \theta_P^i)} \left[e^{-\jmath n\theta_P^i} + e^{-\jmath n\theta_0^i} \jmath n(\theta_P^i - \theta_0^i) - e^{-\jmath n\theta_0^i}\right] \\
&= \frac{1}{n^2} \left[\jmath n e^{-\jmath n\theta_0^i} + \frac{e^{-\jmath n\theta_0^i} - e^{-\jmath n\theta_N^i}}{\theta_0^i - \theta_N^i} + \frac{e^{-\jmath n\theta_P^i} - e^{-\jmath n\theta_0^i}}{\theta_P^i - \theta_0^i} - \jmath n e^{-\jmath n\theta_0^i}\right] \\
&= \frac{1}{n^2} \left[\frac{e^{-\jmath n\theta_0^i} - e^{-\jmath n\theta_N^i}}{\theta_0^i - \theta_N^i} + \frac{e^{-\jmath n\theta_P^i} - e^{-\jmath n\theta_0^i}}{\theta_P^i - \theta_0^i}\right]
\end{aligned}
\tag{C.1}
$$

Bibliography

[1] S. Rao, D. Wilton, and A. Glisson. Electromagnetic scattering by surfaces of arbitrary shape. *IEEE Transactions on Antennas and Propagation*, 30(3):409–418, May 1982.

[2] A. Glisson. An integral equation for electromagnetic scattering from homogeneous dielectric bodies. *IEEE Transactions on Antennas and Propagation*, 32(2):173–175, February 1984.

[3] H. Tosun. Novel differential formulation of electromagnetic scattering by dielectric cylinders of arbitrary cross-section. *IEE Proceedings - Microwaves, Antennas and Propagation*, 141(3):189–195, June 1994.

[4] Y. W. Liu, K. K. Mei, and K. N. Yung. Differential formulation of on-surface measured equation of invariance for 2-d conducting scatterings. *IEEE Microwave and Guided Wave Letters*, 8(2):99–101, Feb 1998.

[5] Bjorn Engquist and Andrew Majda. Absorbing boundary conditions for the numerical simulation of waves. *Mathematics of Computation*, 31(139):629–651, 1977.

[6] Jean-Pierre Berenger. A perfectly matched layer for the absorption of electromagnetic waves. *Journal of Computational Physics*, 114(2):185 – 200, 1994.

[7] Alain. Bamberger, Patrick. Joly, and Jean E. Roberts. Second-order absorbing boundary conditions for the wave equation: A solution for the corner problem. *SIAM Journal on Numerical Analysis*, 27(2):323–352, 1990.

[8] Z. Che, L. Xu, and N. Wang. Implementation of a second-order abc in tdfem for 2d electromagnetic problems. In *2016 11th International Symposium on Antennas, Propagation and EM Theory (ISAPE)*, pages 534–538, Oct 2016.

[9] Z. S. Sacks, D. M. Kingsland, R. Lee, and Jin-Fa Lee. A perfectly matched anisotropic absorber for use as an absorbing boundary condition. *IEEE Transactions on Antennas and Propagation*, 43(12):1460–1463, Dec 1995.

[10] L. Aiyong, N. Zaiping, and Z. Yanwen. Numerical mode matching method with perfectly matching layer. In *2005 IEEE Antennas and Propagation Society International Symposium*, volume 4B, pages 372–375 vol. 4B, July 2005.

[11] F. L. Teixeira and W. C. Chew. Systematic derivation of anisotropic pml absorbing media in cylindrical and spherical coordinates. *IEEE Microwave and Guided Wave Letters*, 7(11):371–373, Nov 1997.

[12] Ying Xiao and Yilong Lu. Combination of pml and abc for scattering problem. *IEEE Transactions on Magnetics*, 37(5):3510–3513, Sep. 2001.

[13] R. Mittra and U. Pekel. A new look at the perfectly matched layer (pml) concept for the reflectionless absorption of electromagnetic waves. *IEEE Microwave and Guided Wave Letters*, 5(3):84–86, March 1995.

[14] C. M. Rappaport. Perfectly matched absorbing boundary conditions based on anisotropic lossy mapping of space. *IEEE Microwave and Guided Wave Letters*, 5(3):90–92, March 1995.

[15] Yun Li and Z. J. Cendes. High-accuracy absorbing boundary condition. *IEEE Transactions on Magnetics*, 31(3):1524–1529, May 1995.

[16] Jo-Yu Wu, D. M. Kingsland, Jin-Fa Lee, and R. Lee. A comparison of anisotropic pml to berenger's pml and its application to the finite-element method for em scattering. *IEEE Transactions on Antennas and Propagation*, 45(1):40–50, Jan 1997.

[17] Joseph B. Keller and Dan Givoli. Exact non-reflecting boundary conditions. *Journal of Computational Physics*, 82(1):172 – 192, 1989.

[18] Marcus J. Grote. Non-reflecting boundary conditions for electromagnetic scattering. *International Journal of Numerical Modelling: Electronic Networks, Devices and Fields*, 13(5):397–416, 2000.

[19] Yuexia Huang and Ya Lu. Scattering from periodic arrays of cylinders by dirichlet-to-neumann maps. *Lightwave Technology, Journal of*, 24:3448 – 3453, 10 2006.

[20] L. Yuan and Y. Y. Lu. An efficient bidirectional propagation method based on dirichlet-to-neumann maps. *IEEE Photonics Technology Letters*, 18(18):1967–1969, Sep. 2006.

[21] Yumao Wu and Ya Lu. Dirichlet-to-neumann map method for analyzing interpenetrating cylinder arrays in a triangular lattice. *JOSA B*, 25, 09 2008.

[22] Graeme Milton, Maxence Cassier, Ornella Mattei, Mordehai Milgrom, and Aaron Welters. *Extending the Theory of Composites to Other Areas of Science*. Milton-Patton Publishers, Salt Lake City, UT, 08 2016.

[23] I. A. Baratta and E. J. Silva. Multi-domain transmission conditions for domain decomposition methods applied to scattering problems. *IEEE Transactions on Magnetics*, 54(3):1–4, March 2018.

[24] M. J. Grote and C. Kirsch. Dirichlet-to-Neumann boundary conditions for multiple scattering problems. *Journal of Computational Physics*, 201:630–650, December 2004.

[25] Dan Givoli. *Numerical methods for problems in infinite domains*. Elsevier Science publishers, Amsterdam, Amsterdam, 1992.

[26] R. Mittra and O. Ramahi. Absorbing boundary conditions for the direct solution of partial differential equations arising in electromagnetic scattering problems. *Progress In Electromagnetics Research*, 02:133–173, 1990.

[27] A. F. Peterson. Accuracy of 3-d radiation boundary conditions for use with the vector helmholtz equation. *IEEE Transactions on Antennas and Propagation*, 40(3):351–355, March 1992.

[28] A. K. Belhora and L. Pichon. Efficient absorbing boundary conditions for the finite element solution of 3d scattering problems. *IEEE Transactions on Magnetics*, 31(3):1534–1537, May 1995.

[29] J. Peng and C. A. Balanis. Transparent absorbing boundary (tab) for the truncation of the computational domain. *IEEE Microwave and Guided Wave Letters*, 7(10):347–349, Oct 1997.

[30] A. T. de Hoop, P. M. van den Berg, and R. F. Remis. Absorbing boundary conditions and perfectly matched layers - an analytic time-domain performance analysis. *IEEE Transactions on Magnetics*, 38(2):657–660, March 2002.

[31] W. Li, Q. Zhang, Y. Chai, T. Li, and Z. Gong. An edge-based smoothed finite element method for two-dimensional underwater acoustic scattering problems. In *OCEANS 2016 - Shanghai*, pages 1–6, April 2016.

[32] Isaac Harari and Thomas J. R. Hughes. Studies of domain-based formulations for computing exterior problems of acoustics. *International Journal for Numerical Methods in Engineering*, 37(17):2935–2950, 1994.

[33] R. Stoffer, A. Sopaheluwakan, M. Hammer, and E. van Groesen. A combination of dirichlet to neumann operators and perfectly matched layers as boundary conditions for optical finite element simulations. In *2008 12th International Conference on Mathematical Methods in Electromagnetic Theory*, pages 124–126, June 2008.

[34] Dan Givoli, Igor Patlashenko, and Joseph B. Keller. Discrete dirichlet-to-neumann maps for unbounded domains. *Computer Methods in Applied Mechanics and Engineering*, 164(1):173 – 185, 1998. Exterior Problems of Wave Propagation.

[35] T. Demeester and D. De Zutter. Construction of the dirichlet to neumann boundary operator for triangles and applications in the analysis of polygonal conductors. *IEEE Transactions on Microwave Theory and Techniques*, 58(1):116–127, Jan 2010.

[36] Jianhua Yuan, Ya Yan Lu, and Xavier Antoine. Modeling photonic crystals by boundary integral equations and dirichlet-to-neumann maps. *Journal of Computational Physics*, 227(9):4617 – 4629, 2008.

[37] Shichang She and Y. Y. Lu. Multiple scattering by circular cylinders on a square lattice. In *17th Microopics Conference (MOC)*, pages 1–2, Oct 2011.

[38] Jianhua Yuan and Ya Yan Lu. Photonic bandgap calculations with dirichlet-to-neumann maps. *J. Opt. Soc. Am. A*, 23(12):3217–3222, Dec 2006.

[39] D. Klindworth and K. Schmidt. Dirichlet-to-neumann transparent boundary conditions for photonic crystal waveguides. *IEEE Transactions on Magnetics*, 50(2):217–220, Feb 2014.

[40] Z. Hu. Analyzing photonic crystal heterostructure mode-gap cavities by dirichlet-to-neumann maps. In *2015 IEEE International Conference on Computational Electromagnetics*, pages 218–220, Feb 2015.

[41] J. Yoon, J. Kim, and J. Jo. Singularity of scattering and dirichlet-to-neumann operator symbols in elliptic wave propagation models. *IMA Journal of Applied Mathematics*, 80(3):651–675, June 2015.

[42] U. R. Patel, S. V. Hum, and P. Triverio. Fast parameter extraction for transmission lines with arbitrarily-shaped conductors and dielectrics using the contour integral method. In *2016 IEEE 25th Conference on Electrical Performance Of Electronic Packaging And Systems (EPEPS)*, pages 193–196, Oct 2016.

[43] T. Demeester and D. de Zutter. Applications of the dirichlet-to-neumann boundary operator in transmission line modeling. In *2009 20th International Zurich Symposium on Electromagnetic Compatibility*, pages 25–28, Jan 2009.

[44] A. Y. Anikin, S. Y. Dobrokhotov, V. E. Nazaikinskii, and M. Rouleux. Asymptotics of green function for the linear waves equations in a domain with a non-uniform bottom. In *2017 Days on Diffraction (DD)*, pages 18–23, June 2017.

[45] G. A. Athanassoulis and C. E. Papoutsellis. Nonlinear irrotational water waves over variable bathymetry. the hamiltonian approach with a new efficient representation of the dirichlet to neumann operator. In *2015 Days on Diffraction (DD)*, pages 1–7, May 2015.

[46] A.Efremov S. Ventre L. Udpa and A. Tamburrino. Application of dirichlet-to-neumann map boundary condition for low frequency electromagnetic problems. *submitted for publication*, 2020.

[47] J.M. Jin. *The Finite Element Method in Electromagnetics*. Wiley - IEEE. Wiley, 2015.

[48] Milton Abramowitz and Irene A. Stegun. *Handbook of Mathematical Functions with Formulas, Graphs, and Mathematical Tables*. Dover, New York, 1964.

[49] James Cooley and John Tukey. An algorithm for the machine calculation of complex fourier series. *Mathematics of Computation*, 19(90):297–301, 1965.

[50] H. Bussey and J. Richmond. Scattering by a lossy dielectric circular cylindrical multilayer numerical values. *IEEE Transactions on Antennas and Propagation*, 23(5):723–725, Sep. 1975.

[51] H. A. van der Vorst. Bi-cgstab: A fast and smoothly converging variant of bi-cg for the solution of nonsymmetric linear systems. *SIAM J. Sci. Stat. Comput.*, 13(2):631–644, March 1992.

[52] L. Gerard G. Sleijpen. Bicgstab for linear equations involving unsymmetric matrices with complex. *Electronic Transactions on Numerical Analysis Volume*, 01:11–323, September 1993.

[53] Yousef Saad. *Iterative methods for sparse linear systems*. SIAM, New York, 2003.

[54] Edmond Chow and Aftab Patel. Fine-grained parallel incomplete lu factorization. *SIAM Journal on Scientific Computing*, 37:C169–C193, 03 2015.

[55] www.comsol.com.

[56] D. Baudry, C. Arcambal, A. Louis, B. Mazari, and P. Eudeline. Applications of the near-field techniques in emc investigations. *IEEE Transactions on Electromagnetic Compatibility*, 49(3):485–493, Aug 2007.

[57] Domenico Capriglione, A.G. Chiariello, and Antonio Maffucci. Accurate models for evaluating the direct conducted and radiated emissions from integrated circuits. *Applied Sciences*, 8:477, 03 2018.

[58] A. Maffucci, A. Perrotta, G. Rubinacci, A. Tamburrino, and S. Ventre. Efficient numerical evaluation of the electromagnetic scattering from arbitrarily-shaped objects by using the dirichlet-to-neumann map. In *2017 International Conference on Electromagnetics in Advanced Applications (ICEAA)*, pages 1616–1619, Sep. 2017.

[59] A. Maffucci A.Perrotta S.Ventre and A. Tamburrino. Numerical solution of electromagnetic scattering problems based on the dirichlet-to-neumann map. *Proceedings of IEEE RTSI, Sep. 2018, Palermo, Italy*, pages 1–5, 09 2018.

[60] Antea M. Perrotta, Antonio Maffucci, Salvatore Ventre, and Antonello Tamburrino. Efficient near-field analysis of the electromagnetic scattering based on the dirichlet-to-neumann map. *Applied Sciences*, 9(19), 2019.

[61] Philip M. Morse and Herman Feshbach. Methods of theoretical physics. *American Journal of Physics*, 22(6):pp 656–657, 1953.